Project Acronym:

SOUNDPET(INTEGRATED/0918/0008)

MRI-guided Focused ultraSOUND system for cancer in PETs (dogs and cats).

Deliverable number: 6.4

Title: Evaluation of navigation algorithms for reducing the near-field heating and the treatment time.

Prepared by:

Theocharis Drakos (MEDSONIC)

Christakis Damianou (CUT)

Date: 25/06/2021

Ευρωπαϊκή Ένωση
Ευρωπαϊκά Διαρθρωτικά και Επενδυτικά Ταμεία

Κυπριακή Δημοκρατία

Διαρθρωτικά Ταμεία της Ευρωπαϊκής Ένωσης στην Κύπρο

Table of Contents

Executive Summary

In this deliverable, the near and far-field heating of six different navigation algorithms was evaluated. The amount of the induced near and far-field heating was estimated using thermocouples. Each of the six algorithms (Sequential, Euler's, Spiral, Square, Random, and Triangular) was evaluated by sonicating an agar-based phantom containing 2 % weight per volume (w/v) agar and 4 % w/v wood powder. The sonication was performed using a 1.1 MHz transducer in a 10 x 10 square grid with a 2 mm step, resulting in 99 sequential movements of the transducer from the initial to final grid point.

The distance between the transducer and the bottom surface of the phantom was set at 4 cm, resulting in a focal depth of 3 cm. Two thin thermocouples of identical type and thickness were inserted in the phantom; the one at 1 cm depth (2 cm from the focal plane) and the other one at 7 cm depth (4 cm from the focal plane) to measure the induced heating in the near and far-field regions, respectively. An acoustical power of 22 W was applied at each grid point for a sonication time of 5 s. Different delays between sequential sonications of 0 s, 10 s, 20 s, 30 s, 40 s, 50 s, and 60 s were used to examine the effect of increasing delay on the temperature increase in the near and far-field regions for each algorithm. The thermal dose and the delay that is required for safe treatment were estimated for each algorithm.

Introduction

The efficient ablation of malignant tissue during a High Intensity Focused Ultrasound (HIFU) procedure is highly dependent on the use of robotic devices for navigating the ultrasonic transducer so as to achieve utmost tissue ablation. Motion algorithms following predetermined rules are utilized for maximal coverage of tissue areas, with the majority of cases following a sequential [1], [2] or a spiral algorithm [3]. Successive sonications utilized by sequential movement do not allow cooling of proximal tissue cells, resulting in excess deposition of thermal energy and increased temperatures in the pre-focal region (near-field). Near-field heating is a major drawback for a HIFU procedure since it limits the amount of ultrasonic energy supplied to the focal region, thus affecting maximum tissue ablation and treatment time [4], impacting surrounding healthy tissues, and inducing unwanted effects such as skin burns [5].

In order to allow diffusion of thermal energy, cooling periods should be introduced between successive sonications for reducing the near-field heating. This was firstly introduced in 1993 [4] where a time delay of 20 s between sonications substantially decreased near-field heating. The authors concluded that increasing time delay and operating frequency or decreasing sonication time and transducer's F-number (radius of curvature/ diameter) greatly reduced near-field heating. However, later studies [7], [28] consistently showed that the aforementioned delay was probably not sufficient. The effect of near-field heating's dependency on F-number was later confirmed when two transducers having the same nominal frequency and diameter but varied focal length were used [6]. A variation of time delays between 30 or 90 s was needed for inducing the same amount of pre-focal heating among the two transducers, with a higher time delay required for the transducer having increased focal length (i.e., increased F-number). Near-field heating and the shape of the ablation area were investigated by McDannold et al. [7] during in vivo sonications using time delays of 11-60 s monitored by Magnetic Resonance Imaging (MRI). Time delays of up to 40 s induced increased pre-focal heating and necrosis area, with the optimal 60 s delay required for elimination of the near-field heating and formation of a uniform area of necrosis.

Following the introduction of monitoring during sonications, MRI thermometry was much later proposed and used for monitoring the temperature increase in the near-field region during *in vivo* volumetric ablations [5]. Substantial near-field heating and increased area of necrosis were observed, with the former being linearly related to the energy density, which can thus be a sign for possible induced necrosis. Although proton resonance frequency shift (PRFS) MRI thermometry has since been utilized during in vivo soft tissue sonications for the monitoring of near-field heating [8], its utilisation for monitoring near-field heating in fat tissue is unfeasible [9]. To compensate for this, T2-based temperature measurements were investigated and proven feasible for monitoring near-field heating in fat tissue, although being much slower than the respective PRFS method [9]. Although near-field heating can be monitored with MR thermometry, undetected necrosis can still be induced if the accumulation of thermal energy is not sufficiently accounted for by using appropriate cooling periods [10].

However, the introduction of cooling periods between sonications significantly increases the overall treatment time. The study by Ji et al. [11] proposed a new way of utilising cooling periods by exploiting both *in silico* and *ex vivo* experiments. They used a linear algorithm for sonications in a 4 x 4 grid, where cooling periods were only utilized between each grid line. Additionally, they divided the volume in four 2 x 2 grids and used square movement for the sonication of each subsection, with a cooling period introduced after each sub-sectional sonication. The nature of the square movement resulted in a decreased treatment time, with a 60 s time delay required for reduction of the near-field heating.

Studies have shown that the reduction of the near-field heating, and consequently the increase of the energy absorption in the focal region, can also be achieved by using pulsed waves [8], cooling of the transducer with cold water for approximately half an hour prior to sonication [12], or exterior tissue cooling through the means of a cooling mat [13]. The latter was utilized for abdominal ablation since higher powers are used so as to adjust for the increased perfusion of organs, thereby resulting in higher near-field heating [13]. The use of perfluorocarbon agents such as microbubbles and nanodroplets, has also been proven able in reducing heating in the pre-focal region and thereby increasing temperature deposition at the focal region [14]. Compared to microbubbles, nanodroplets resulted in decreased near-field heating and double energy deposition in the focal region, thereby concluding that they can possibly reduce treatment time by a factor of 3 [14].

Despite the fact that phased arrays are not dependent on the motion algorithm but rather on the electronic steering of the focal point for treating large volumes of tissue, the volumetric ablation utilized entails extended ultrasonic exposures resulting in greater induced near-field heating than their non-phased counterparts, thereby requiring longer delays between sonications [7], [15]. Further studies also confirmed that electronic steering of the phased array transducer significantly increases the accumulated thermal dose in the near-field region, compared to mechanical steering [16]. Volumetric ablation was introduced more than a decade ago and it involves electronically maneuvering the focus of the transducer for sonicating points located in concentric circles of increasing diameter [15]. The method was later improved by development of an algorithm that dynamically controls the ultrasonic duration on each concentric circle through MR thermometry feedback from already sonicated points, thereby resulting in decrease of the near-field heating [17]. The algorithm was further improved through development of a dynamic control system of activation or deactivation of the individual ultrasonic elements inducing further reduction of near-field heating [18].

In order to reduce near-field heating, a simulation study [19] and later an experimental evaluation [20] for a phased array transducer operating at a frequency of 500 kHz were performed for potential ablation of fibroids. Although the near-field heating of the transducer was reduced, its low operating frequency increased heating in the far-field (post-focal region). According to the author's proposal about its use for fibroid ablation, the transducer could potentially result in unnecessary heating in the spinal area [19].

The introduction of varied cooling times between sonications for reducing the near-field heating effect results in prolonged treatment times particularly for large ablation areas. The use of conventional sequential movement for treatment resulted in the utilization of other algorithms (spiral, square) [3], [11] that spatially distribute the successively sonicated cells in a way that allows diffusion of thermal energy so as to reduce the high accumulation of energy in the near-field region. The demand for development of new algorithms that result in lower treatment times stimulated the introduction of new algorithms by Yiallouras et al. [21]. The authors used simulation studies for evaluating the induced heating and thermal dose in the pre-focal region with each of the six proposed algorithms. Nevertheless, no temperature data was acquired for supporting the modelling. Varying time delays were introduced between sonications in order to eliminate near-field heating and reduce the treatment time. The authors concluded that half of the proposed algorithms significantly reduced near-field heating.

In this paper we present the experimental evaluation of the six algorithms previously proposed by Yiallouras et al. [21], by sonicating an agar-based phantom doped with wood powder [22]. The phantom was used as a soft tissue mimicking material since it presents with the same ultrasonic, thermal and MR properties as those of soft tissue [22]. The effect of increasing time delay between sonications on the induced temperature in the near and far-field regions of the transducer using each algorithm was examined. The recorded temperature increase was utilized in order to calculate the thermal dose, as defined by Sapareto and Dewey [23], accumulated both in the near and far-field regions. Although there have been a number of simulation studies [16], [21] examining the thermal dose induced by the respective candidate transducer in the near-field region, the existing literature does not include any experimental assessment of the induced dose in either the near-field or the far-field. Thereby, the proposed study is novel since it experimentally assesses the induced thermal dose in both the near and far-field regions so as to find the optimal time delay and algorithm.

Materials and Methods

Robotic system

The SOUNDPET robotic device Version 2 was used to navigate the spherically-focused transducer. Specifically, the motors offer linear movement of the transducer in the X, Y, and Z axes. Motion in the X and Y axes was necessary to perform the motion patterns of specific algorithms in a plane perpendicular to the focal beam while the Z-axis was used to adjust the distance between the focused transducer and the phantom (and therefore the focal depth). The robotic device is described in detail in Deliverable 3.1.

Mechanical design

The phantom was held and stabilized in a 3D printed structure (F270, Stratasys Ltd., Minnesota, USA) that was designed to attach to the acoustic opening of the water enclosure. The structure was made out of Acrylonitrile Butadiene Styrene (ABS) plastic and was designed to allow easy vertical insertion of thin (100 μm) thermocouples (5SC-TT-K-30-36, type K insulated beaded wire, 100 μm thick, Omega Engineering, Norwalk, Connecticut, USA) at various locations spaced by 5 mm in the phantom in a plane perpendicular to the ultrasound beam. Figure 1 shows the computer-aided design (CAD) drawing of the phantom holder designed to accommodate the phantom above the transducer so that proper ultrasonic coupling is achieved through water.

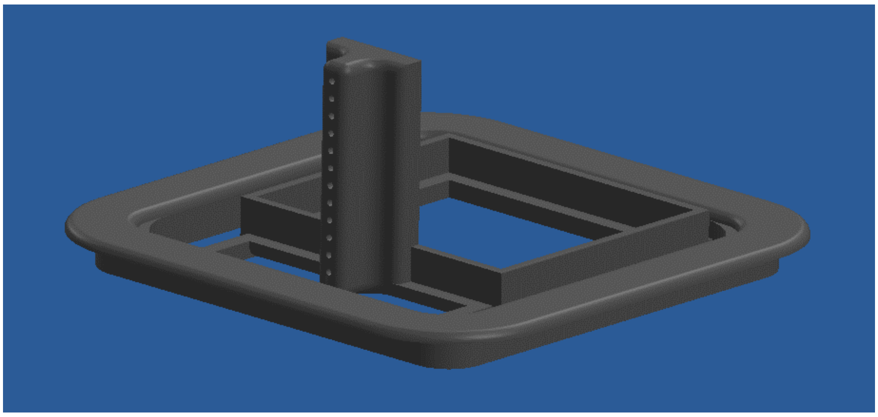

Figure 1: CAD drawing of the phantom holder.

Sample

The heating effects of the algorithms in the near and far-field were evaluated in an agar-based gel phantom. The tissue-mimicking material was composed of degassed/de-ionized water, 2 % w/v agar (Merck KGaA, EMD Millipore Corporation, Darmstadt, Germany), and 4 % w/v wood powder (Swedish pine). The phantom was developed in a 3D-printed Acrylonitrile Styrene Acrylate (ASA) cube mold with a volume of 512 cm^3. The procedure of phantom development is fully described in Deliverable 4.1.

The 3D printed holder as attached to the acoustic opening of the water container is shown in Figure 2. Figure 3 shows of a photo of the experimental set-up with the agar/wood powder phantom mounted on the holder.

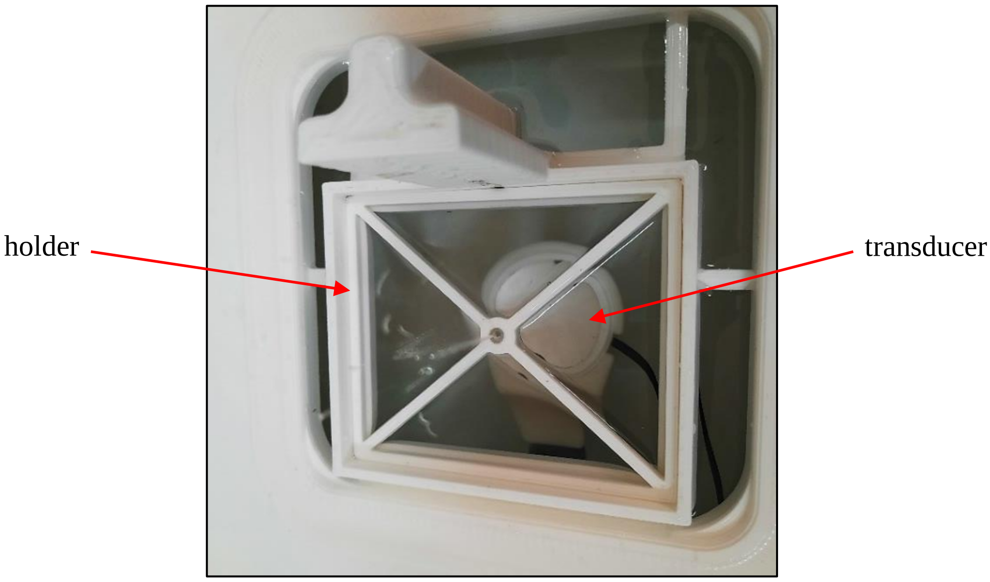

Figure 2: The phantom holder as attached to the acoustic opening of the water enclosure.

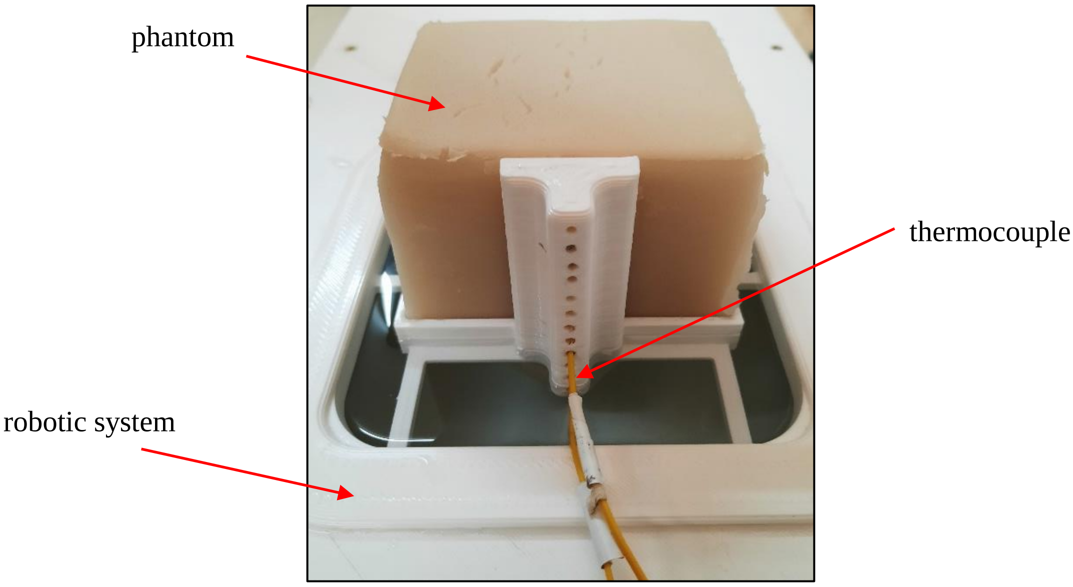

Figure 1: Photo of the experimental set-up.

Software and temperature reader

A custom-made software written in c# was used to send motion commands to the motor controllers via a friendly graphical user interface. The software allows the user to control parameters such as the grid size, voltage (for acoustic power selection), sonication time, delay, and motion algorithm. Figure 4 shows a screenshot of the controlling software prior to the execution of an algorithm. A temperature reader (HH806AU, Omega Engineering) continuously measured the temperature change in the phantom during each algorithm.

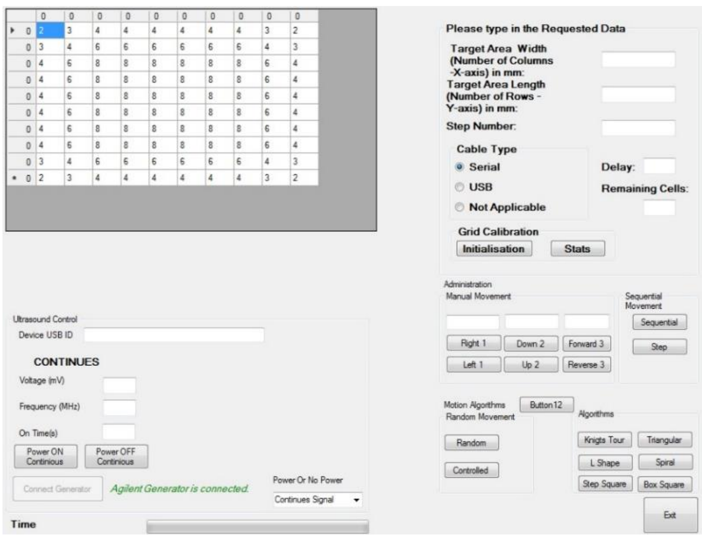

Figure 4: Software screenshot.

HIFU system

The HIFU system consisted of a signal generator (HP 33120A, Agilent technologies, Englewood, CO, USA), an RF amplifier (75A250M4, Acoustic Research, School House Road Souderton, PA, USA), and a single element spherically focused transducer. The generated voltage was matched to the acoustic power of the transducer using an ultrasonic power meter (UPM-DT100N, Ohmic Instruments Co., St. Charles, Missouri, USA). The focused transducer had an operating frequency of 1.1 MHz, a radius of curvature of 70 mm, and a diameter of 50 mm (piezoelectric element from Meggitt, Kvistgaard, Denmark), and was manufactured by Medsonic Ltd. (Limassol, Cyprus). The signal generator, RF amplifier, and focused transducer are shown in Figure 5. Figure 6 shows a schematic diagram of the complete experimental set-up.

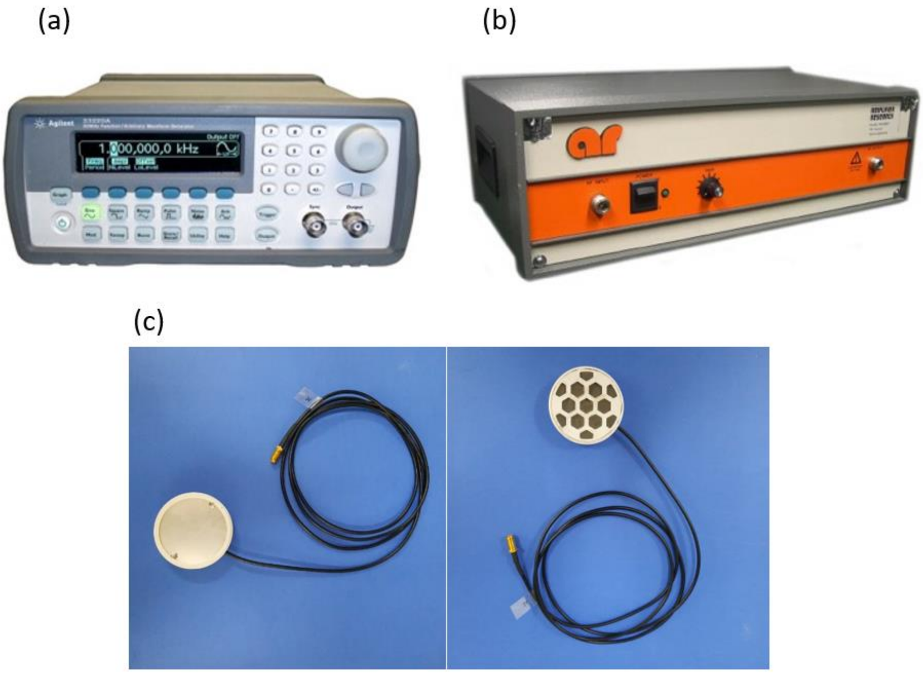

Figure 5: Photos of the a) signal generator, b) RF amplifier, and c) focused transducer (1.1 MHz).

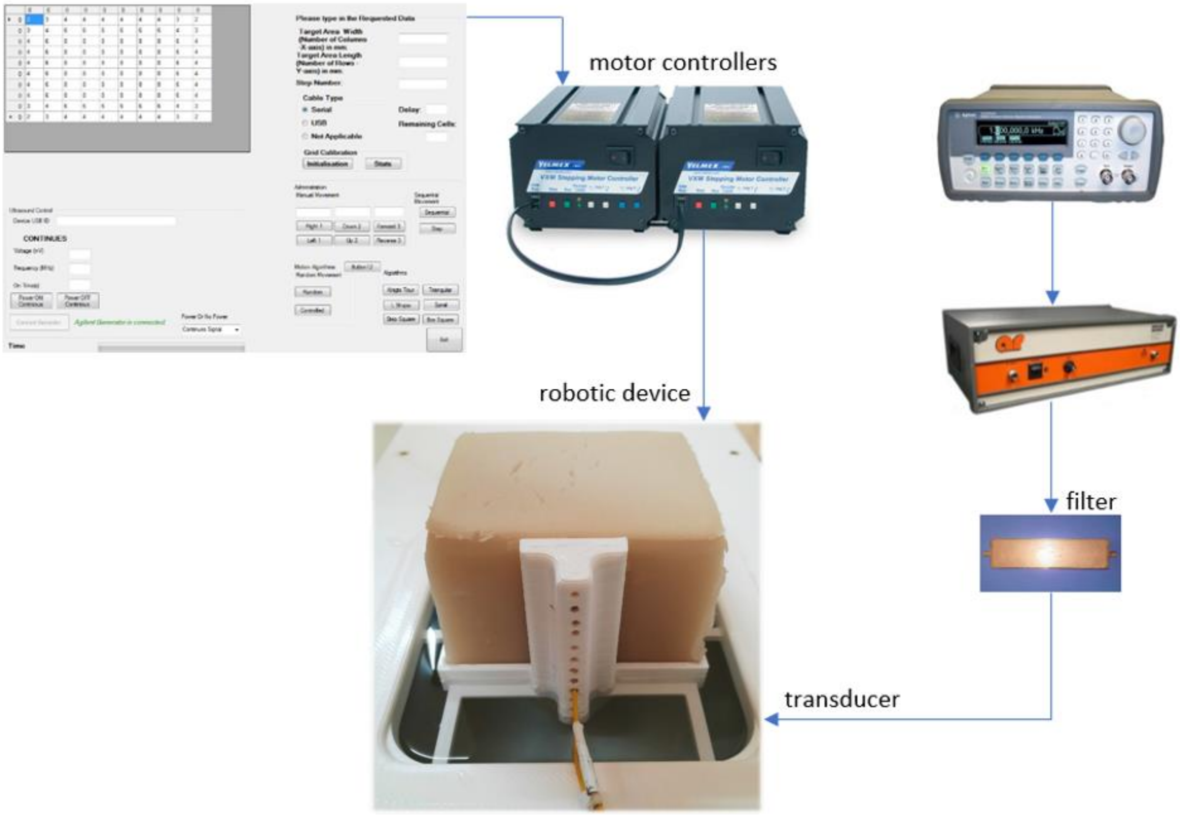

Figure 6: Schematic diagram of the complete experimental set-up.

Algorithms

Six different algorithms were applied with varying time delay to investigate the induced near and far-field heating of the transducer in the phantom. Every algorithm follows a different pathway depending on its rules. It may follow a path of adjacent or remote cells. The following algorithms were investigated for reducing the near and far-field heating: Sequential, Euler's, Spiral, Square, Random, and Triangular.

Sonication parameters and grid selection

For each algorithm, sonications were performed in a 10 x 10 grid with a 2 mm step, and an acoustical power of 22 W was applied at each grid point for a sonication time of 5 s. Therefore, the robotic device navigated the transducer at 100 grid points covering a total phantom area of 20 mm x 20 mm (a square of 10 mm around the center of the phantom). The distance between the transducer and the bottom surface of the phantom was adjusted at 4 cm. Initially, the thermocouples were inserted in the phantom at various depths and a delay of 30 s was used to define the near-field and far-field regions of the beam. Thermocouples were consecutively inserted at 1, 3, 4, 5, 6, and 7 cm depth. After the focal point was defined, a thermocouple was inserted in the phantom at 1 cm depth to measure the induced heating in the near-field region. A second identical thermocouple was placed at 7 cm depth to measure the induced heating in the far-field. Different delays of 0 s, 10 s, 20 s, 30 s, 40 s, 50 s, and 60 s were used to examine the effect of increasing time delay on the temperature increase in the pre-focal region for each algorithm. Figure 7a illustrates a schematic diagram of the top view of the phantom and the sonicated grid area for each algorithm. Figure 7b illustrates the side view of the phantom, indicating the distances on the setup.

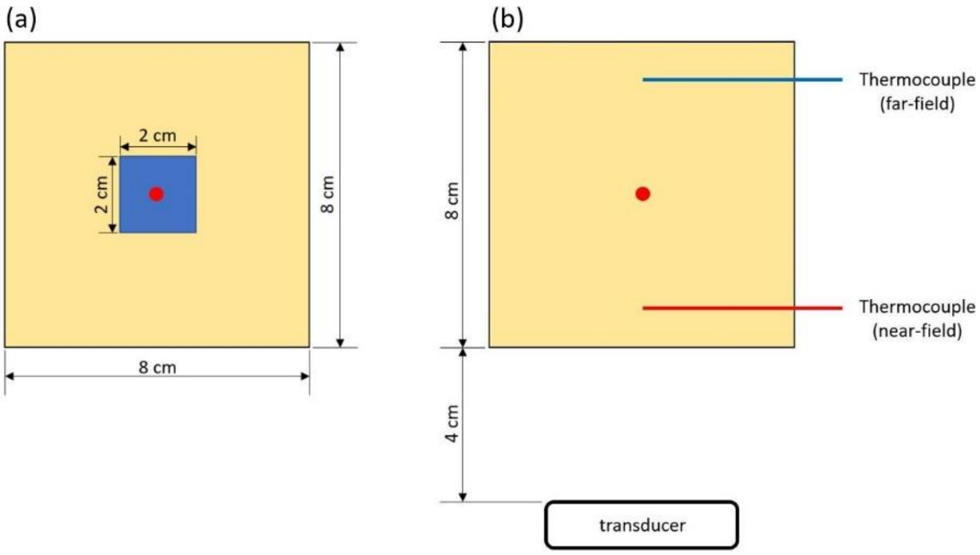

Figure 7: Schematic diagram of the a) top view of the phantom, and b) side view. The red dot indicates the location of the focal point.

Thermal dose estimation

The thermal dose of each algorithm, depth, and delay were estimated using a method proposed by Sapareto and Dewey [23]:

$$CEM43°\mathrm{C} = \sum_{t=0}^{t=final} R^{(43-T)} \Delta t \quad (1)$$

where *CEM43°C* is the cumulative number of equivalent minutes at 43 °C, *T* is the average temperature during time *Δt*, and *R* relates to the temperature dependence on the rate of cell death. R values of 0.25 and 0.5 were used for temperatures smaller and higher than 43 °C, respectively. The temperatures have been shifted so that the initial temperature was set at 37 °C to simulate the temperature of the human body.

Results

Sequential

In this algorithm, the transducer moves from the left to the right side of the grid in the x-axis, and then, one step down in the y-axis. Then, it starts moving from the right back to the left side and the process repeats itself. The sonicated grid is shown in Figure 8.

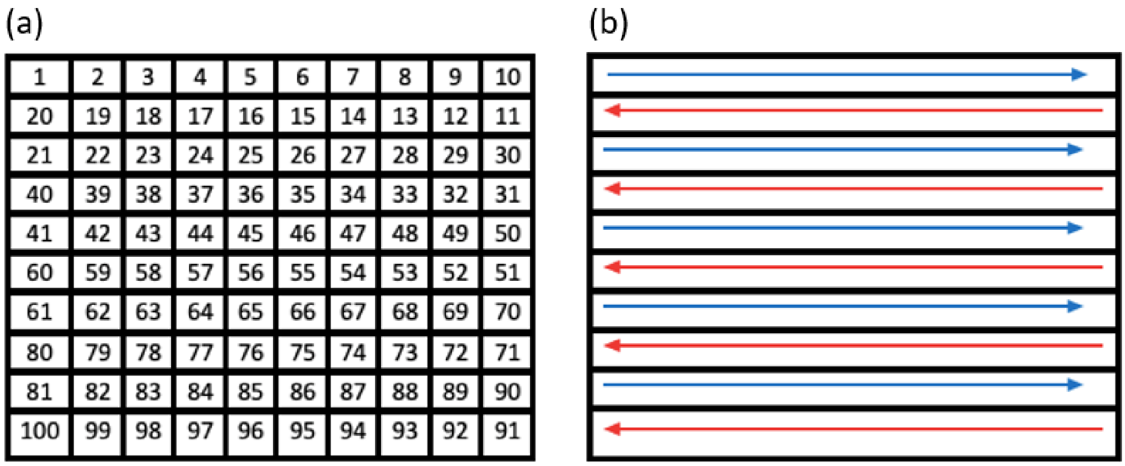

Figure 8: a) Transducer movement with sequential algorithm, and b) conceptual diagram.

The thermocouples were inserted in the phantom at various depths to define the near-field and far-field regions of the beam. Figure 9 shows graphs of the temperature versus time recorded at the various depths along the phantom.

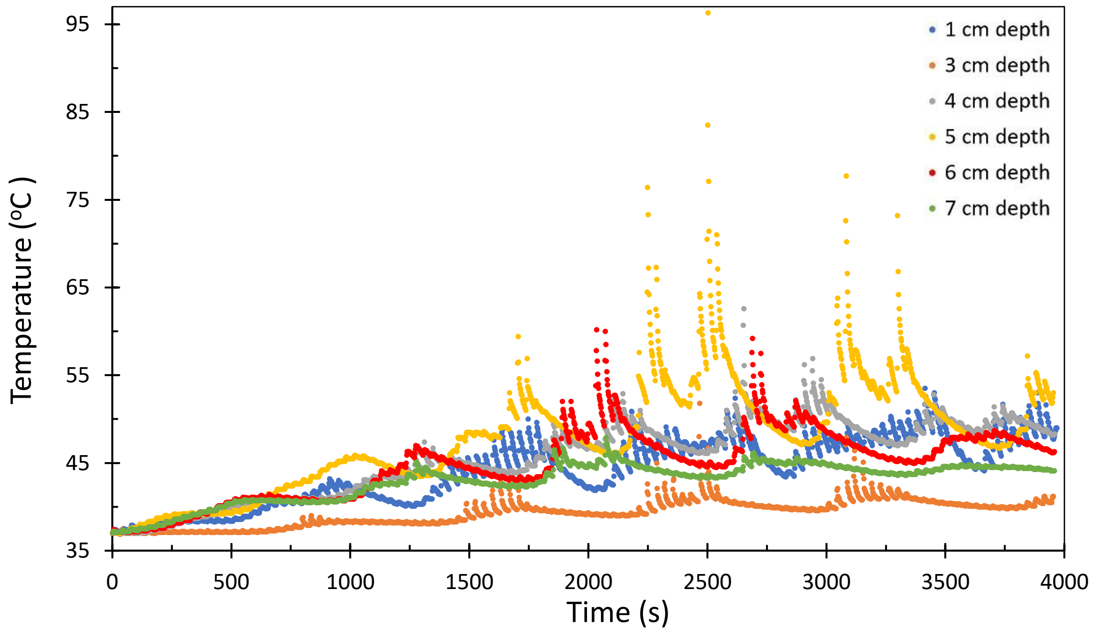

Figure 9: Temperature versus time recorded at various depths within the phantom for sonication in a 10 x 10 grid using acoustical power of 22 W, sonication time of 5 s, and delay of 30 s.

Table 1 summarizes both the peak and average temperature change, as well as the total thermal dose accumulated at each depth.

Table 1: Peak and average temperature change and thermal dose at different depths within the phantom, for sonication in a 10 x 10 grid using acoustical power of 22 W for sonication time of 5 s and 30 s delay.

Depth within phantom (cm)	Peak ΔT (ºC)	Average ΔT (ºC)	Total dose (CEM43ºC)
1	16.5	7.2	1607.4
3	14.8	2.31	23.3
4	25.6	8.57	39175.9
5	59.3	10.96	3.7E14
6	23.2	7.87	21016.5
7	10.9	5.89	124.4

It was observed that the focal point of the transducer was situated at 5 cm depth. The radial spatial distribution of induced temperature was also investigated. Initially, the thermocouple was located at the center of the phantom. Motion steps of 2 mm were then performed in both radial directions. Figure 10 shows the induced temperature versus distance for every 2 mm radial step from the focal point (0 mm) of the transducer.

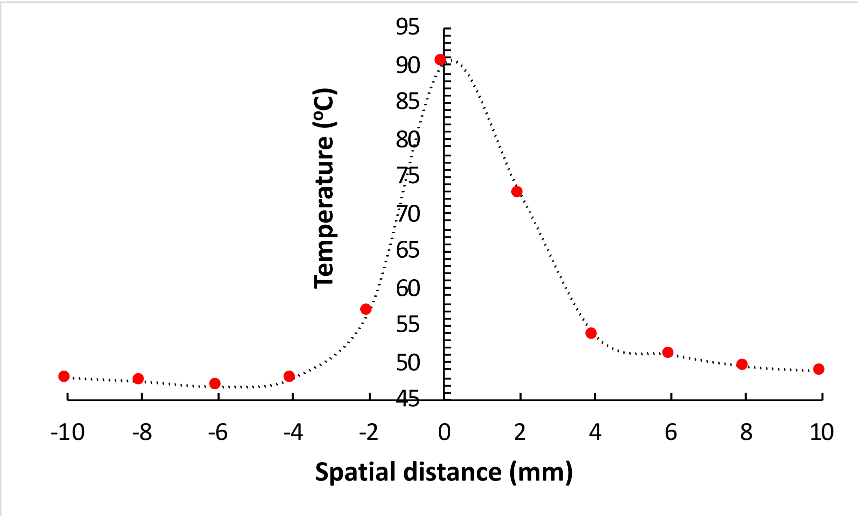

Figure 10: Temperature versus radial distance from the focal point of the transducer for sonication in a 10 x 10 grid using acoustical power of 22 W, sonication time of 5 s, and delay of 30 s.

Then the thermocouples were inserted at the near-field (1 cm depth) and far-field (7 cm depth) locations to record the temperature change using delays of 0 s, 10 s, 20 s, 30 s, 40 s, 50 s, and

60 s. The recorded temperature versus time for delays of 0 – 60 s (10 s step) is shown respectively in Figure 11 to Figure 17.

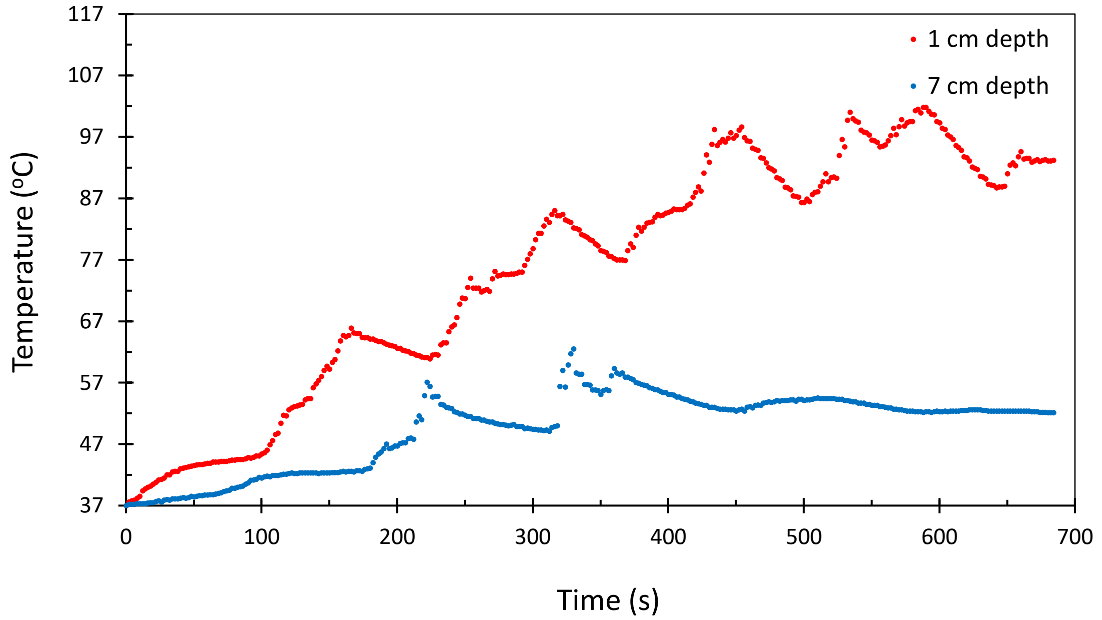

Figure 11: Temperature versus time at near-field (1 cm depth) and far-field (7 cm depth) for sonication in a 10 x 10 grid using acoustical power of 22 W, sonication time of 5 s, and delay of 0 s.

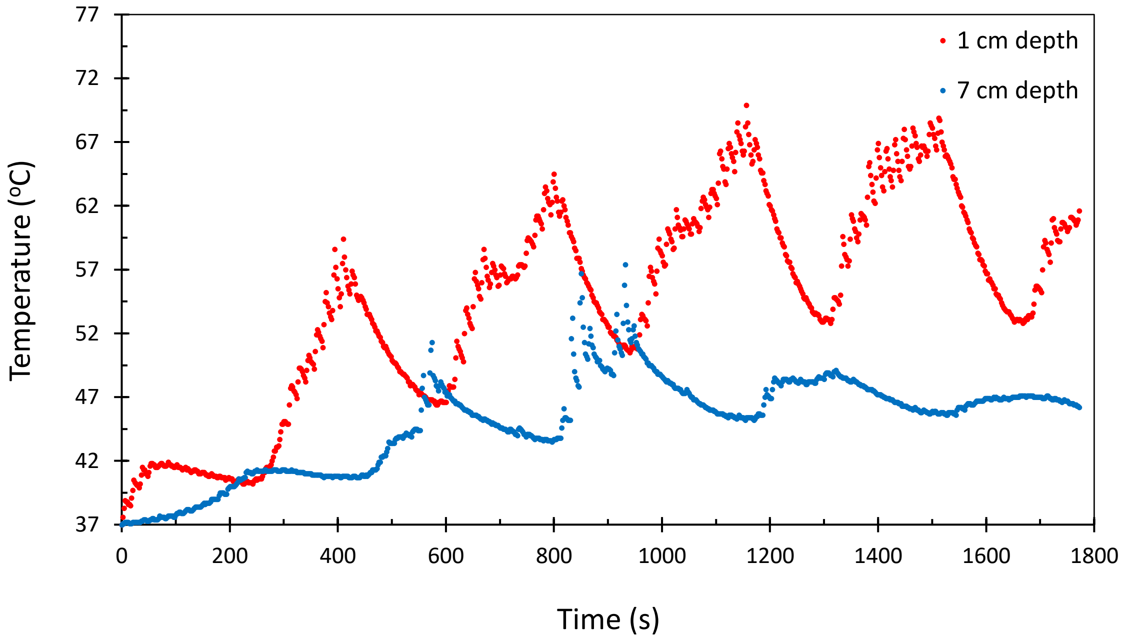

Figure 12: Temperature versus time at near-field (1 cm depth) and far-field (7 cm depth) for sonication in a 10 x 10 grid using acoustical power of 22 W, sonication time of 5 s, and delay of 10 s.

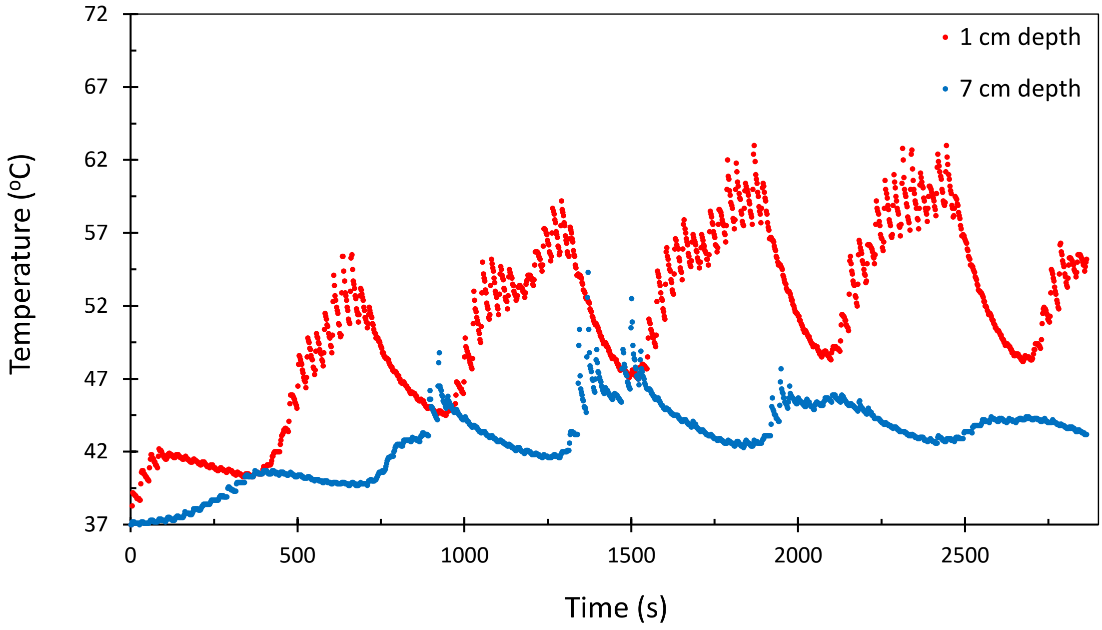

Figure 13: Temperature versus time at near-field (1 cm depth) and far-field (7 cm depth) for sonication in a 10 x 10 grid using acoustical power of 22 W, sonication time of 5 s, and delay of 20 s.

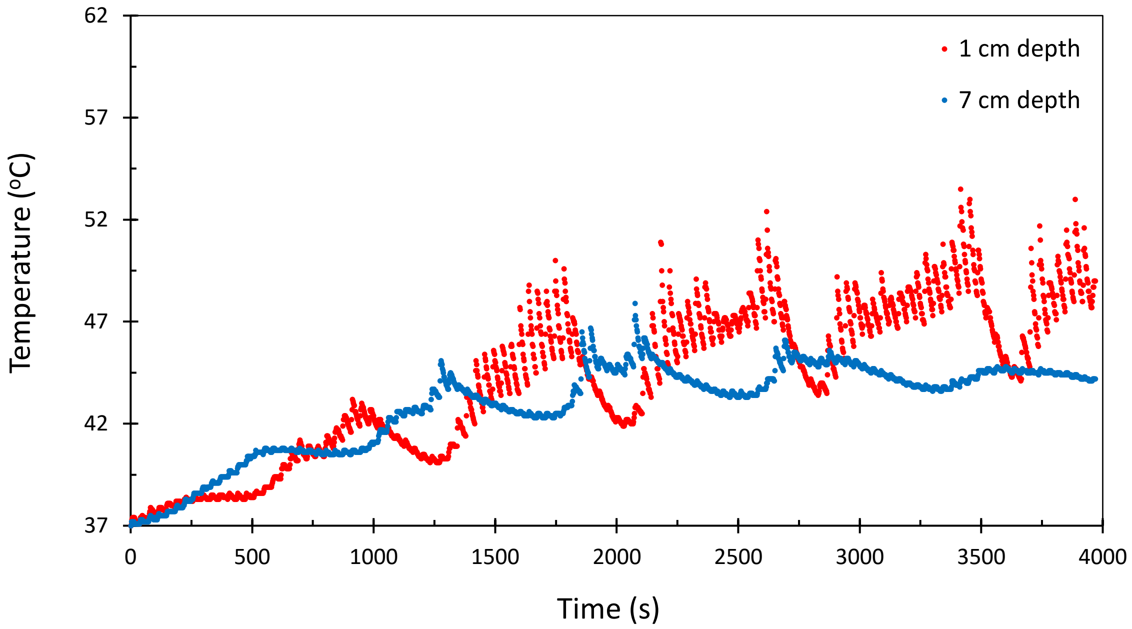

Figure 14: Temperature versus time at near-field (1 cm depth) and far-field (7 cm depth) for sonication in a 10 x 10 grid using acoustical power of 22 W, sonication time of 5 s, and delay of 30 s.

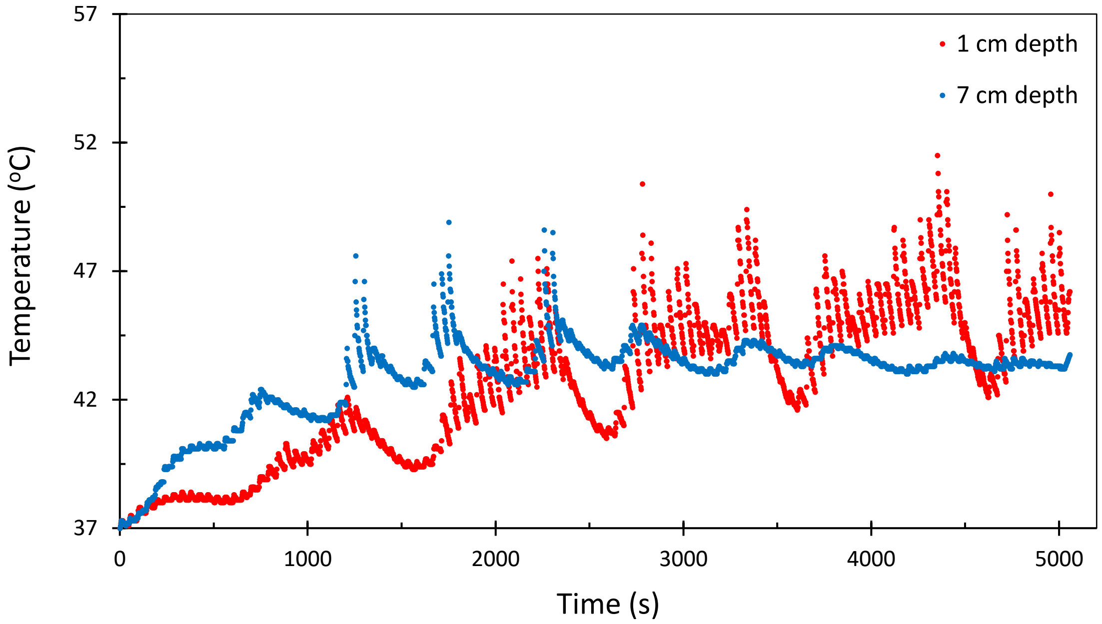

Figure 15: Temperature versus time at near-field (1 cm depth) and far-field (7 cm depth) for sonication in a 10 x 10 grid using acoustical power of 22 W, sonication time of 5 s, and delay of 40 s.

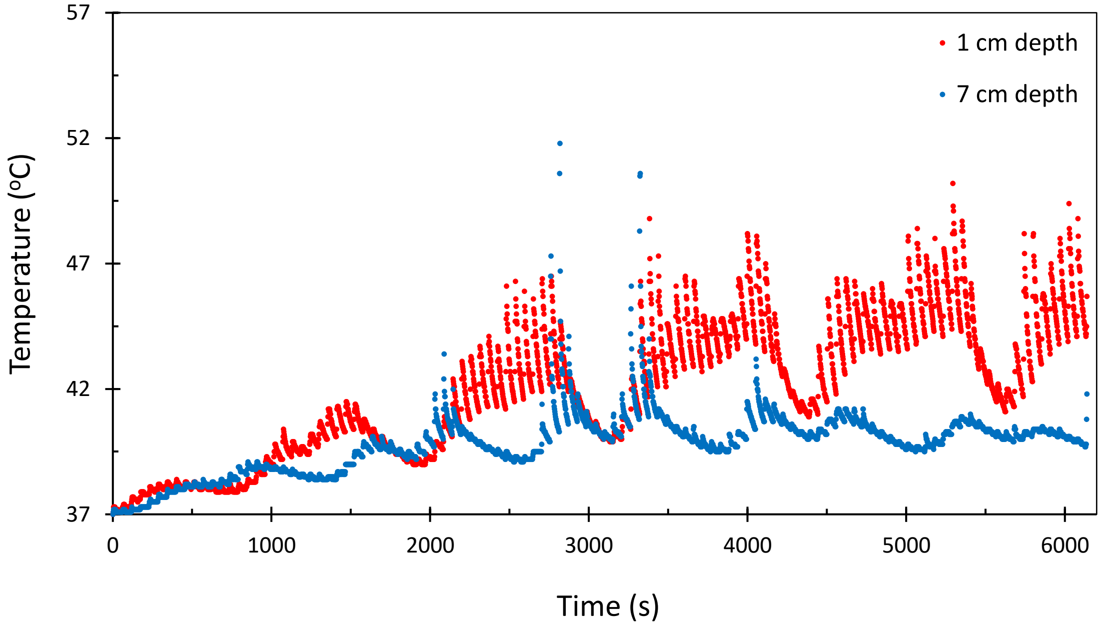

Figure 16: Temperature versus time at near-field (1 cm depth) and far-field (7 cm depth) for sonication in a 10 x 10 grid using acoustical power of 22 W, sonication time of 5 s, and delay of 50 s.

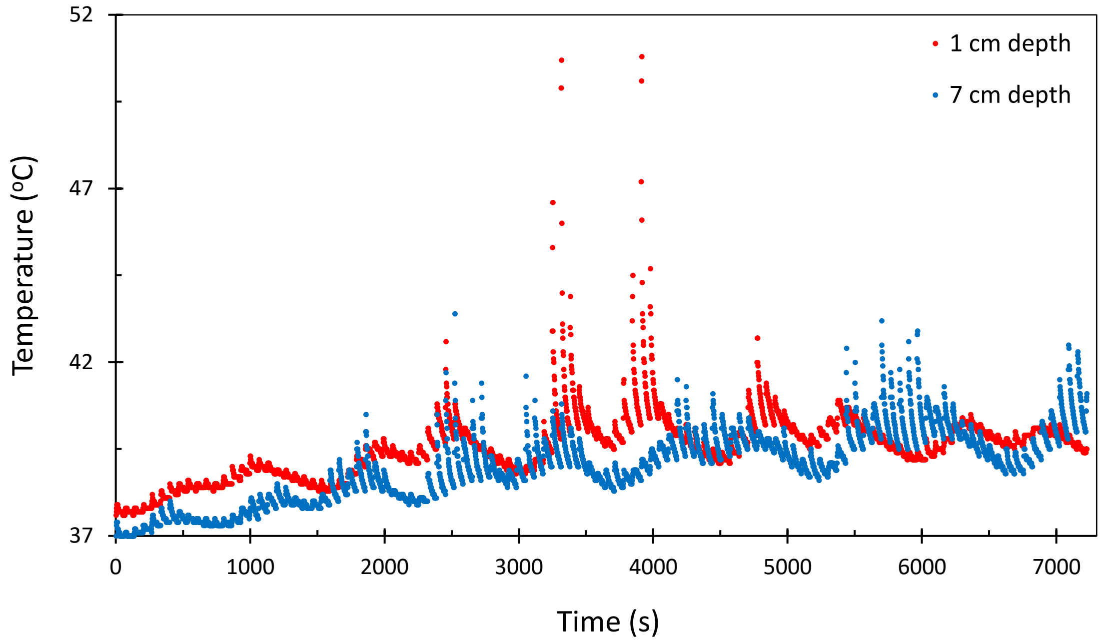

Figure 17: Temperature versus time at near-field (1 cm depth) and far-field (7 cm depth) for sonication in a 10 x 10 grid using acoustical power of 22 W, sonication time of 5 s, and time of 60 s.

Figure 18 shows the temperature versus time for the near-field (1 cm depth) using varying delays.

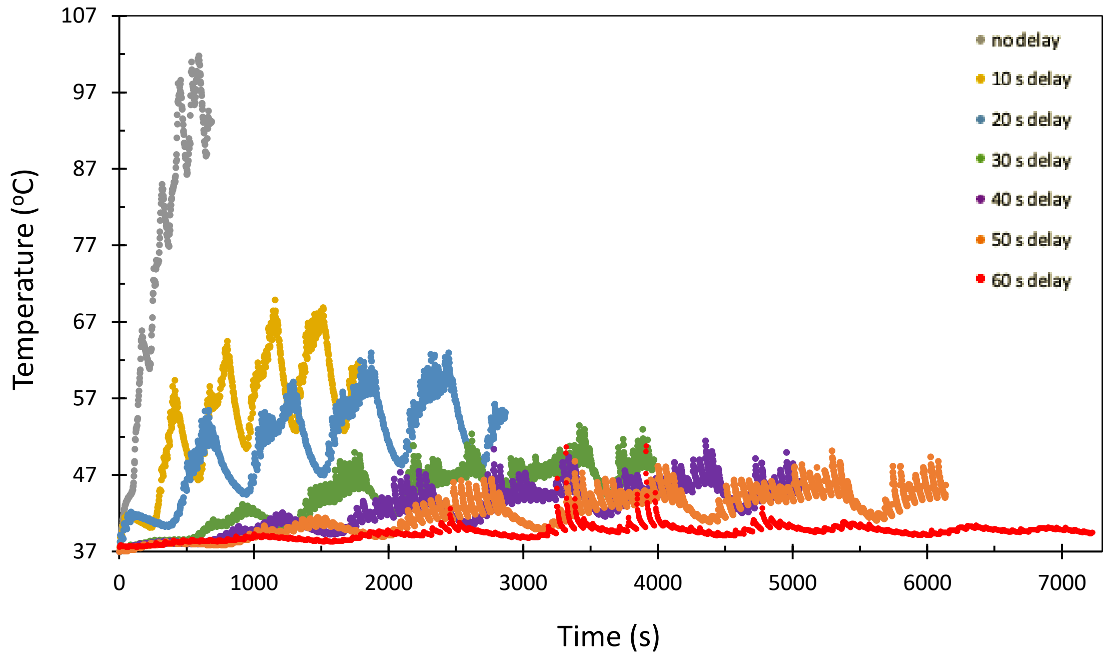

Figure 18: Temperature versus time at near-field (1 cm depth) for sonication in a 10 x 10 grid using acoustical power of 22 W, sonication time of 5 s, and varying delays (Sequential algorithm).

Table 2 summarizes both the peak and average temperature changes, as well as the thermal dose, for each delay at the near-field.

Table 2: Peak and average temperature change and total dose for each delay at near-field, for sonication in a 10 x 10 grid using acoustical power of 22 W for sonication time of 5 s.

Delay (s)	Peak ΔT (ºC)	Average ΔT (ºC)	Total dose (CEM43^{0}C)
0	64.8	38.5	1.70757E+17
10	32.9	17.49	56964725.96
20	26	13.77	977060.1
30	16.5	7.2	1607.4
40	14.5	5.58	365.7
50	13.2	5	236.3
60	13.2	1.94	17.6

Figure 19 shows the thermal dose versus delay in the near-field for the Sequential algorithm.

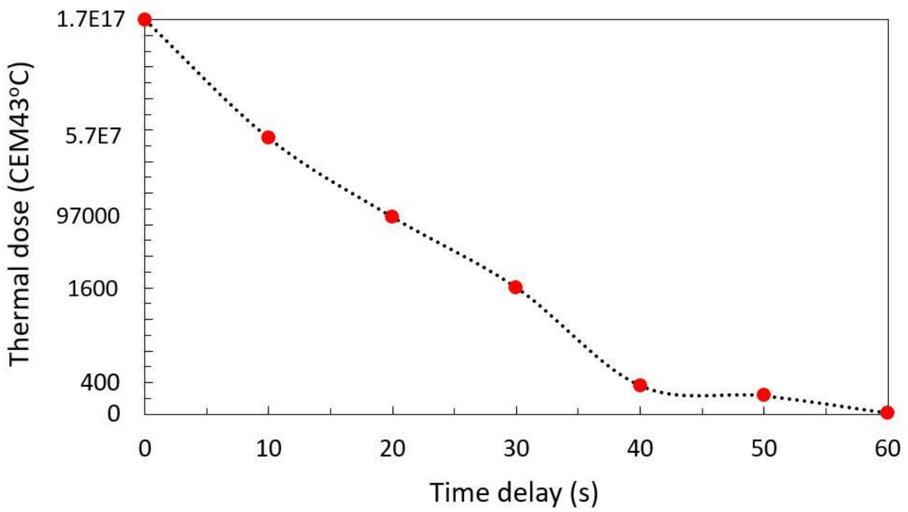

Figure 19: Thermal dose versus delay at near-field (1 cm depth) for sonication in a 10 x 10 grid using acoustical power of 22 W for sonication time of 5 s.

Figure 20 shows the temperature versus time for the far-field (7 cm depth) for various delays of 0-60 s.

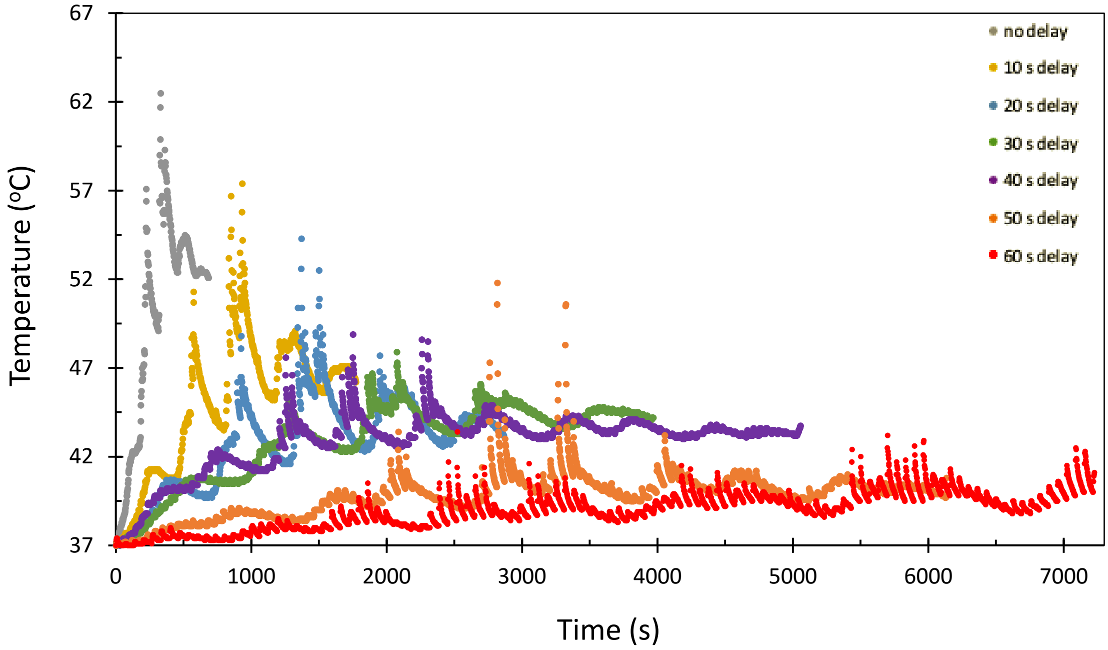

Figure 20: Temperature versus time at far-field (7 cm depth) for sonication in a 10 x 10 grid using acoustical power of 22 W, sonication time of 5 s, and varying delays (Sequential algorithm).

Table 3 summarizes both the peak and average temperature change, as well as the thermal dose, at the far-field for varying delays.

Table 3: Peak and average temperature change and total dose for each delay at far-field, for sonication in a 10 x 10 grid using acoustical power of 22 W for sonication time of 5 s.

Delay (s)	Peak ΔT (°C)	Average ΔT (°C)	Total dose (CEM43°C)
0	25.5	12.6	77977.3
10	20.4	7.97	2630.4
20	17.3	5.77	293.4
30	10.9	5.89	124.4
40	11.9	5.86	121.4
50	14.8	2.79	41.3
60	6.4	1.99	1.4

Figure 21 shows the thermal dose versus time delay in the far-field for the sequential algorithm.

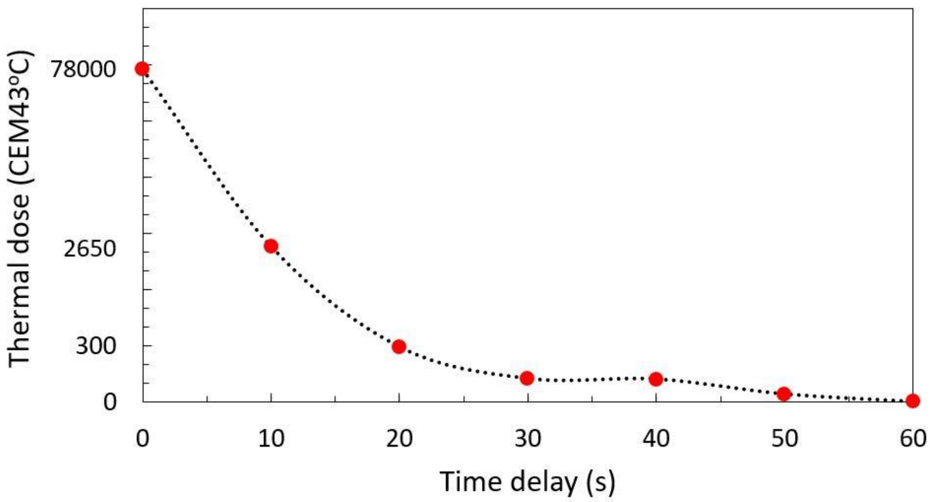

Figure 21: Thermal dose versus delay at far-field (7 cm depth) for sonication in a 10 x 10 grid using acoustical power of 22 W for sonication time of 5 s.

Euler's (Knight's Tour)

In this algorithm, the motion pattern imitates the movement of the "knight" at chess board games. Euler's solution allows "L" shape movements until every point of the 10 x 10 sonicated grid is visited (only once). The sonicated grid is shown in Figure 22.

1	4	31	24	51	6	65	10	53	8
32	23	2	5	64	25	52	7	68	11
3	30	33	50	27	66	69	84	9	54
22	49	28	63	46	85	26	67	12	83
29	34	47	78	61	70	95	82	55	72
48	21	62	45	90	81	86	71	96	13
35	44	79	60	77	94	91	100	73	56
20	41	38	89	80	87	76	93	14	97
39	36	43	18	59	92	99	16	57	74
42	19	40	37	88	17	58	75	98	15

Figure 22: Transducer movement with Euler's (Knight's Tour) algorithm.

The recorded graphs of the temperature versus time for time delays of 0 - 60 s (10 s step) are shown respectively in Figure 23 to Figure 29.

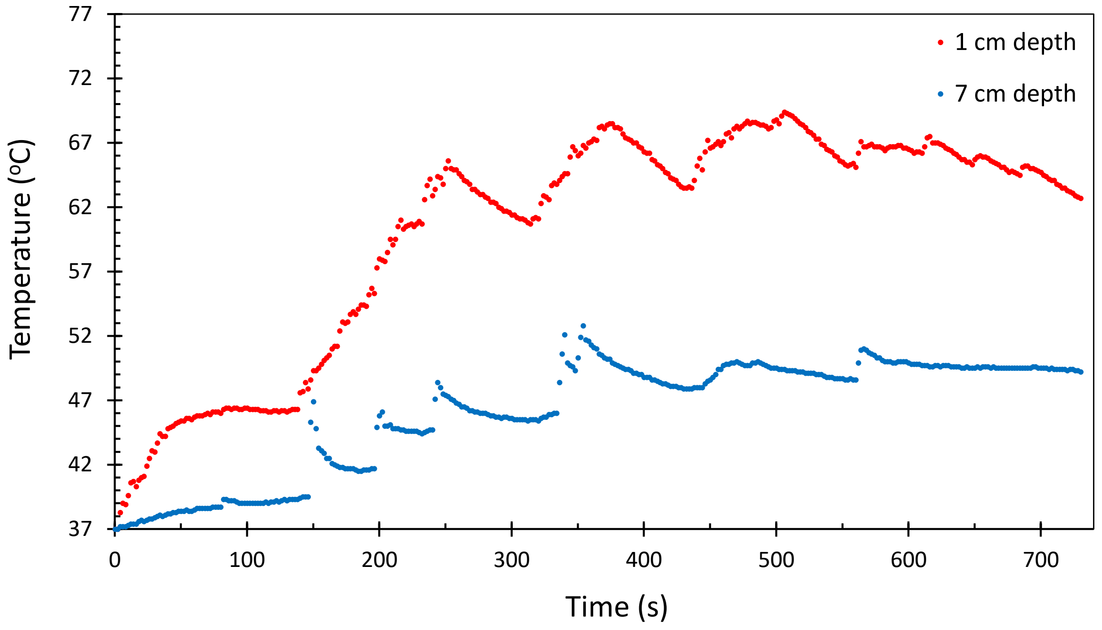

Figure 23: Temperature versus time at near-field (1 cm depth) and far-field (7 cm depth) for sonication in a 10 x 10 grid using acoustical power of 22 W, sonication time of 5 s, and delay of 0 s.

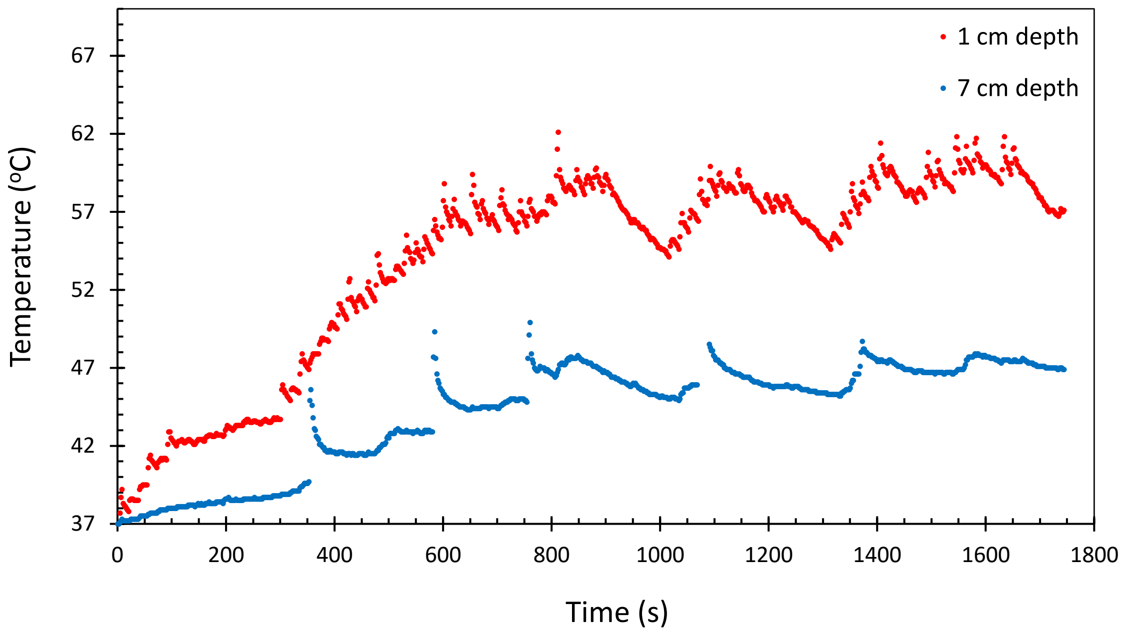

Figure 24: Temperature versus time at near-field (1 cm depth) and far-field (7 cm depth) for sonication in a 10 x 10 grid using acoustical power of 22 W, sonication time of 5 s, and delay 10 s.

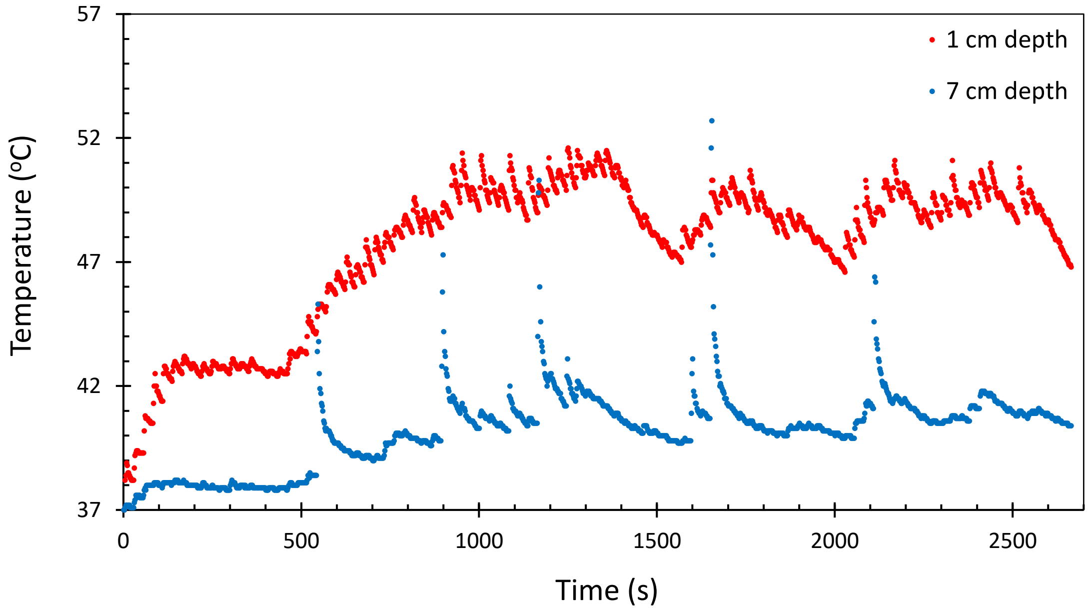

Figure 25: Temperature versus time at near-field (1 cm depth) and far-field (7 cm depth) for sonication in a 10 x 10 grid using acoustical power of 22 W, sonication time of 5 s, and delay of 20 s.

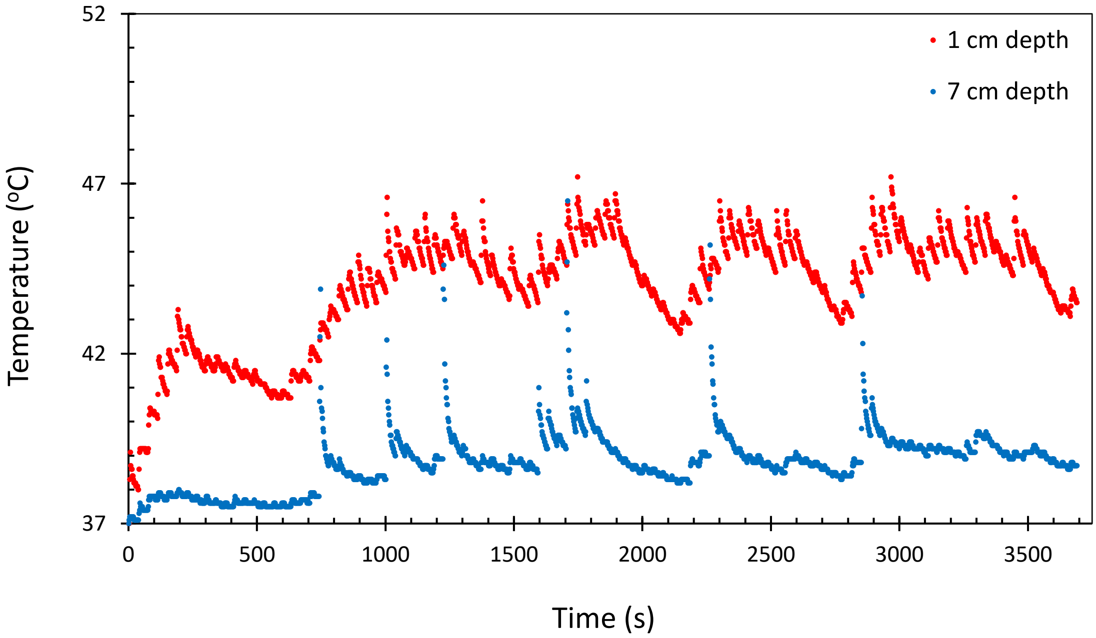

Figure 26: Temperature versus time at near-field (1 cm depth) and far-field (7 cm depth) for sonication in a 10 x 10 grid using acoustical power of 22 W, sonication time of 5 s, and delay of 30 s.

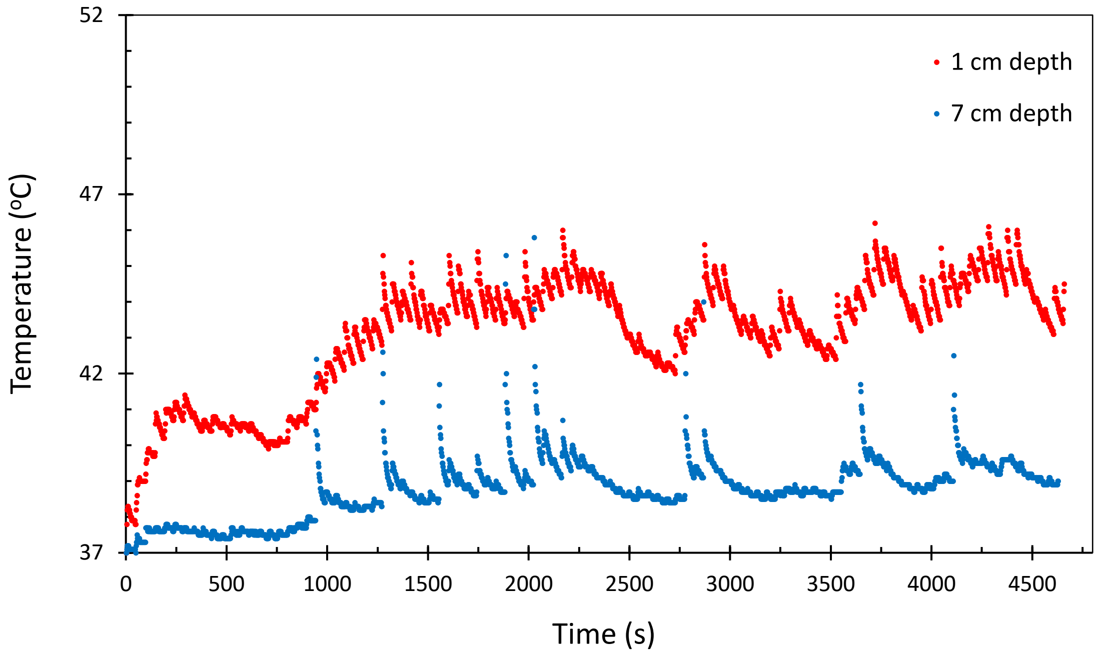

Figure 27: Temperature versus time at near-field (1 cm depth) and far-field (7 cm depth) for sonication in a 10 x 10 grid using acoustical power of 22 W, sonication time of 5 s, and delay of 40 s.

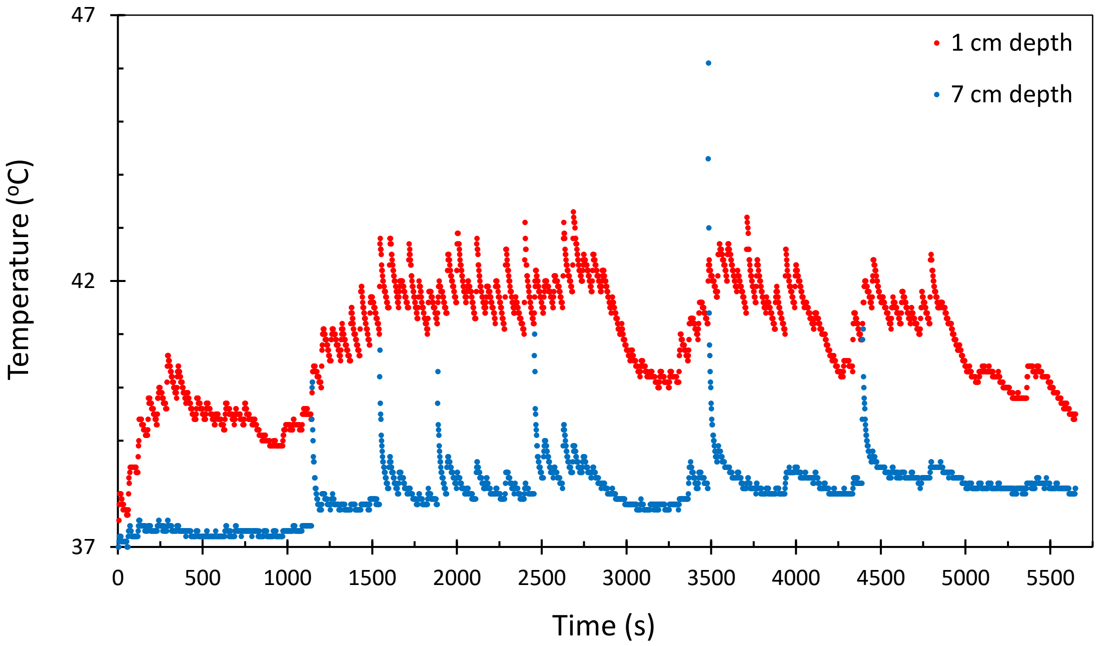

Figure 28: Temperature versus time at near-field (1 cm depth) and far-field (7 cm depth) for sonication in a 10 x 10 grid using acoustical power of 22 W, sonication time of 5 s, and time delay of 50 s.

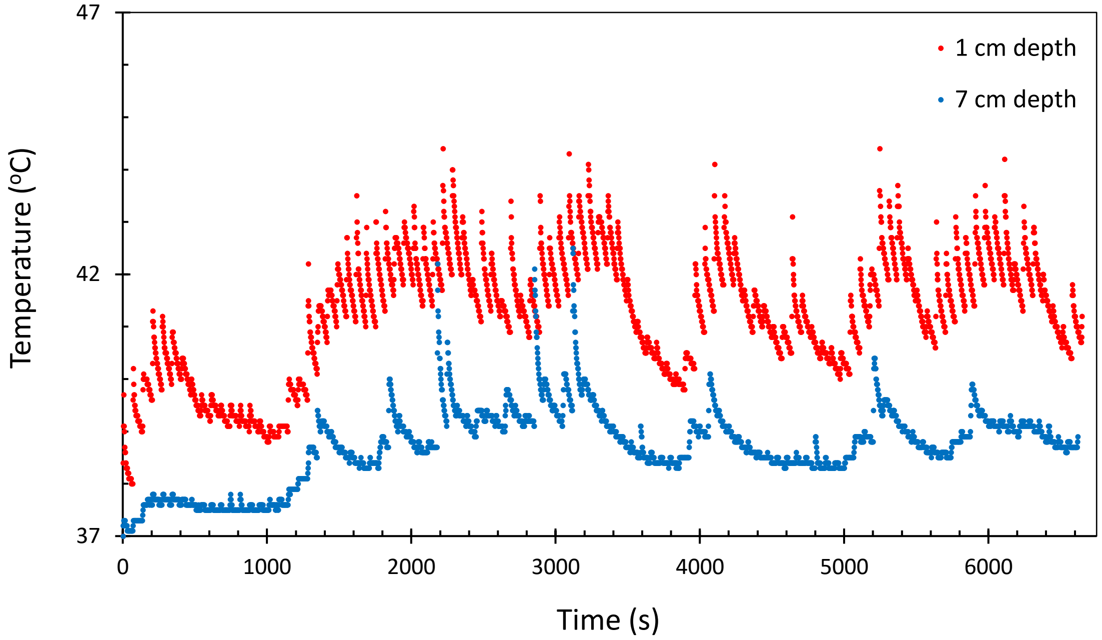

Figure 29: Temperature versus time at near-field (1 cm depth) and far-field (7 cm depth) for sonication in a 10 x 10 grid using acoustical power of 22 W, sonication time of 5 s, and time delay of 60 s.

Figure 30 shows the recorded temperature versus time in the near-field for delays of 0-60 s while Figure 31 shows the corresponding accumulated thermal dose versus delay.

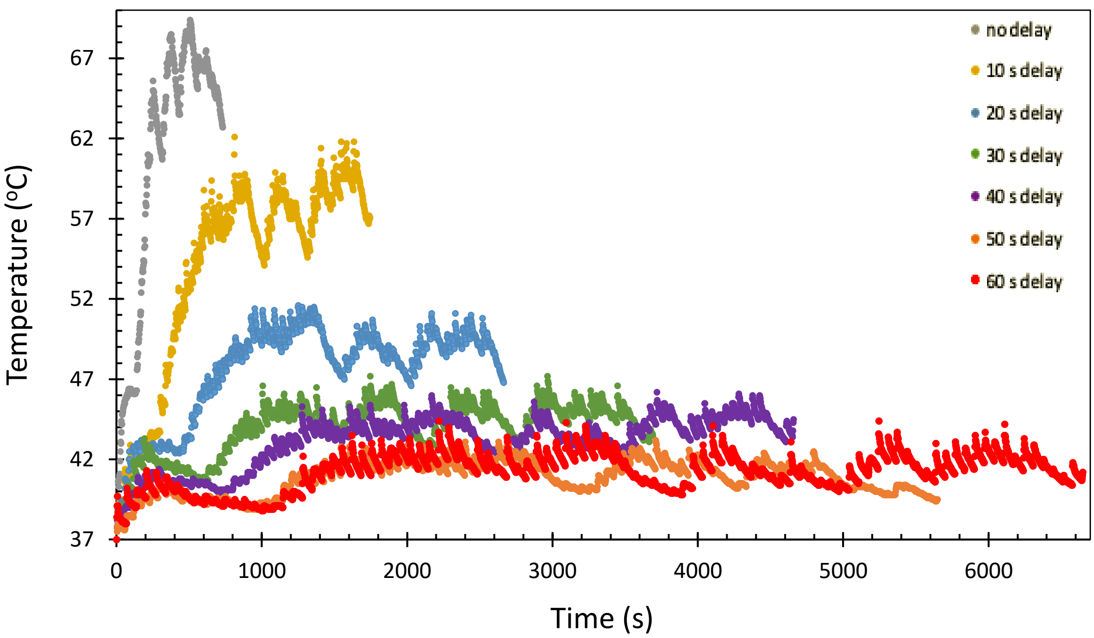

Figure 30: Temperature versus time at near-field (1 cm depth) for sonication in a 10 x 10 grid using acoustical power of 22 W, sonication time of 5 s, and varying delays (Euler's algorithm).

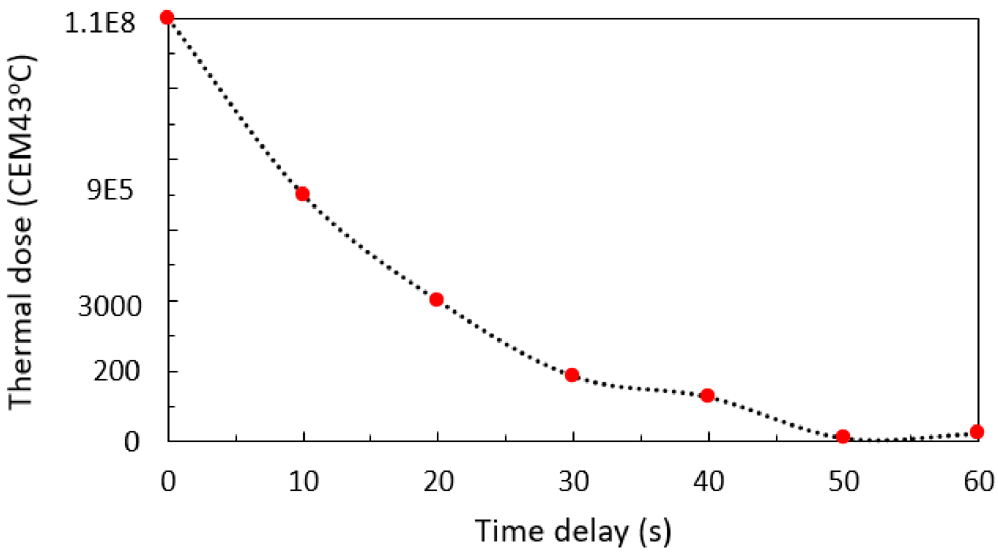

Figure 31: Thermal dose versus delay at near-field (1 cm depth) for sonication in a 10 x 10 grid using acoustical power of 22 W for sonication time of 5 s.

Table 4 summarizes both the peak and average temperature change, as well as the accumulated thermal dose, for each delay at the near-field.

Table 4: Peak and average temperature change and total dose for each delay at near-field, for sonication in a 10 x 10 grid using acoustical power of 22 W for sonication time of 5 s.

Delay (s)	Peak ΔT (°C)	Average ΔT (°C)	Total dose (CEM43°C)
0	32.4	23.18	115629236.4
10	25.1	16.89	944287.2
20	14.6	10.58	3049
30	10.2	6.95	186.7
40	9.2	6.1	127.98
50	6.3	3.86	11.2
60	7.4	4.22	24.1

Figure 32 shows the recorded temperature versus time for the far-field using varying delays of 0-60 s while Figure 33 shows the corresponding thermal dose versus delay.

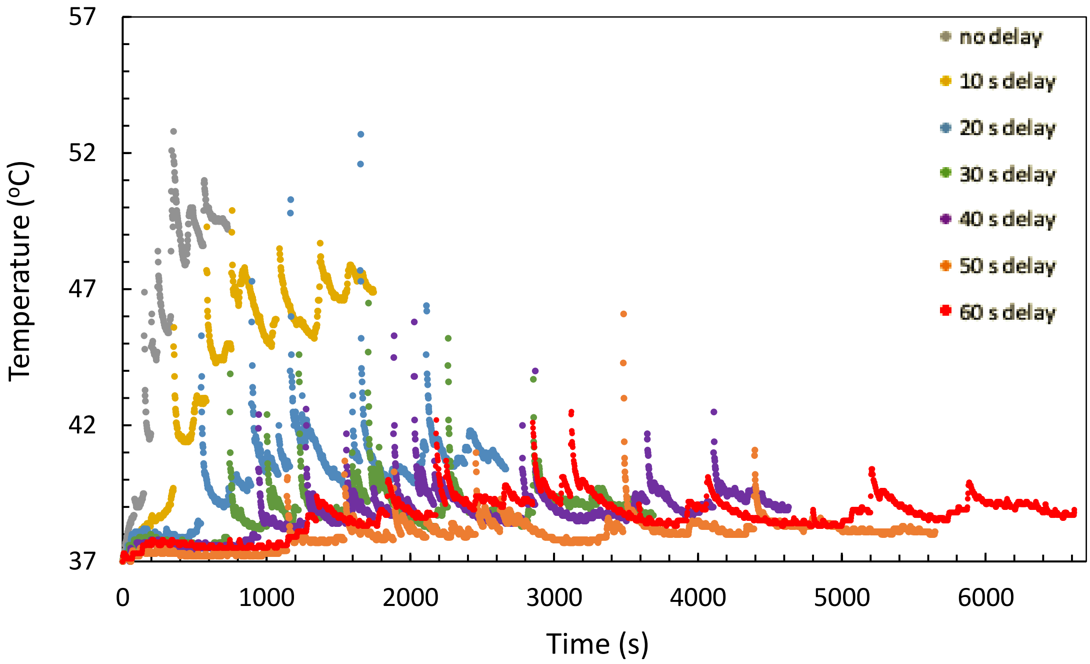

Figure 32: Temperature versus time at far-field (7 cm depth) for sonication in a 10 x 10 grid using acoustical power of 22 W, sonication time of 5 s, and varying delays (Euler's algorithm).

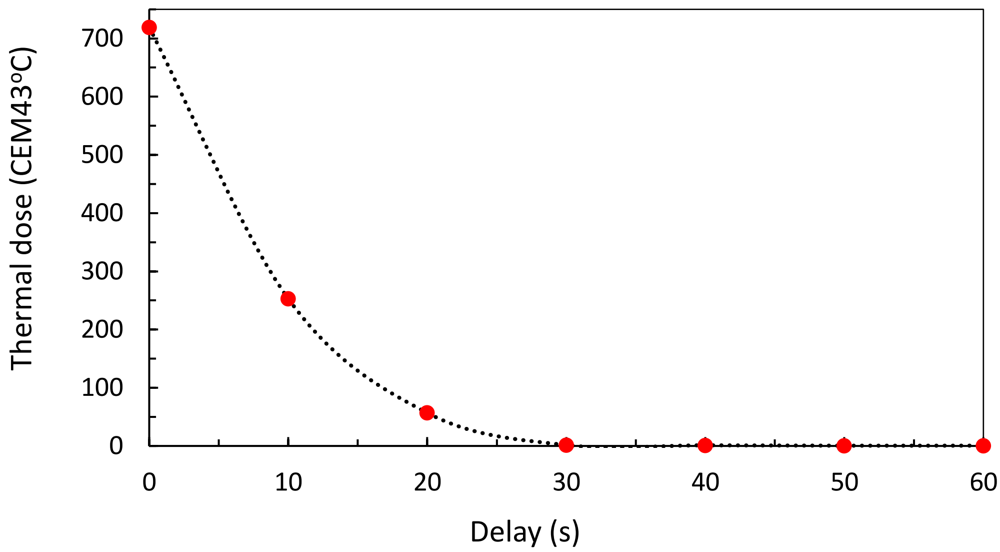

Figure 33: Thermal dose versus delay at far-field (7 cm depth) for sonication in a 10 x 10 grid using acoustical power of 22 W for sonication time of 5 s.

Table 5 summarizes both the peak and average temperature changes, as well as the total thermal dose, for each delay at the far-field.

Table 5: Peak and average temperature change and total dose for each delay at far-field, for sonication in a 10 x 10 grid using acoustical power of 22 W for sonication time of 5 s.

Delay (s)	Peak ΔT (ºC)	Average ΔT (ºC)	Total dose (CEM43^{0}C)
0	15.8	9.08	719.05
10	12.9	7.16	253
20	15.7	3.21	56.8
30	9.5	1.79	1.54
40	8.8	1.76	1.14
50	9.1	1.02	0.53
60	5.5	1.7	0.54

Spiral

In this algorithm, the visiting cells are spread in a concentric grid to reduce the pre-focal heating effect. The sonicated grid is shown in Figure 34. Figure 35 shows a screenshot of the software acquired during execution of the spiral movement.

1	21	41	61	81	2	22	42	62	82
8	28	48	68	88	9	29	49	69	3
87	73	93	14	34	54	74	94	89	23
67	53	77	97	18	38	58	15	10	43
47	33	57	20	40	60	78	35	30	63
27	13	37	99	100	80	98	55	50	83
7	92	17	79	59	39	19	75	70	4
86	72	96	76	56	36	16	95	90	24
66	52	32	12	91	71	51	31	11	44
46	26	6	85	65	45	25	5	84	64

Figure 34: Transducer movement with spiral algorithm.

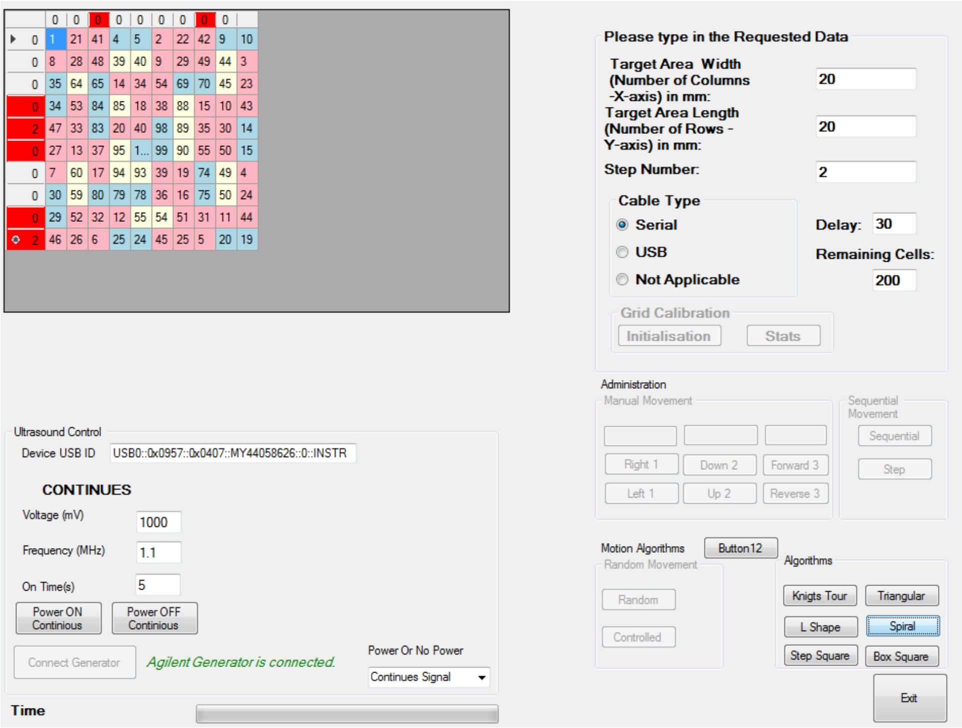

Figure 35: Software screenshot during execution of the spiral algorithm.

The recorded temperature versus time for delays of 0 - 60 s (10 s step) at both near-field and far-field locations is shown respectively in Figure 36 to Figure 42.

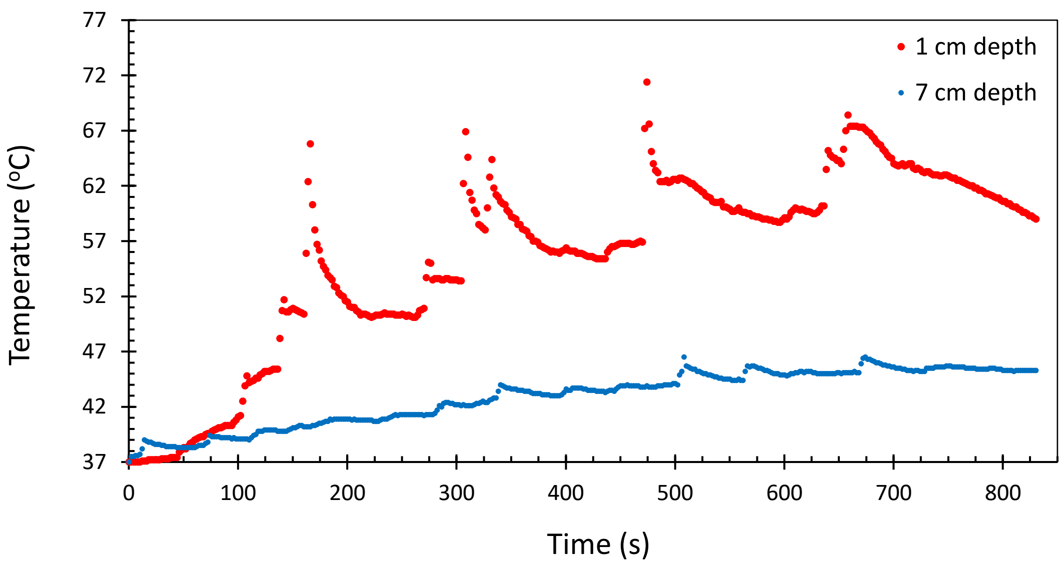

Figure 36: Temperature versus time at near-field (1 cm depth) and far-field (7 cm depth) for sonication in a 10 x 10 grid using acoustical power of 22 W, sonication time of 5 s, and delay of 0 s.

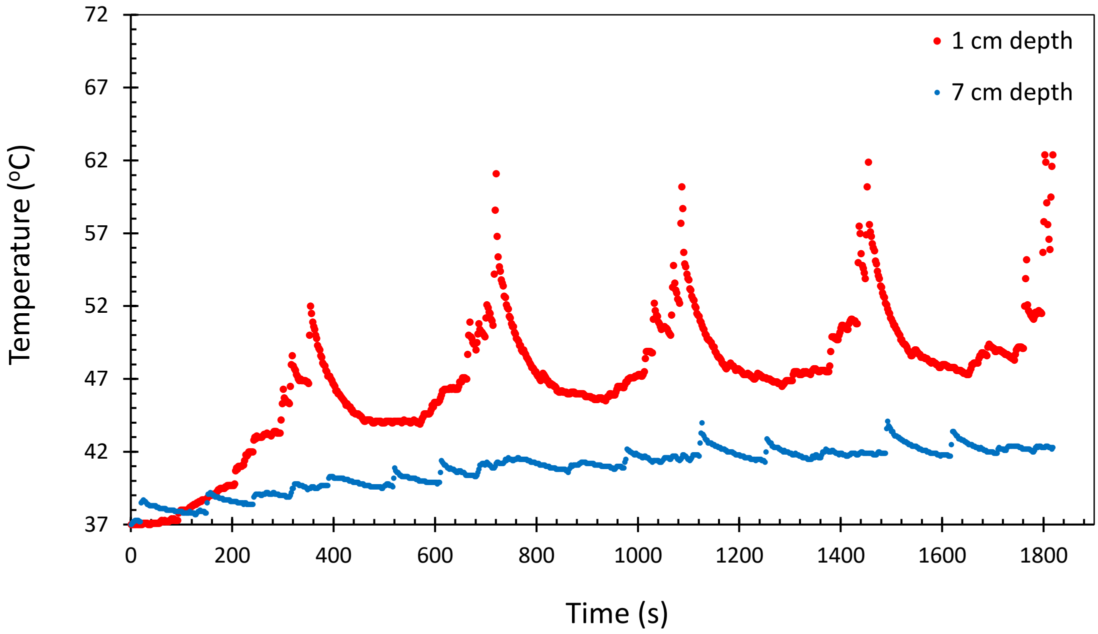

Figure 37: Temperature versus time at near-field (1 cm depth) and far-field (7 cm depth) for sonication in a 10 x 10 grid using acoustical power of 22 W, sonication time of 5 s, and delay 10 s.

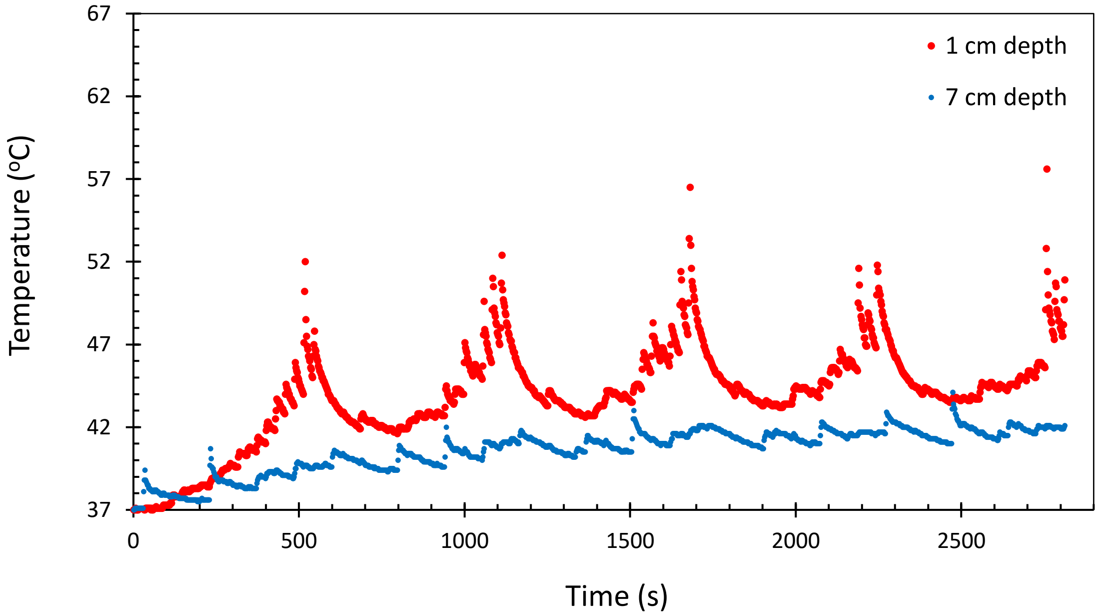

Figure 38: Temperature versus time at near-field (1 cm depth) and far-field (7 cm depth) for sonication in a 10 x 10 grid using acoustical power of 22 W, sonication time of 5 s, and delay of 20 s.

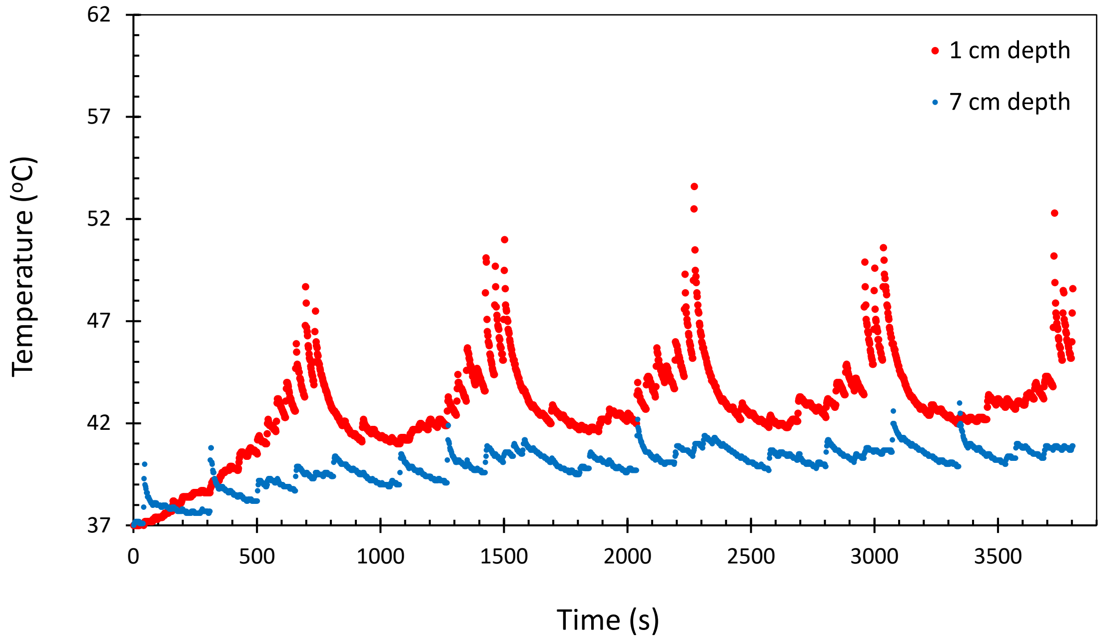

Figure 39: Temperature versus time at near-field (1 cm depth) and far-field (7 cm depth) for sonication in a 10 x 10 grid using acoustical power of 22 W, sonication time of 5 s, and delay of 30 s.

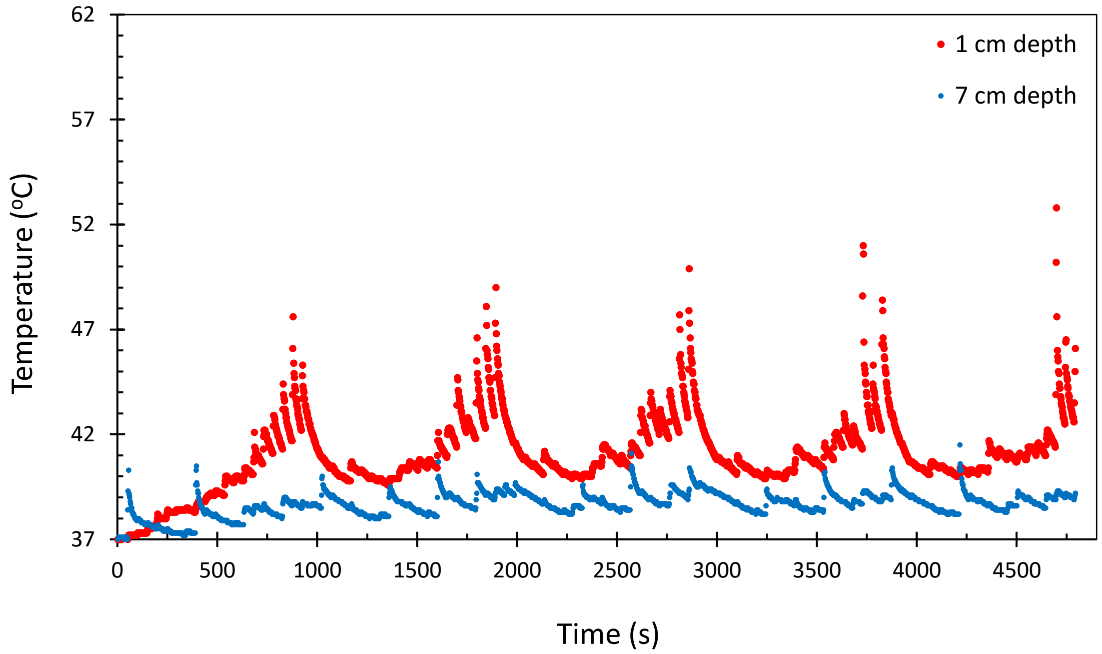

Figure 40: Temperature versus time at near-field (1 cm depth) and far-field (7 cm depth) for sonication in a 10 x 10 grid using acoustical power of 22 W, sonication time of 5 s, and delay of 40 s.

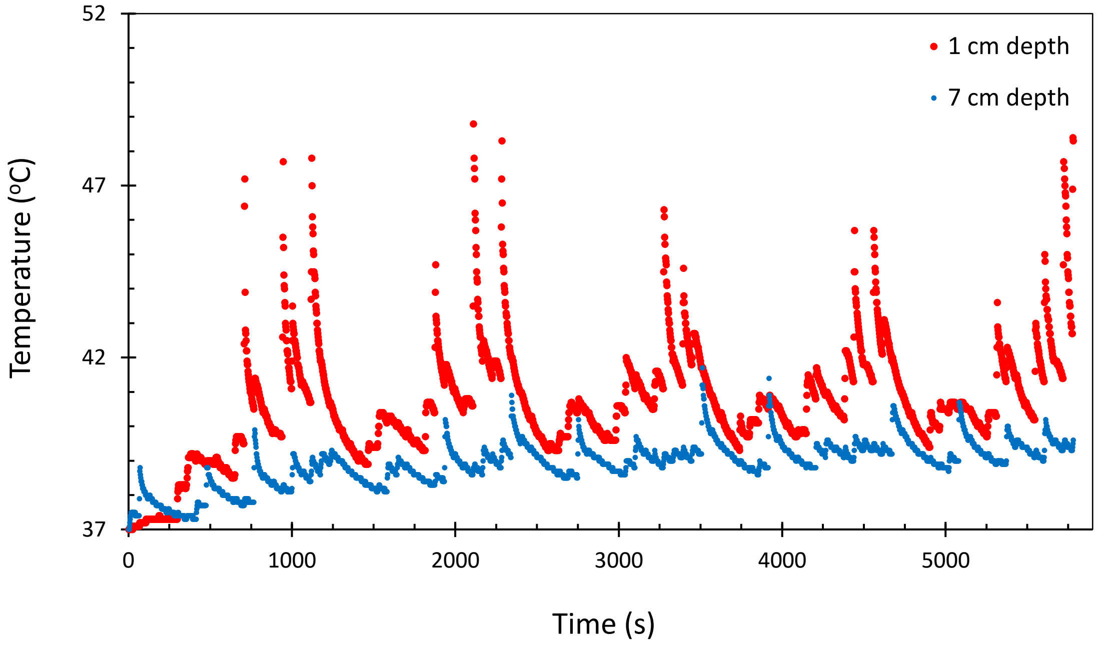

Figure 41: Temperature versus time at near-field (1 cm depth) and far-field (7 cm depth) for sonication in a 10 x 10 grid using acoustical power of 22 W, sonication time of 5 s, and delay of 50 s.

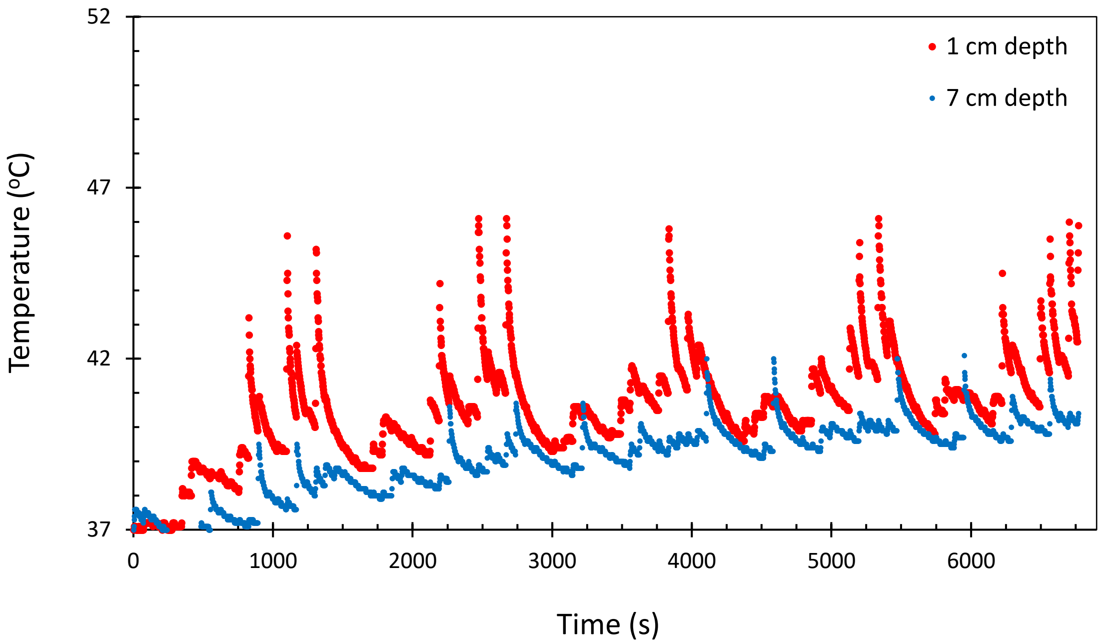

Figure 42: Temperature versus time at near-field (1 cm depth) and far-field (7 cm depth) for sonication in a 10 x 10 grid using acoustical power of 22 W, sonication time of 5 s, and delay of 60 s.

Figure 43 shows the recorded temperature versus time in the near-field for various delays of 0 – 60 s while Figure 44 shows the corresponding thermal dose versus delay.

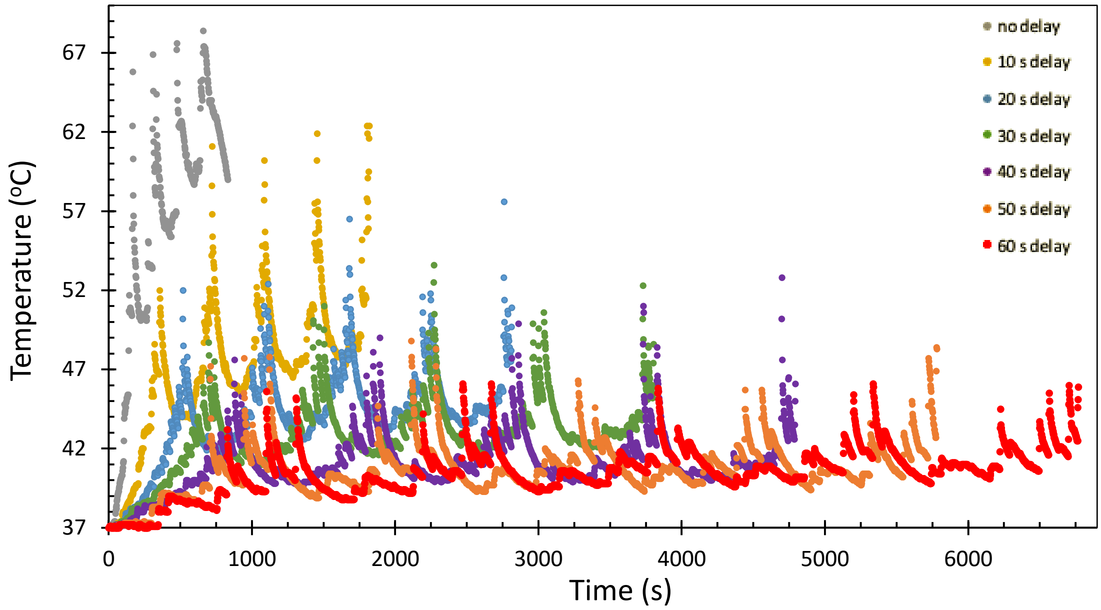

Figure 43: Temperature versus time at near-field (1 cm depth) for sonication in a 10 x 10 grid using acoustical power of 22 W, sonication time of 5 s, and varying delays (Spiral algorithm).

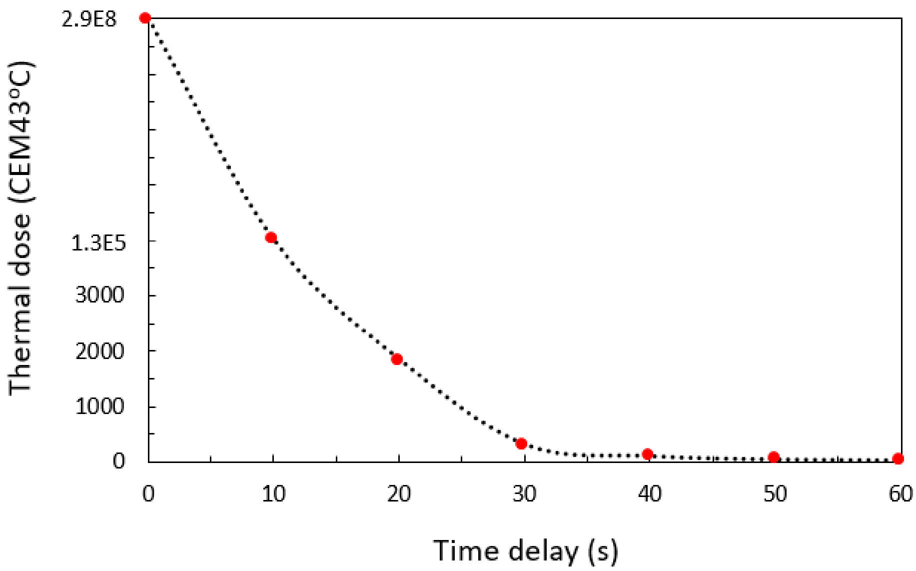

Figure 44: Thermal dose versus delay at near-field (1 cm depth) for sonication in a 10 x 10 grid using acoustical power of 22 W for sonication time of 5 s.

Table 6 summarizes both the peak and average temperature change, as well as the induced thermal dose, for each delay at the near-field.

Table 6: Peak and average temperature change and total dose for each delay at near-field, for sonication in a 10 x 10 grid using acoustical power of 22 W for sonication time of 5 s.

Delay (s)	Peak ΔT (ºC)	Average ΔT (ºC)	Total dose (CEM43^{0}C)
0	34.4	18.6	28933635.2
10	25.4	9.95	133808.7
20	20.6	6.9	1845.2
30	16.6	5.7	306
40	15.8	4.01	98.4
50	11.8	3.64	37.9
60	9.1	3.51	22.4

Figure 45 shows a graph of the recorded temperature versus time in the far-field for the various delays of 0 - 60 s while Figure 46 shows the corresponding thermal dose versus delay.

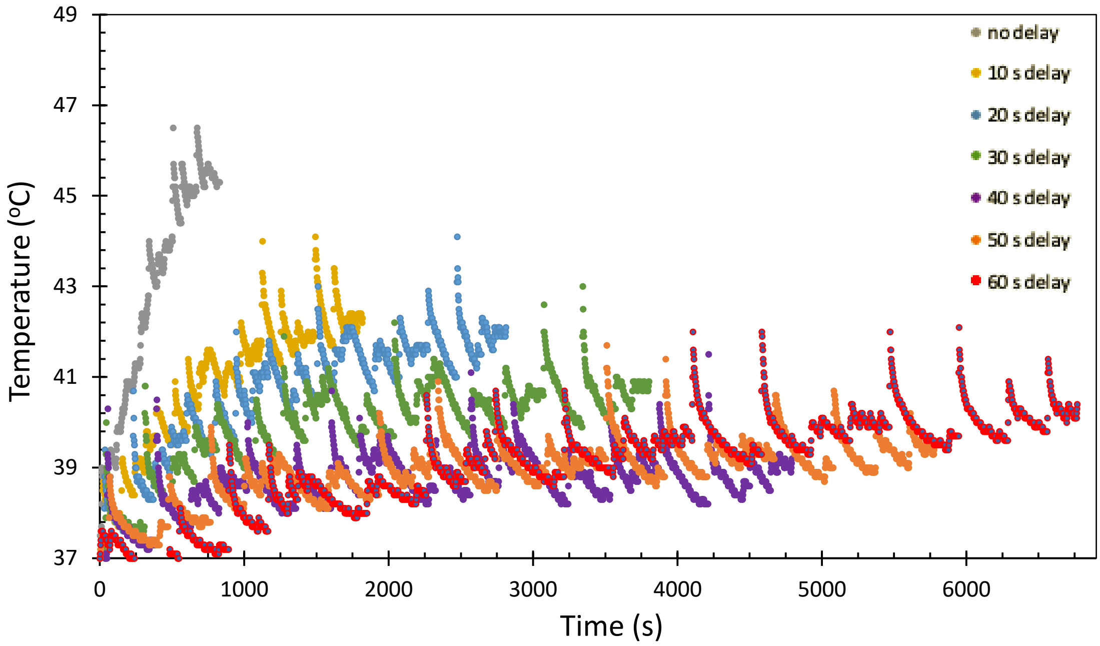

Figure 45: Temperature versus time at far-field (7 cm depth) for sonication in a 10 x 10 grid using acoustical power of 22 W, sonication time of 5 s, and varying delays (Spiral algorithm).

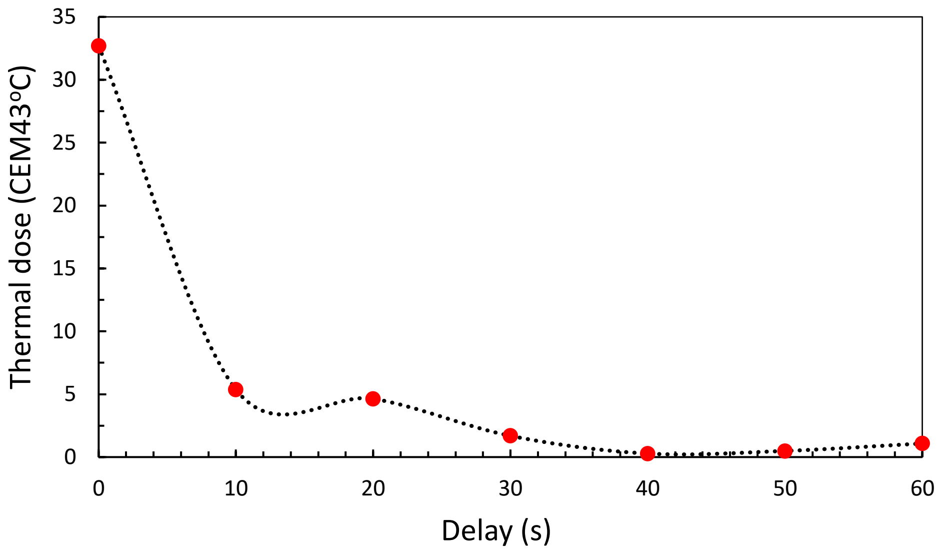

Figure 46: Thermal dose versus delay at far-field (7 cm depth) for sonication in a 10 x 10 grid using acoustical power of 22 W for sonication time of 5 s.

Table 7 summarizes both the peak and average temperature changes, as well as the total thermal dose, for each time delay at the far-field (Spiral algorithm).

Table 7: Peak and average temperature change and total dose for each delay at far-field, for sonication in a 10 x 10 grid using acoustical power of 22 W for sonication time of 5 s.

Delay (s)	Peak ΔT (ºC)	Average ΔT (ºC)	Total dose (CEM43^{0}C)
0	9.5	5.89	32.69
10	7.1	3.88	5.37
20	7.1	3.62	4.64
30	6	2.93	1.69
40	4.5	1.68	0.28
50	4.7	1.91	0.49
60	5.1	2.06	1.08

Square

In this algorithm, the motion is based on the concept of concentric “squares”. Each square is inscribed in another square, with its dimensions reduced by one row and one column. The sonicated grid is shown in Figure 47.

1	21	37	53	65	77	85	93	97	2
99	5	25	41	57	69	81	89	6	22
95	91	9	29	45	61	73	10	26	38
87	83	75	13	33	49	14	30	42	54
79	71	63	51	17	18	34	46	58	66
67	59	47	35	19	20	50	62	70	78
55	43	31	15	52	36	16	74	82	86
39	27	11	76	64	48	32	12	90	94
23	7	92	84	72	60	44	28	8	98
3	100	96	88	80	68	56	40	24	4

Figure 27: Transducer movement with box-square algorithm.

Figure 48 shows a screenshot of the software acquired during execution of the box-square movement.

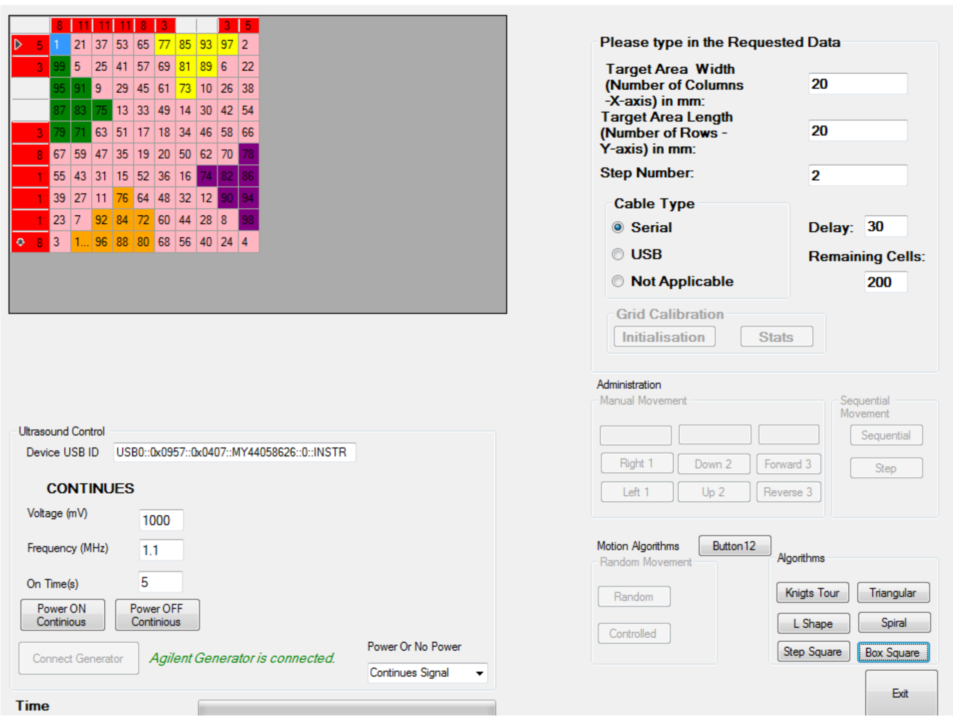

Figure 48: Software screenshot during execution of the box-square algorithm.

The recorded temperature versus time in the near and far-field for delays of 0 - 60 s (10 s step) is shown respectively in Figure 49 to Figure 55.

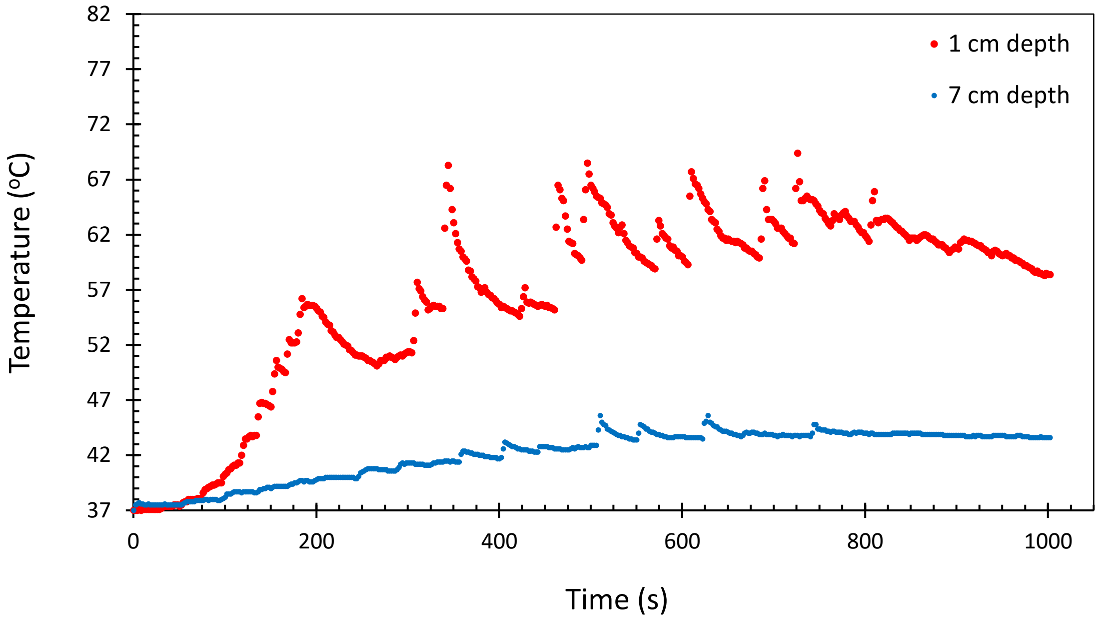

Figure 49: Temperature versus time at near-field (1 cm depth) and far-field (7 cm depth) for sonication in a 10 x 10 grid using acoustical power of 22 W, sonication time of 5 s, and delay of 0 s.

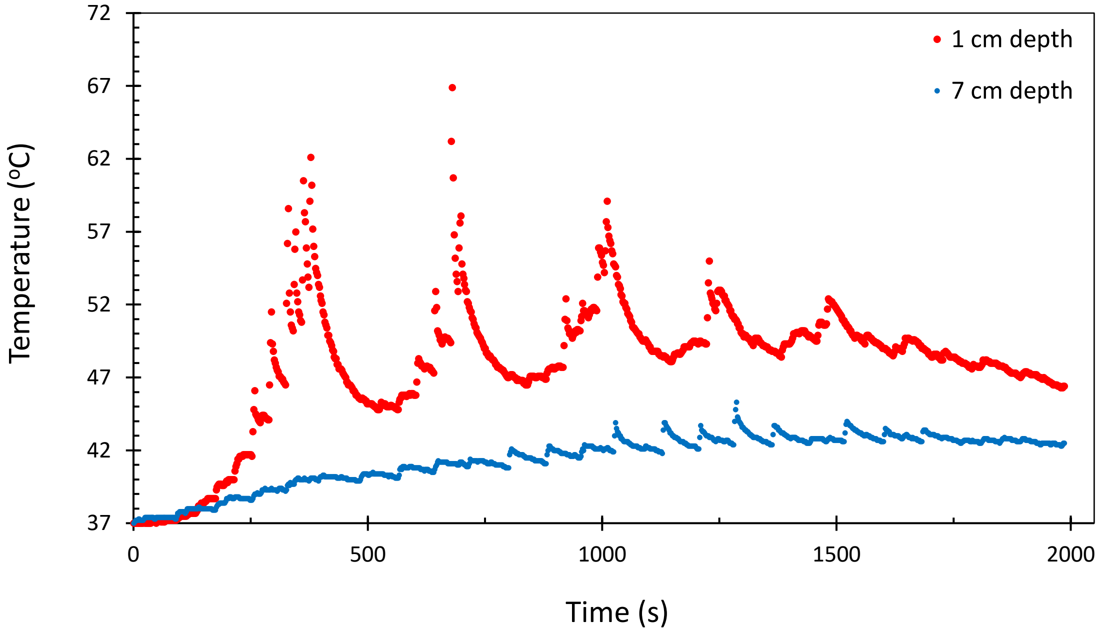

Figure 50: Temperature versus time at near-field (1 cm depth) and far-field (7 cm depth) for sonication in a 10 x 10 grid using acoustical power of 22 W, sonication time of 5 s, and delay 10 s.

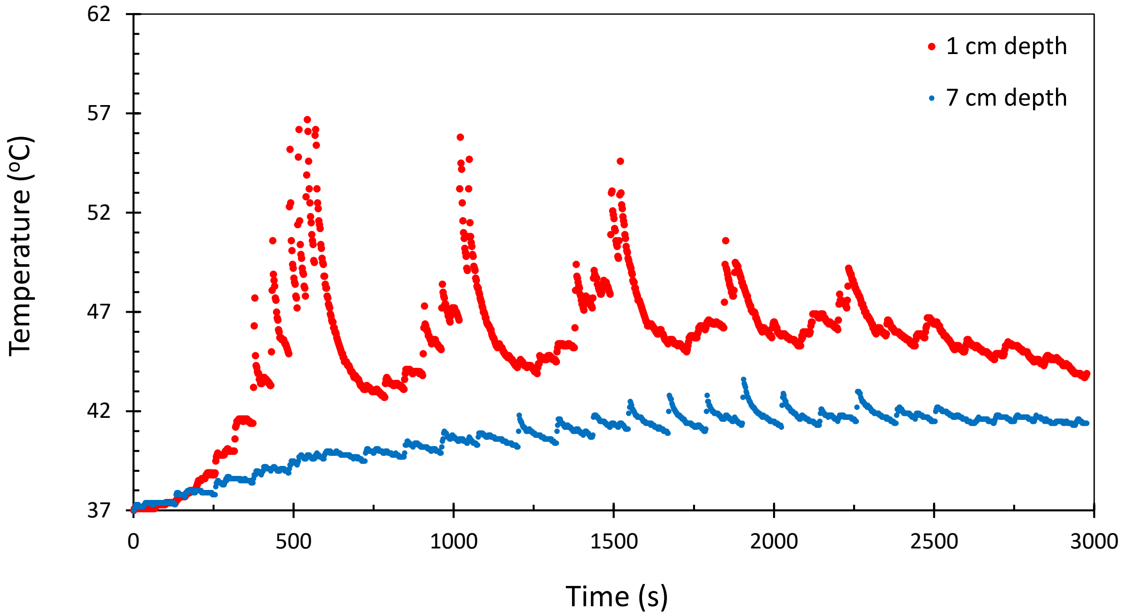

Figure 51: Temperature versus time at near-field (1 cm depth) and far-field (7 cm depth) for sonication in a 10 x 10 grid using acoustical power of 22 W, sonication time of 5 s, and delay of 20 s.

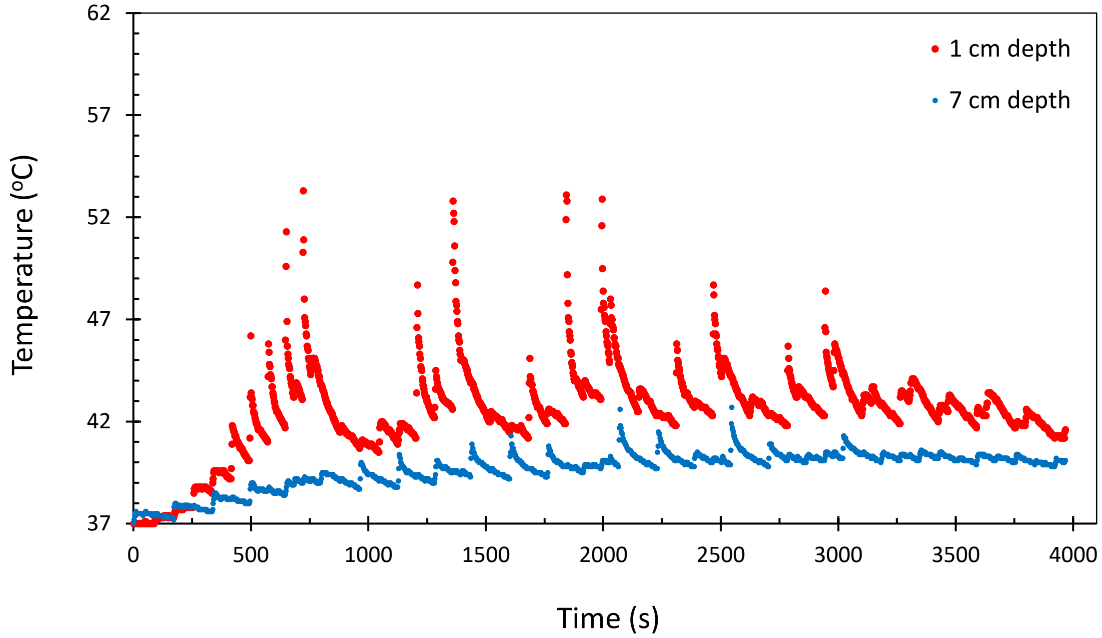

Figure 52: Temperature versus time at near-field (1 cm depth) and far-field (7 cm depth) for sonication in a 10 x 10 grid using acoustical power of 22 W, sonication time of 5 s, and delay of 30 s.

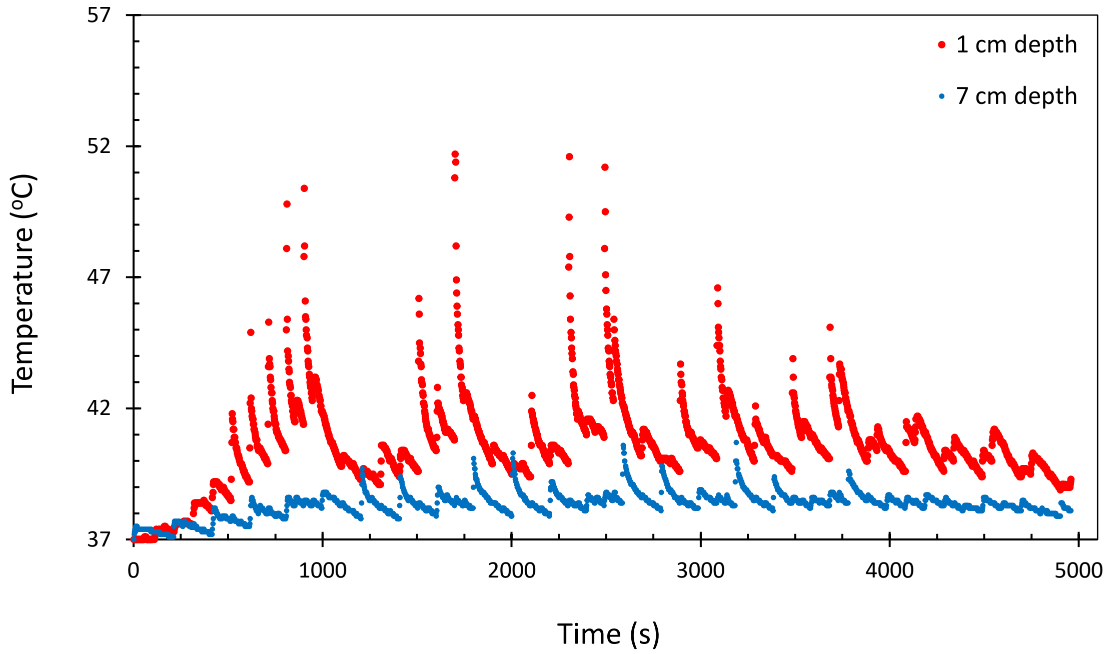

Figure 53: Temperature versus time at near-field (1 cm depth) and far-field (7 cm depth) for sonication in a 10 x 10 grid using acoustical power of 22 W, sonication time of 5 s, and delay of 40 s.

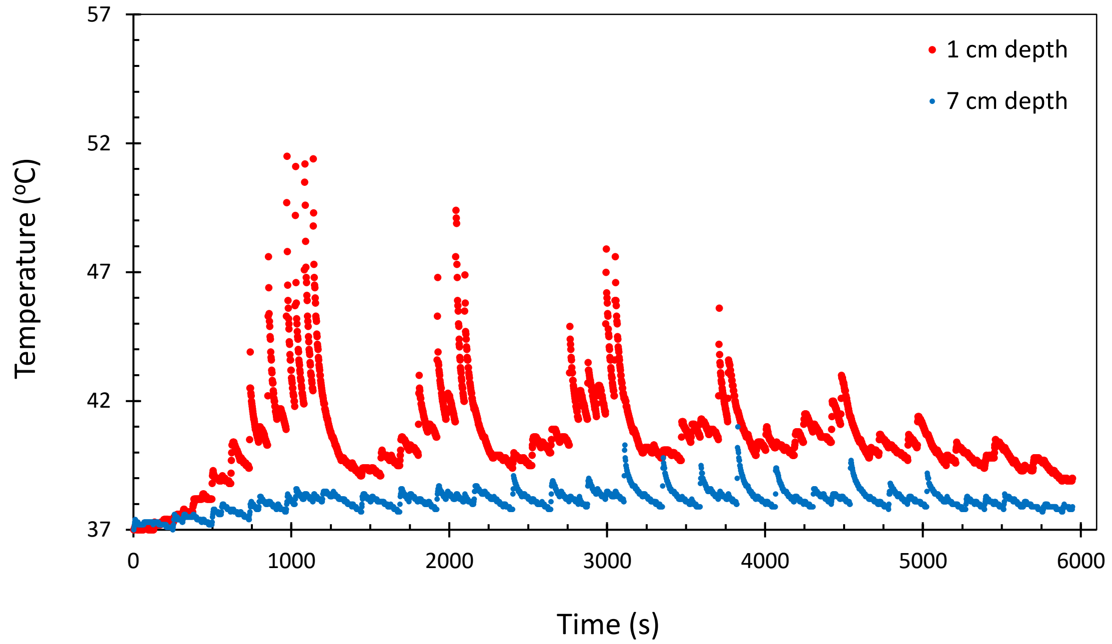

Figure 54: Temperature versus time at near-field (1 cm depth) and far-field (7 cm depth) for sonication in a 10 x 10 grid using acoustical power of 22 W, sonication time of 5 s, and delay of 50 s.

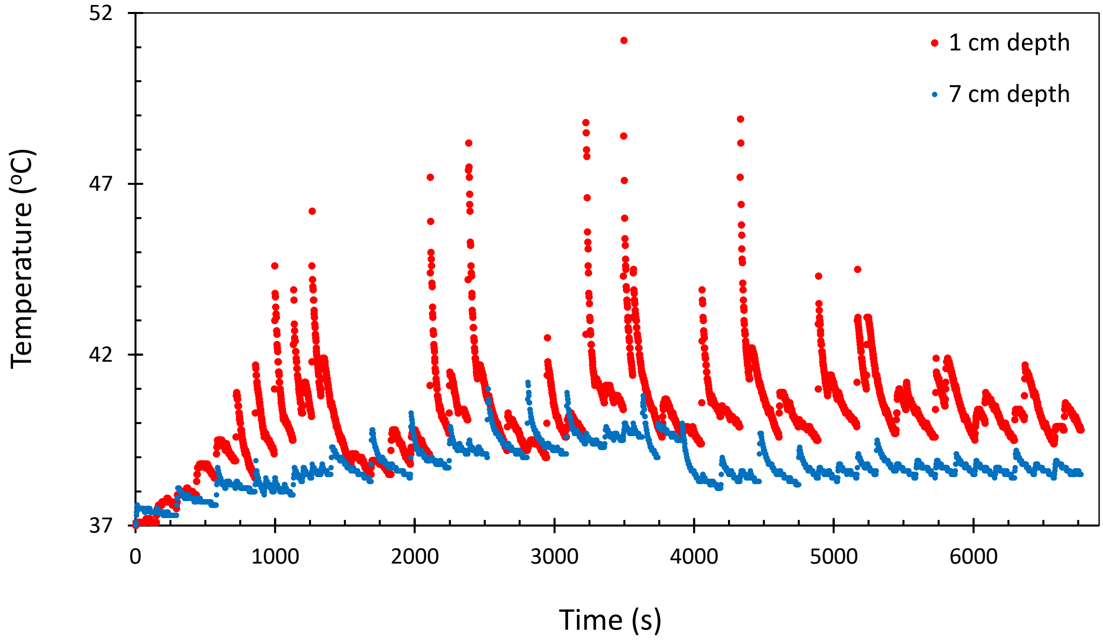

Figure 55: Temperature versus time at near-field (1 cm depth) and far-field (7 cm depth) for sonication in a 10 x 10 grid using acoustical power of 22 W, sonication time of 5 s, and time delay of 60 s.

Figure 56 shows a graph of the recorded temperature versus time in the near-field for the various delays of 0 - 60 s while Figure 57 shows the corresponding thermal dose versus delay.

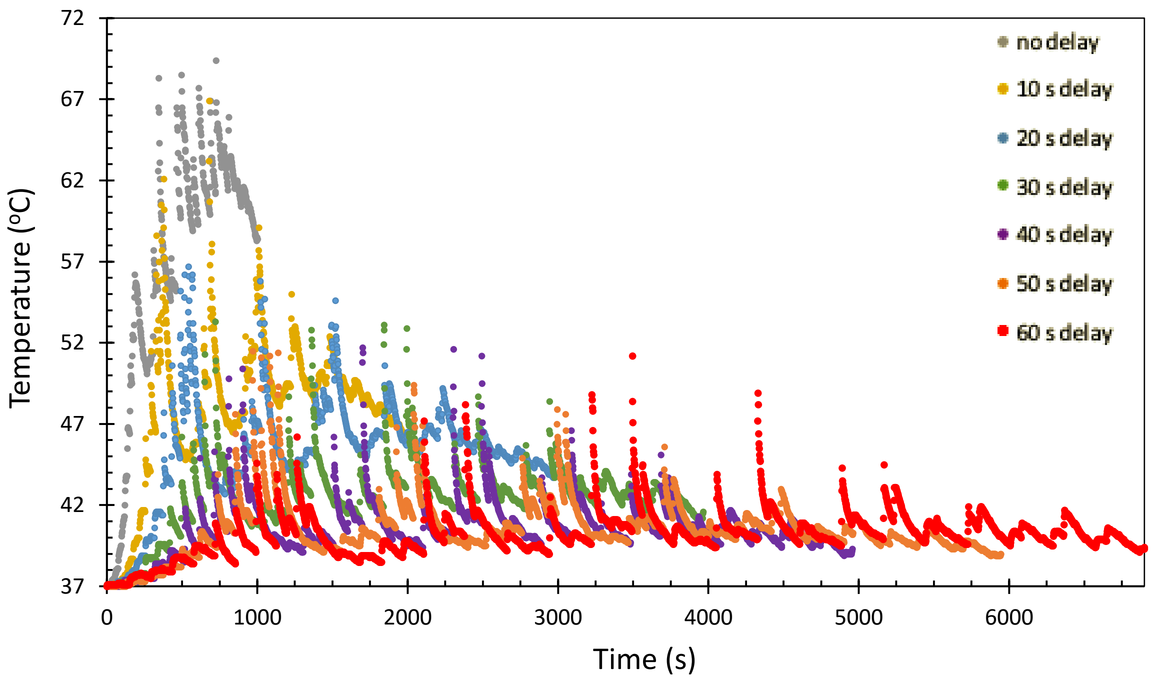

Figure 56: Temperature versus time at near-field (1 cm depth) for sonication in a 10 x 10 grid using acoustical power of 22 W, sonication time of 5 s, and varying delays (Square algorithm).

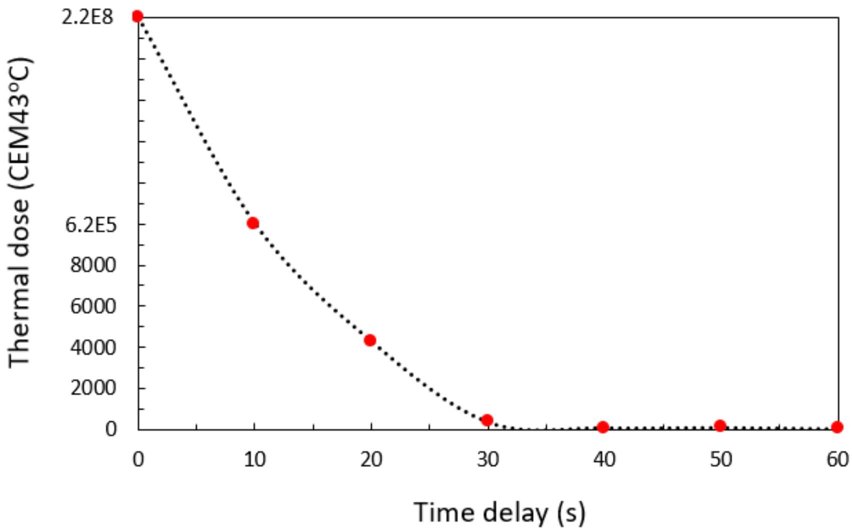

Figure 57: Thermal dose versus delay at near-field (1 cm depth) for sonication in a 10 x 10 grid using acoustical power of 22 W for sonication time of 5 s.

Table 8 summarizes both the peak and average temperature changes, as well as induced thermal dose, for each delay at the near-field (Square algorithm).

Table 8: Peak and average temperature change and total dose for each delay at near-field, for sonication in a 10 x 10 grid using acoustical power of 22 W for sonication time of 5 s.

Delay (s)	Peak ΔT (°C)	Average ΔT (°C)	Total dose (CEM43^{0}C)
0	32.4	19.43	22420020.6
10	29.9	10.82	622325.1
20	19.7	8.23	4282.8
30	16.3	5.46	372.8
40	14.7	3.57	96.24
50	14.5	3.51	104.62
60	14.2	3.22	40.17

Figure 58 shows a graph of the recorded temperature versus time in the far-field for the various delays of 0 - 60 s while Figure 59 shows the corresponding thermal dose versus delay.

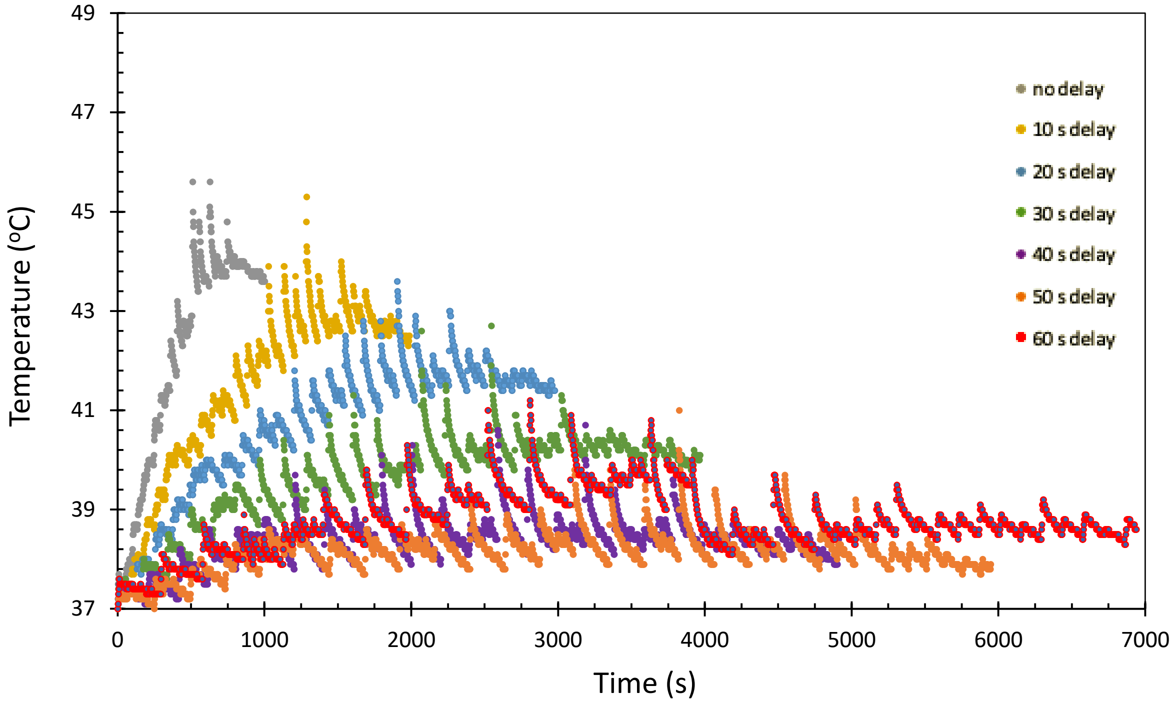

Figure 58: Temperature versus time at far-field (7 cm depth) for sonication in a 10 x 10 grid using acoustical power of 22 W, sonication time of 5 s, and varying delays (Square algorithm).

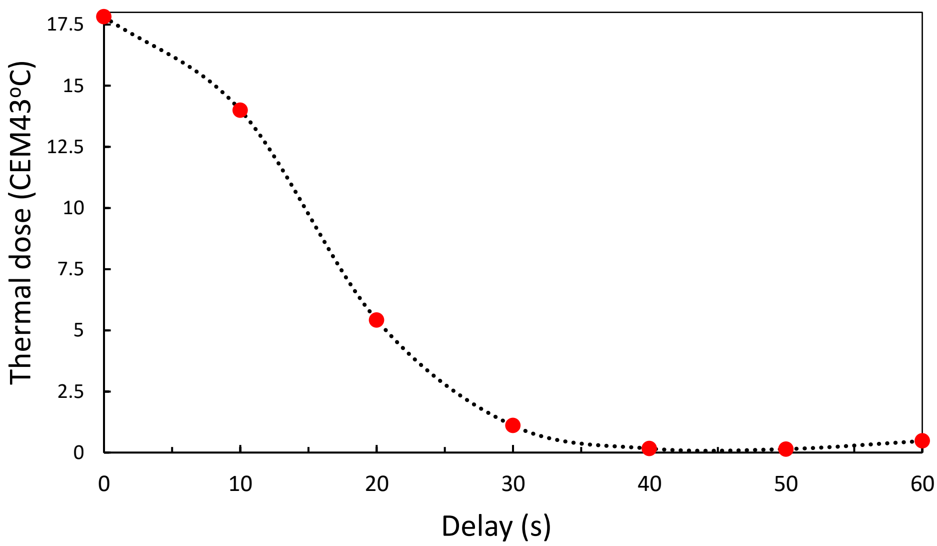

Figure 59: Thermal dose versus delay at far-field (7 cm depth) for sonication in a 10 x 10 grid using acoustical power of 22 W for sonication time of 5 s.

Table 9 summarizes both the peak and average temperature changes, as well as the total thermal dose, for each delay at the far-field (Square algorithm).

Table 9: Peak and average temperature change and total dose for each delay at far-field, for sonication in a 10 x 10 grid using acoustical power of 22 W for sonication time of 5 s.

Delay (s)	Peak ΔT (ºC)	Average ΔT (ºC)	Total dose (CEM43^{0}C)
0	8.6	5.10	17.82
10	8.3	4.40	14
20	6.6	3.68	5.42
30	5.7	2.64	1.1
40	3.7	1.34	0.164
50	4	1.13	0.142
60	4.2	1.74	0.472

Random

In this algorithm, random movement is performed depending on the output value of a random function. A random number is generated and checked whether it has already been created; if not, the positioning device is moved to that location. Otherwise, a new random number is generated. A random sonicated grid is shown in Figure 60.

100	45	88	84	58	47	26	59	64	83
92	63	12	65	42	75	50	99	19	1
70	39	17	95	38	77	40	60	86	16
7	91	18	61	24	6	8	72	66	32
15	35	49	80	27	73	90	76	51	97
10	94	98	41	20	69	4	28	22	3
13	37	29	81	56	30	2	96	53	82
74	5	57	71	85	9	23	52	33	44
78	21	68	89	46	31	62	79	48	55
93	54	67	36	87	34	43	11	25	14

Figure 60: Transducer movement with random algorithm.

Figure 61 shows a screenshot of the software acquired during execution of the random movement.

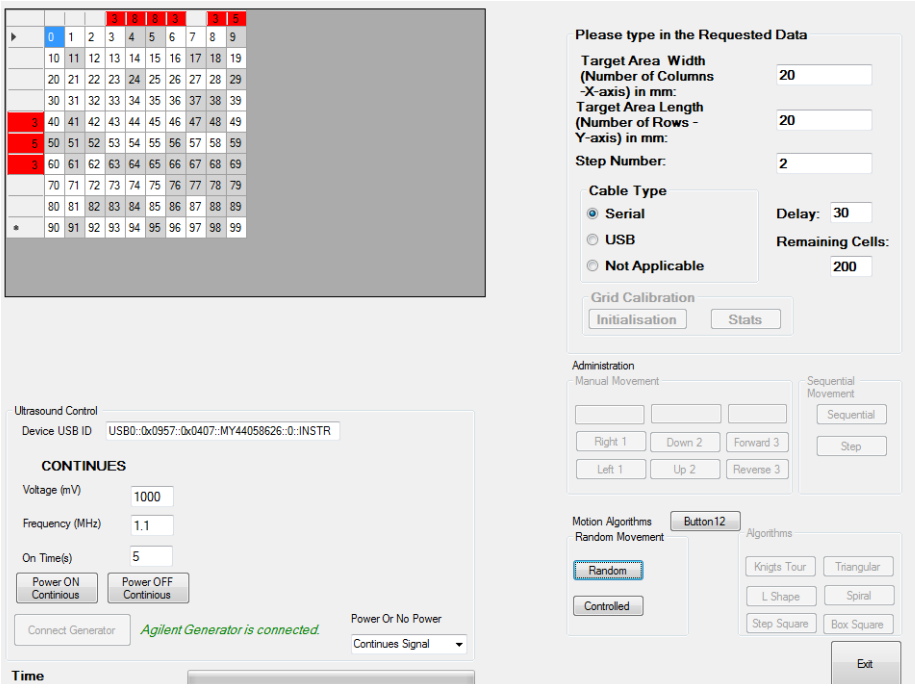

Figure 61: Software screenshot during execution of the random algorithm.

The recorded temperature versus time in the near and far-field for delays of 0 - 60 s (10 s step) is shown respectively in Figure 62 to Figure 68.

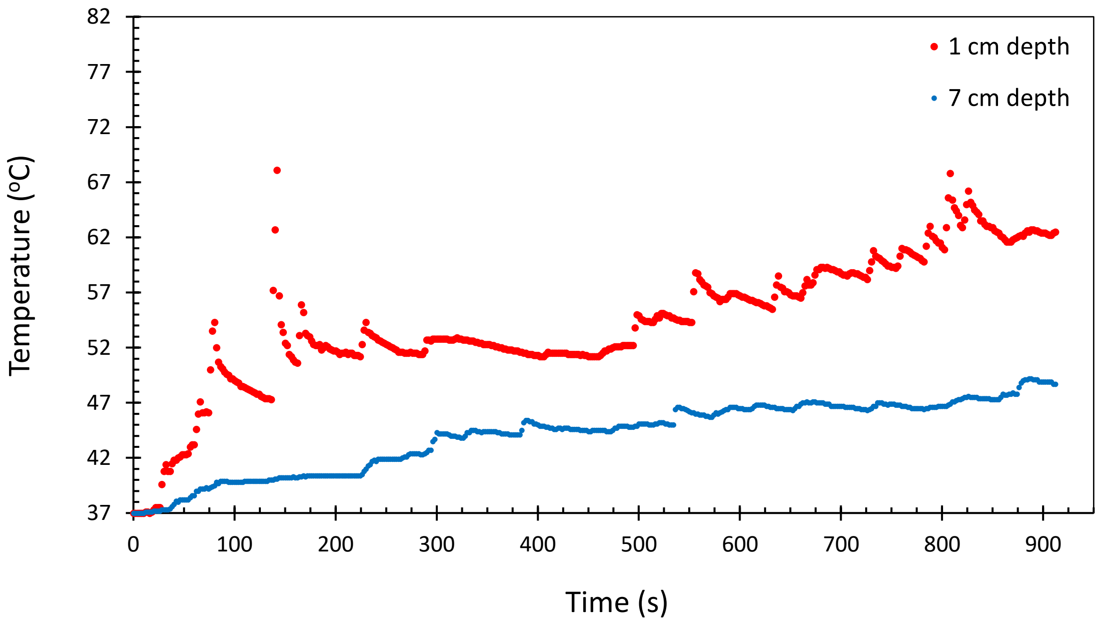

Figure 62: Temperature versus time at near-field (1 cm depth) and far-field (7 cm depth) for sonication in a 10 x 10 grid using acoustical power of 22 W, sonication time of 5 s, and delay of 0 s.

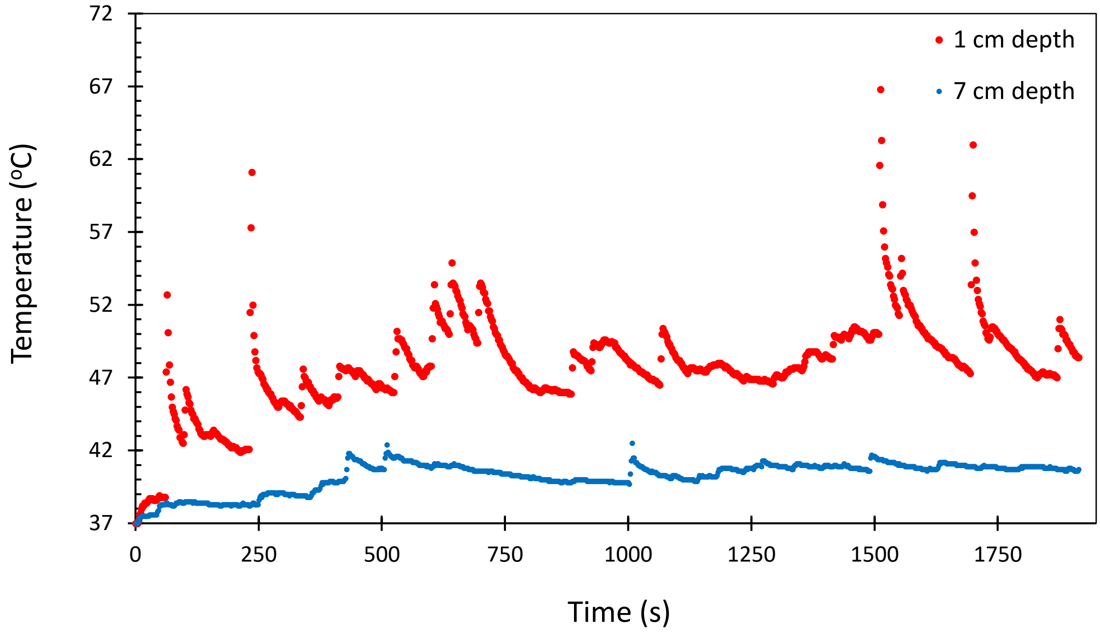

Figure 63: Temperature versus time at near-field (1 cm depth) and far-field (7 cm depth) for sonication in a 10 x 10 grid using acoustical power of 22 W, sonication time of 5 s, and delay of 10 s.

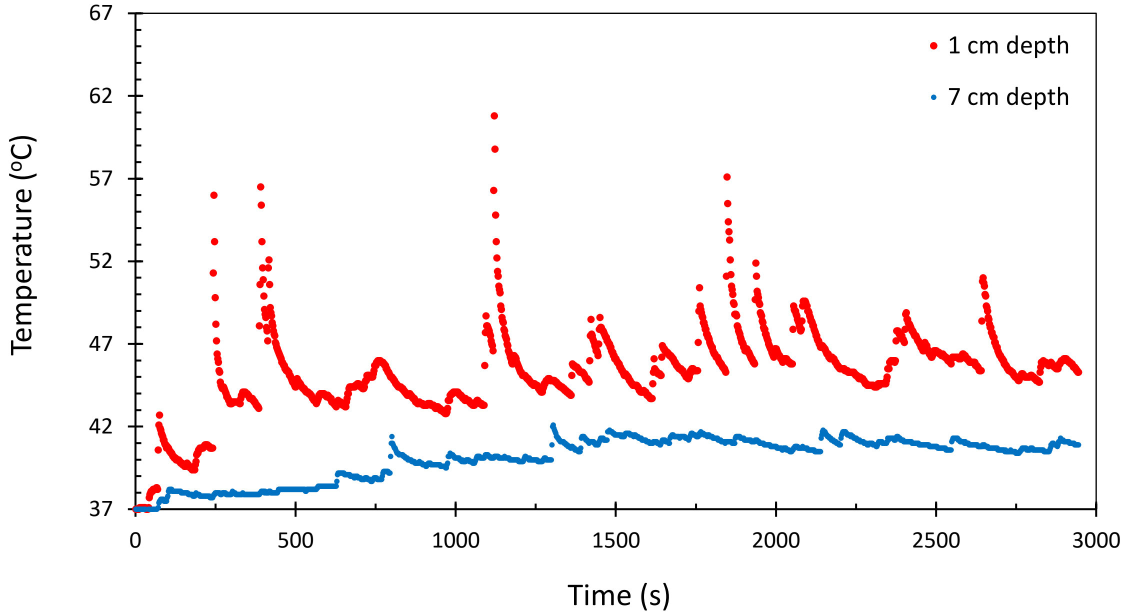

Figure 64: Temperature versus time at near-field (1 cm depth) and far-field (7 cm depth) for sonication in a 10 x 10 grid using acoustical power of 22 W, sonication time of 5 s, and delay of 20 s.

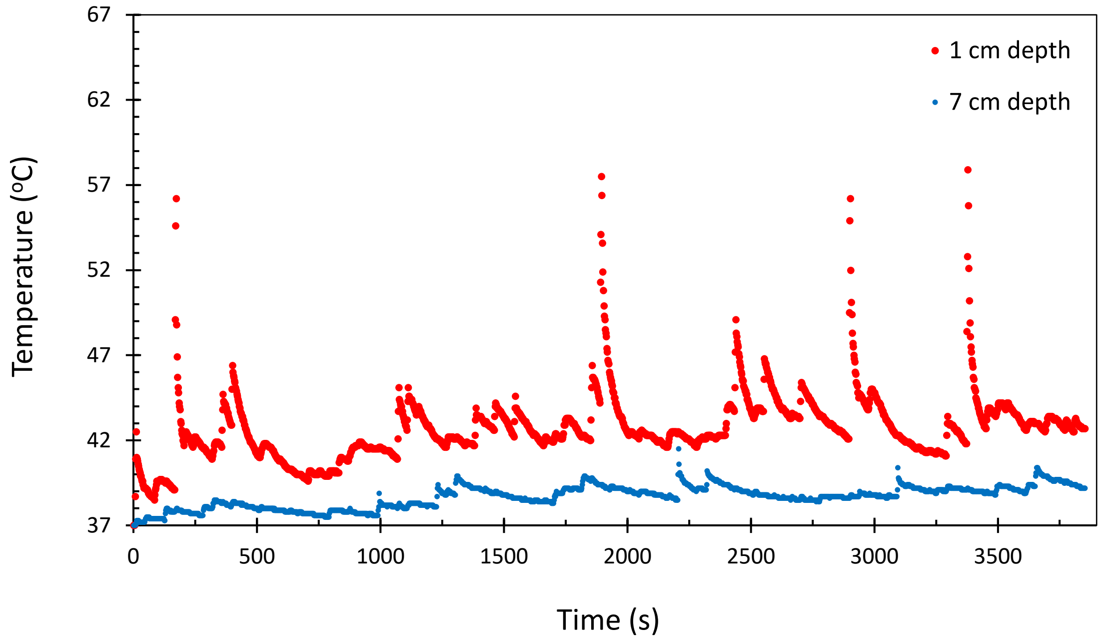

Figure 65: Temperature versus time at near-field (1 cm depth) and far-field (7 cm depth) for sonication in a 10 x 10 grid using acoustical power of 22 W, sonication time of 5 s, and delay of 30 s.

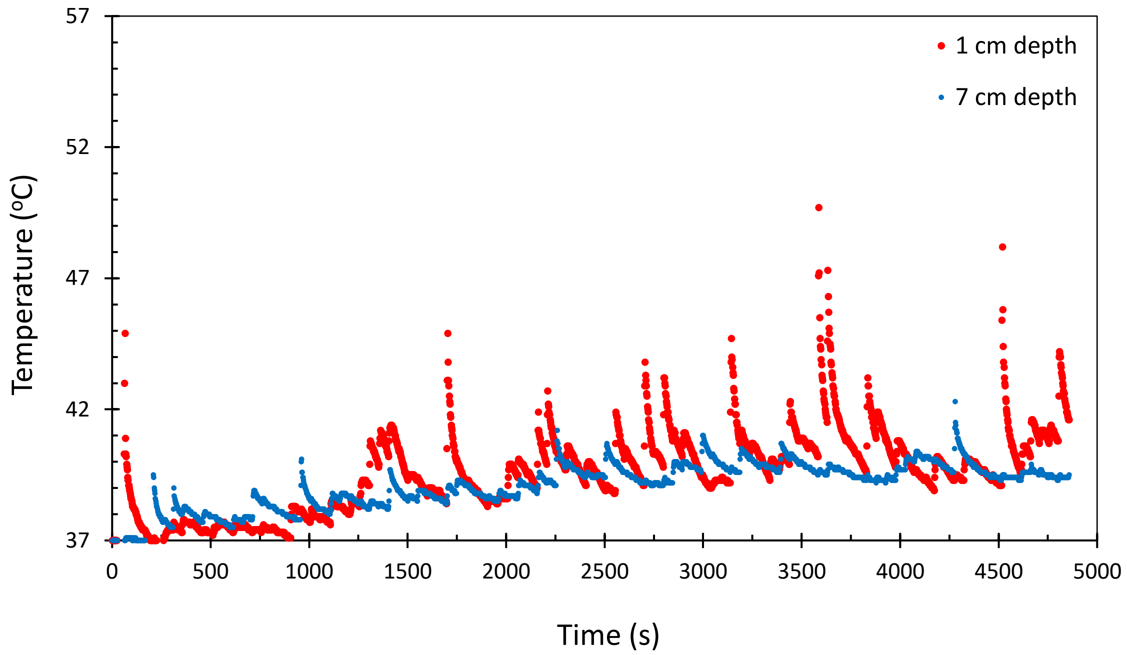

Figure 66: Temperature versus time at near-field (1 cm depth) and far-field (7 cm depth) for sonication in a 10 x 10 grid using acoustical power of 22 W, sonication time of 5 s, and delay of 40 s.

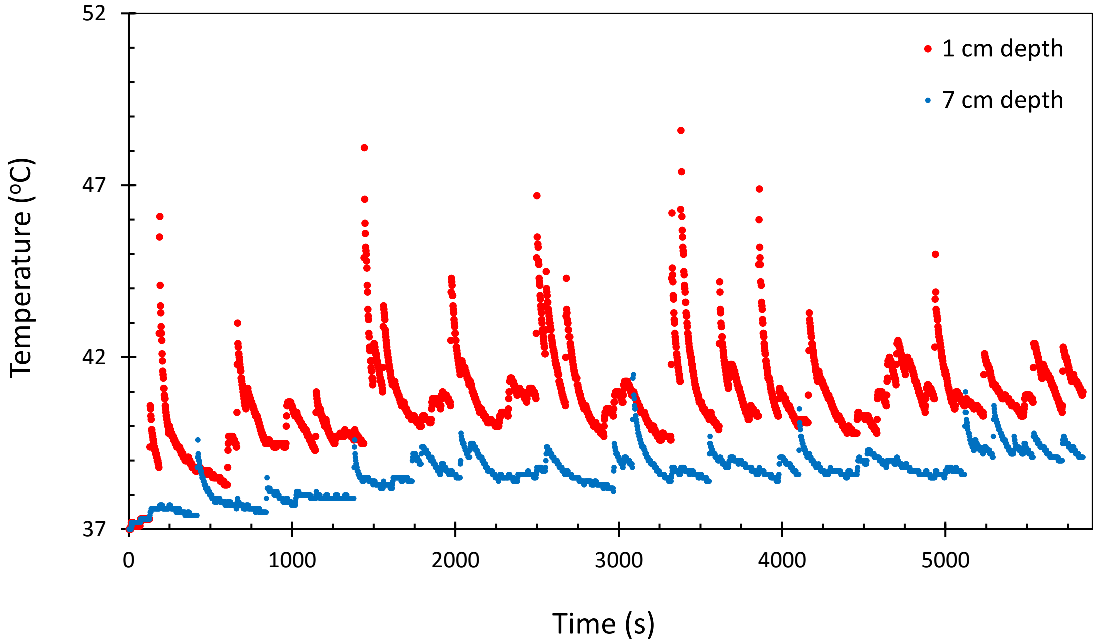

Figure 67: Temperature versus time at near-field (1 cm depth) and far-field (7 cm depth) for sonication in a 10 x 10 grid using acoustical power of 22 W, sonication time of 5 s, and delay of 50 s.

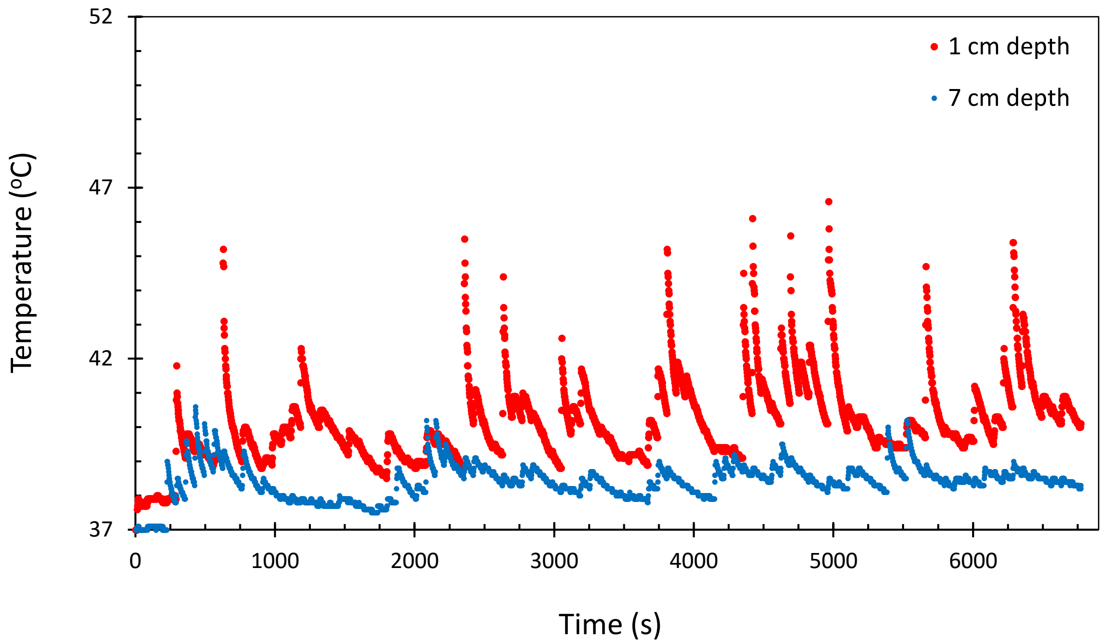

Figure 68: Temperature versus time at near-field (1 cm depth) and far-field (7 cm depth) for sonication in a 10 x 10 grid using acoustical power of 22 W, sonication time of 5 s, and time delay of 60 s.

Figure 69 shows a graph of the recorded temperature versus time in the near-field for the various delays of 0 - 60 s while Figure 70 shows the corresponding thermal dose versus delay.

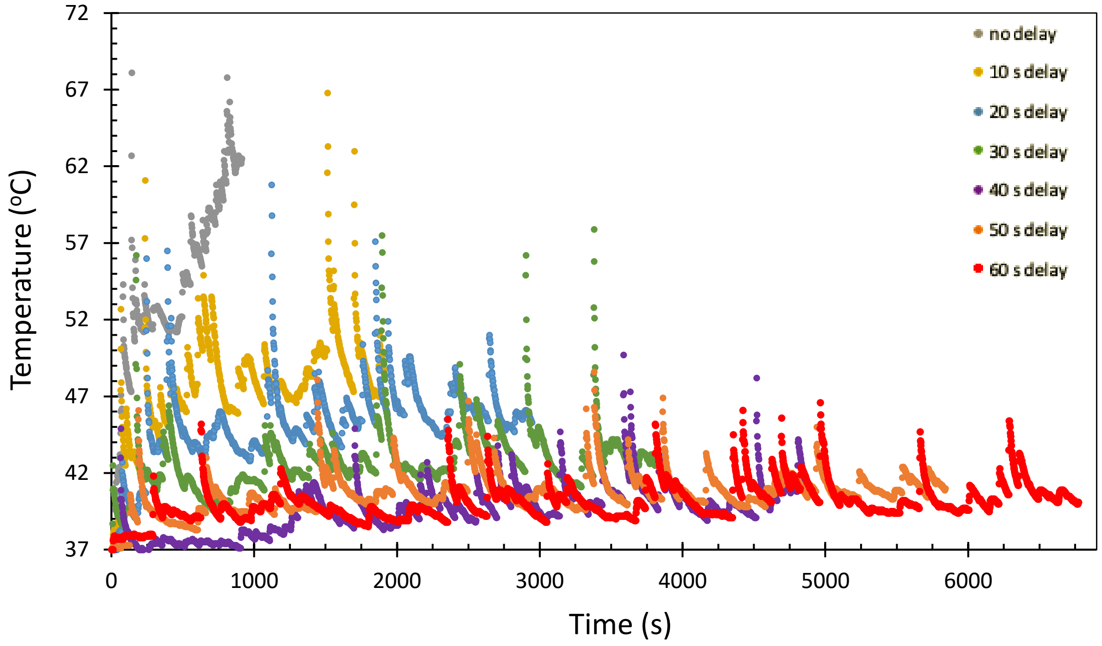

Figure 69: Temperature versus time at near-field (1 cm depth) for sonication in a 10 x 10 grid using acoustical power of 22 W, sonication time of 5 s, and varying delays (Random algorithm).

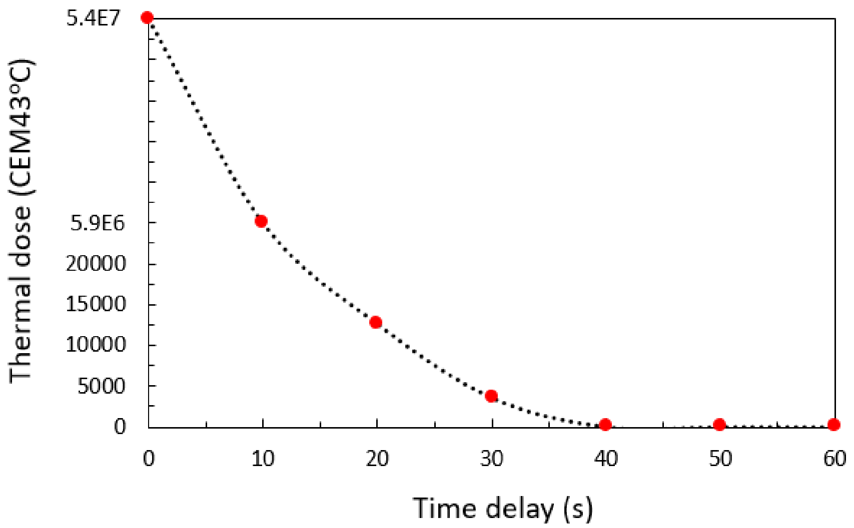

Figure 70: Thermal dose versus delay at near-field (1 cm depth) for sonication in a 10 x 10 grid using acoustical power of 22 W for sonication time of 5 s.

Table 10 summarizes both the peak and average temperature changes, as well as the accumulated thermal dose, for each delay at the near-field (Random algorithm).

Table 10: Peak and average temperature change and total dose for each delay at near-field, for sonication in a 10 x 10 grid using acoustical power of 22 W for sonication time of 5 s.

Delay (s)	Peak ΔT (ºC)	Average ΔT (ºC)	Total dose (CEM43ºC)
0	31.1	17.2	5367023.5
10	29.8	10.7	598546.4
20	23.8	8.25	12614.9
30	20.9	5.69	3589.5
40	12.7	2.58	13.77
50	11.6	3.71	22.19
60	9.6	3.11	12.56

Figure 71 shows a graph of the recorded temperature versus time in the far-field for the various delays of 0 - 60 s while Figure 72 shows the corresponding thermal dose versus delay.

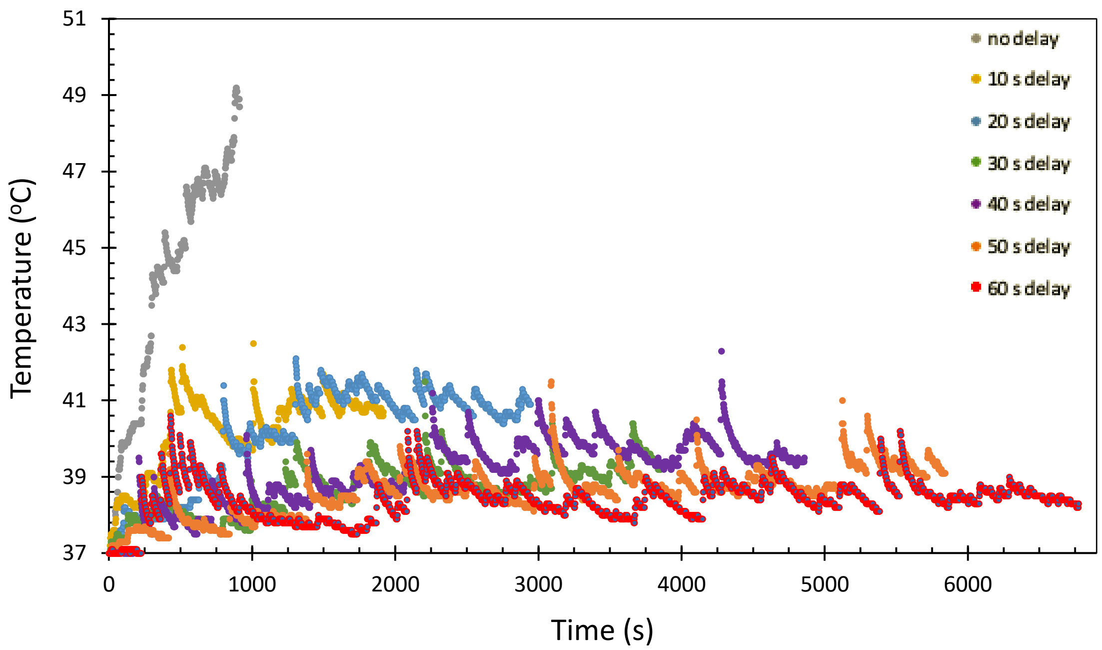

Figure 71: Temperature versus time at far-field (7 cm depth) for sonication in a 10 x 10 grid using acoustical power of 22 W, sonication time of 5 s, and varying delays (Random algorithm).

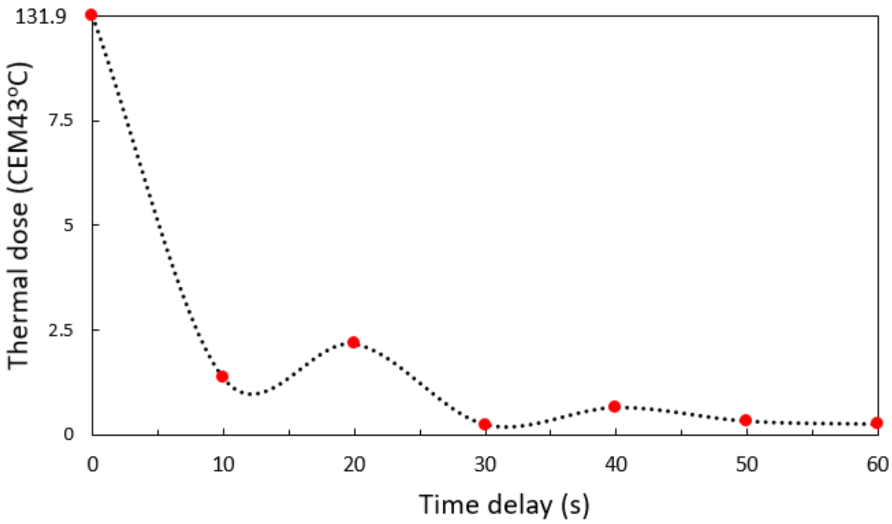

Figure 72: Thermal dose versus delay at far-field (7 cm depth) for sonication in a 10 x 10 grid using acoustical power of 22 W for sonication time of 5 s.

Table 11 summarizes both the peak and average temperature changes, as well as the total thermal dose, for each delay at the far-field (Random algorithm).

Table 11: Peak and average temperature change and total dose for each delay at far-field, for sonication in a 10 x 10 grid using acoustical power of 22 W for sonication time of 5 s.

Delay (s)	Peak ΔT (°C)	Average ΔT (°C)	Total dose (CEM43^{0}C)
0	12.2	7.07	131.9
10	6.2	3.25	1.35
20	5.1	3.08	2.17
30	4.5	1.68	0.24
40	5.3	2.09	0.65
50	4.5	1.61	0.32
60	3.6	1.40	0.25

Triangular

In this algorithm, the transducer's movement follows a “zig zag” pattern. Specifically, with each step, the transducer is moved one column to the right (in the x-axis) and either one row up or one row down in the y-axis. The sonicated grid is shown in Figure 73.

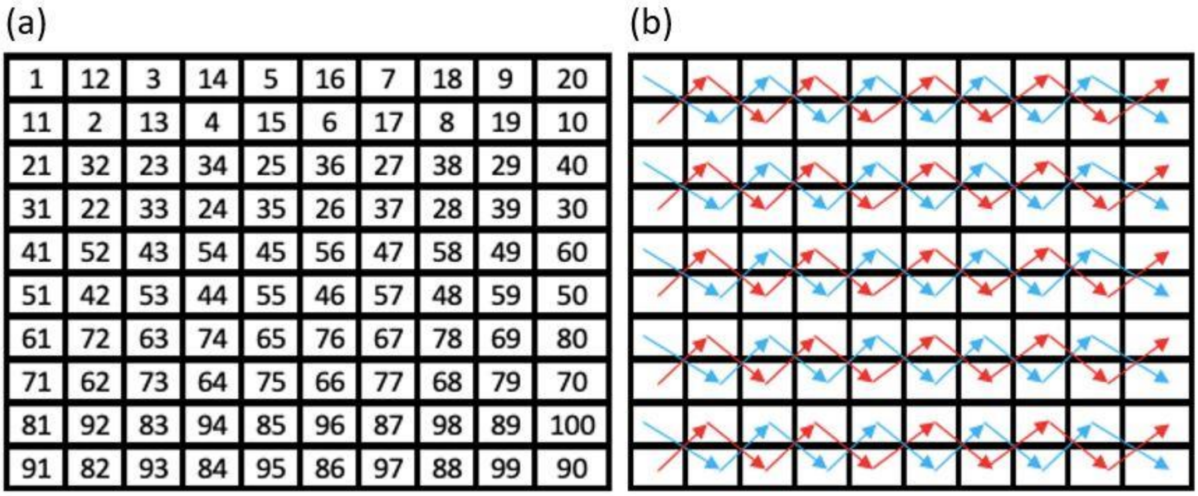

Figure 73: a) Transducer movement with triangular algorithm, and b) conceptual diagram.

Figure 74 shows a screenshot of the software acquired during execution of the triangular movement.

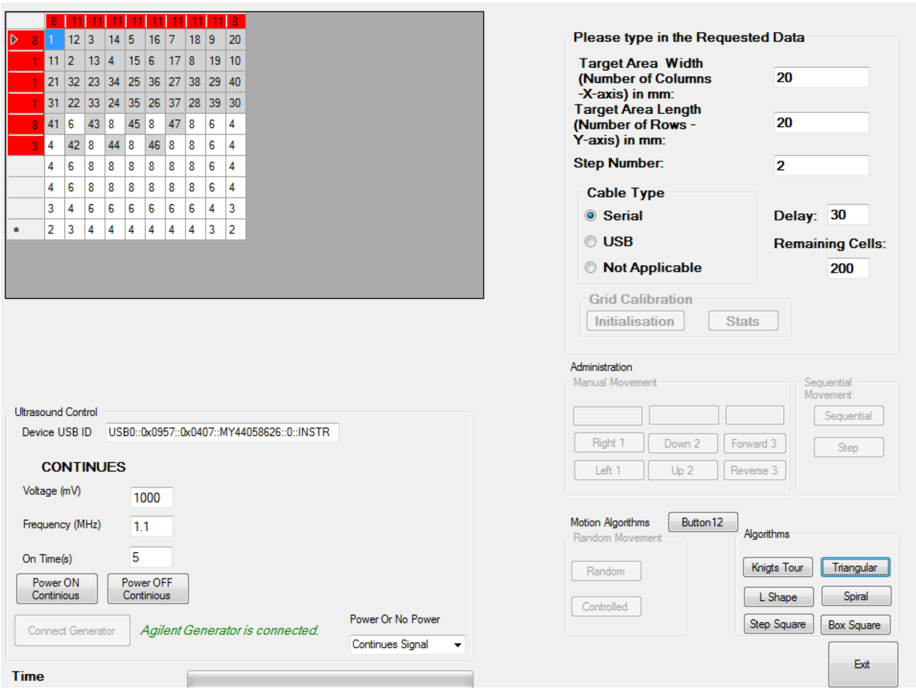

Figure 74: Software screenshot during execution of the triangular algorithm.

The recorded temperature versus time in the near and far-field for delays of 0 - 60 s (10 s step) is shown respectively in Figure 75 to Figure 81.

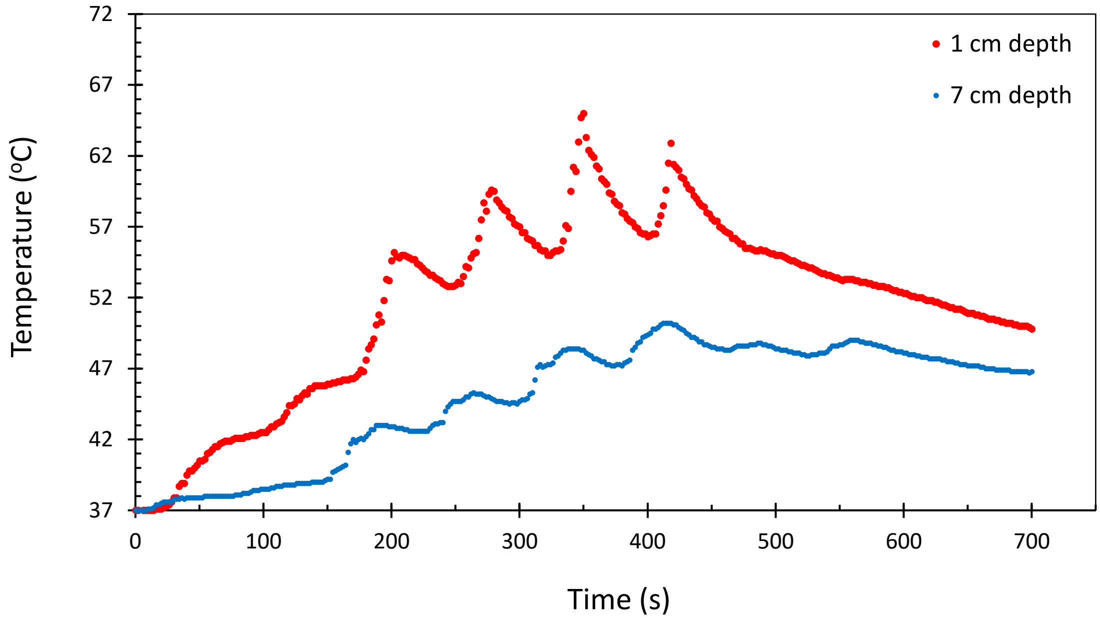

Figure 75: Temperature versus time at near-field (1 cm depth) and far-field (7 cm depth) for sonication in a 10 x 10 grid using acoustical power of 22 W, sonication time of 5 s, and delay of 0 s.

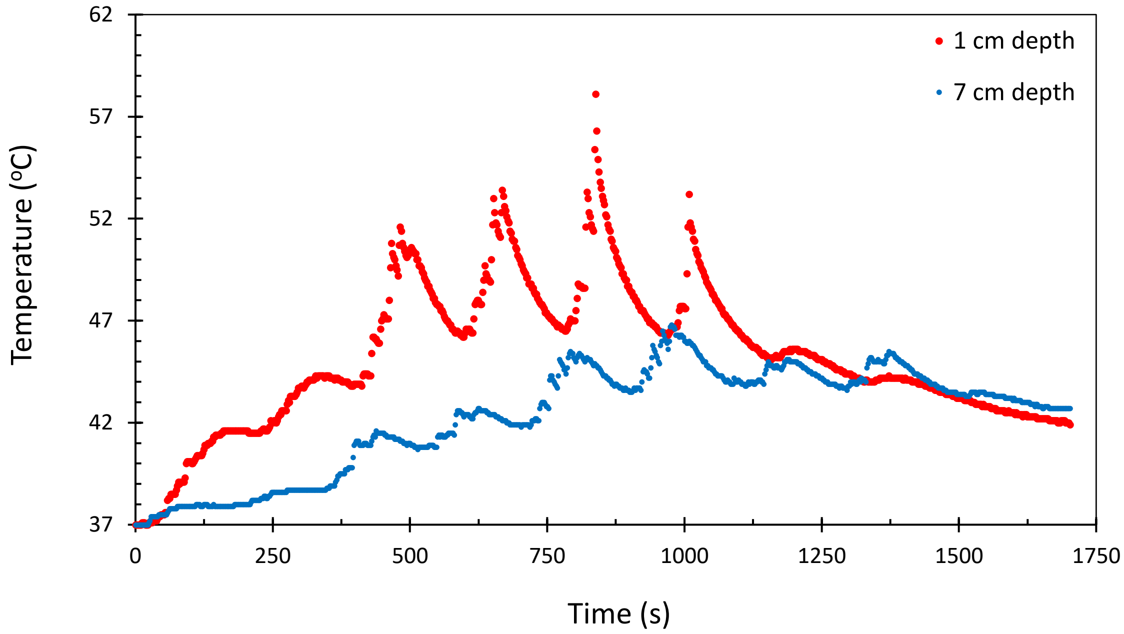

Figure 76: Temperature versus time at near-field (1 cm depth) and far-field (7 cm depth) for sonication in a 10 x 10 grid using acoustical power of 22 W, sonication time of 5 s, and delay of 10 s.

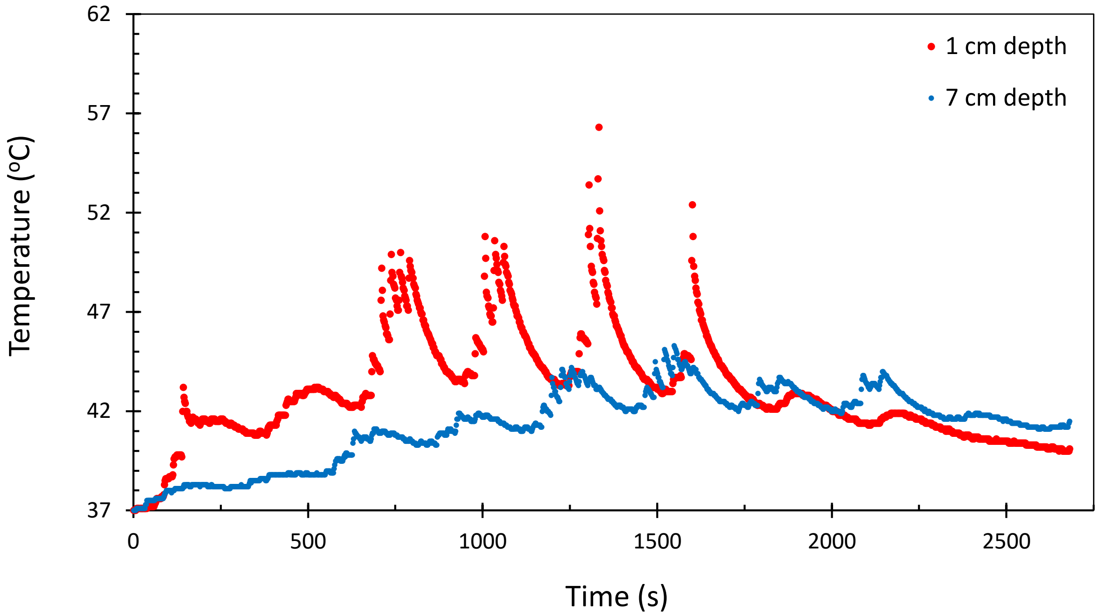

Figure 77: Temperature versus time at near-field (1 cm depth) and far-field (7 cm depth) for sonication in a 10 x 10 grid using acoustical power of 22 W, sonication time of 5 s, and delay of 20 s.

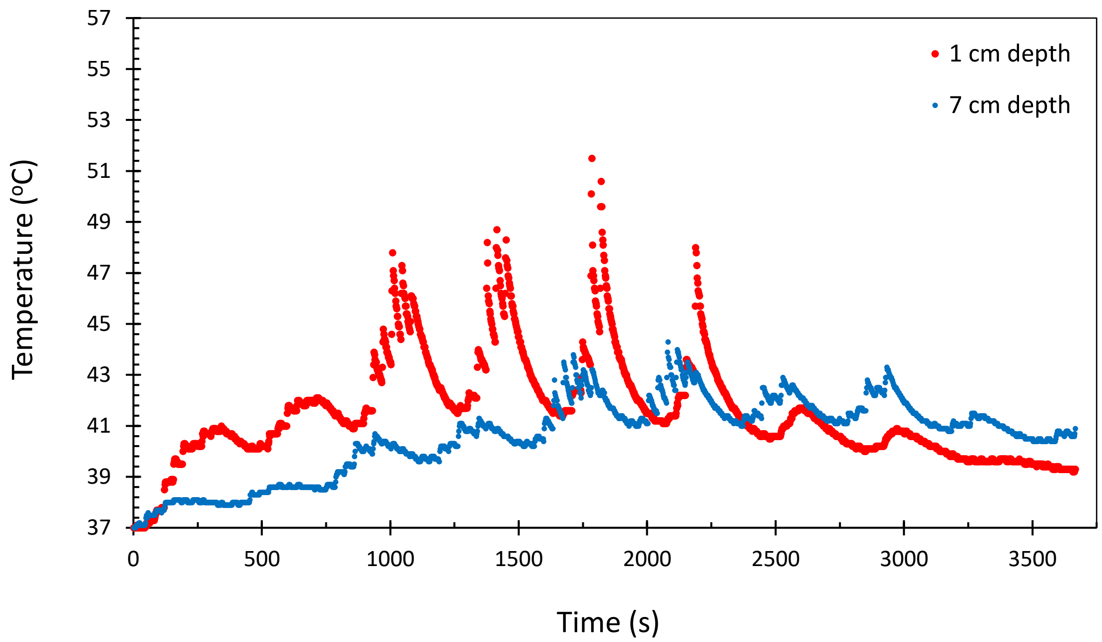

Figure 78: Temperature versus time at near-field (1 cm depth) and far-field (7 cm depth) for sonication in a 10 x 10 grid using acoustical power of 22 W, sonication time of 5 s, and delay of 30 s.

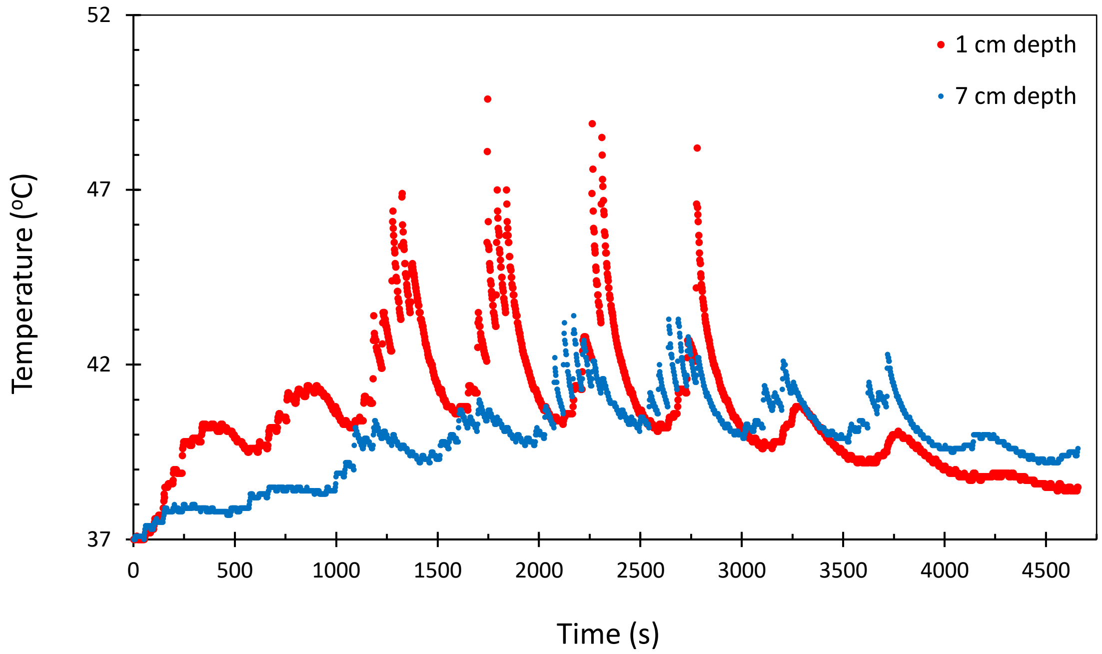

Figure 79: Temperature versus time at near-field (1 cm depth) and far-field (7 cm depth) for sonication in a 10 x 10 grid using acoustical power of 22 W, sonication time of 5 s, and delay of 40 s.

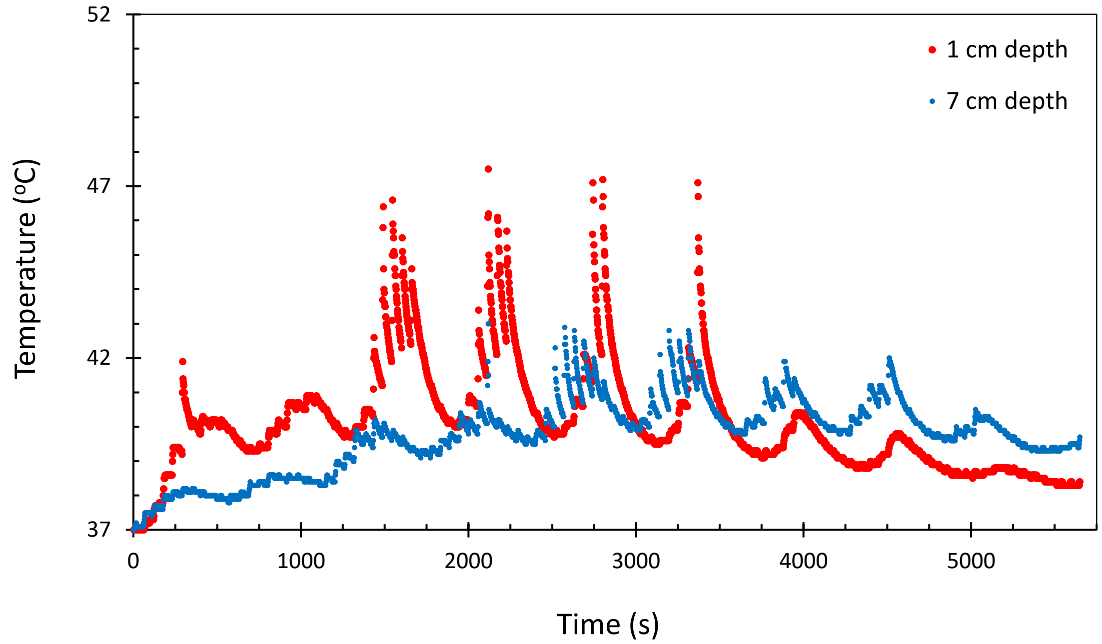

Figure 80: Temperature versus time at near-field (1 cm depth) and far-field (7 cm depth) for sonication in a 10 x 10 grid using acoustical power of 22 W, sonication time of 5 s, and delay of 50 s.

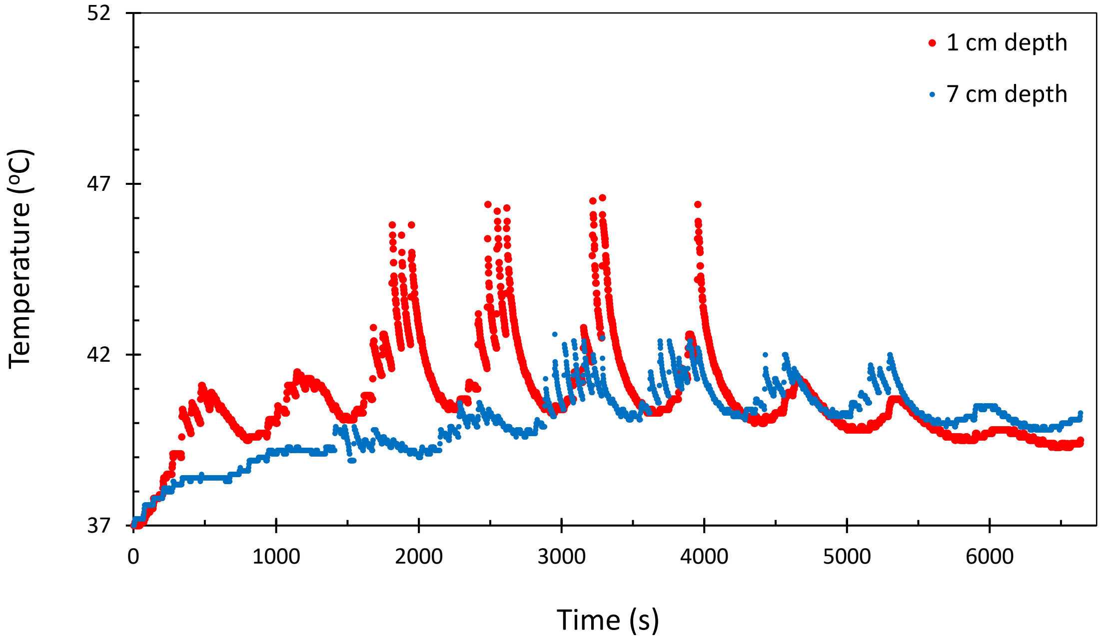

Figure 81: Temperature versus time at near-field (1 cm depth) and far-field (7 cm depth) for sonication in a 10 x 10 grid using acoustical power of 22 W, sonication time of 5 s, and time delay of 60 s.

Figure 82 shows a graph of the recorded temperature versus time in the near-field for the various delays of 0 - 60 s while Figure 83 shows the corresponding thermal dose versus delay.

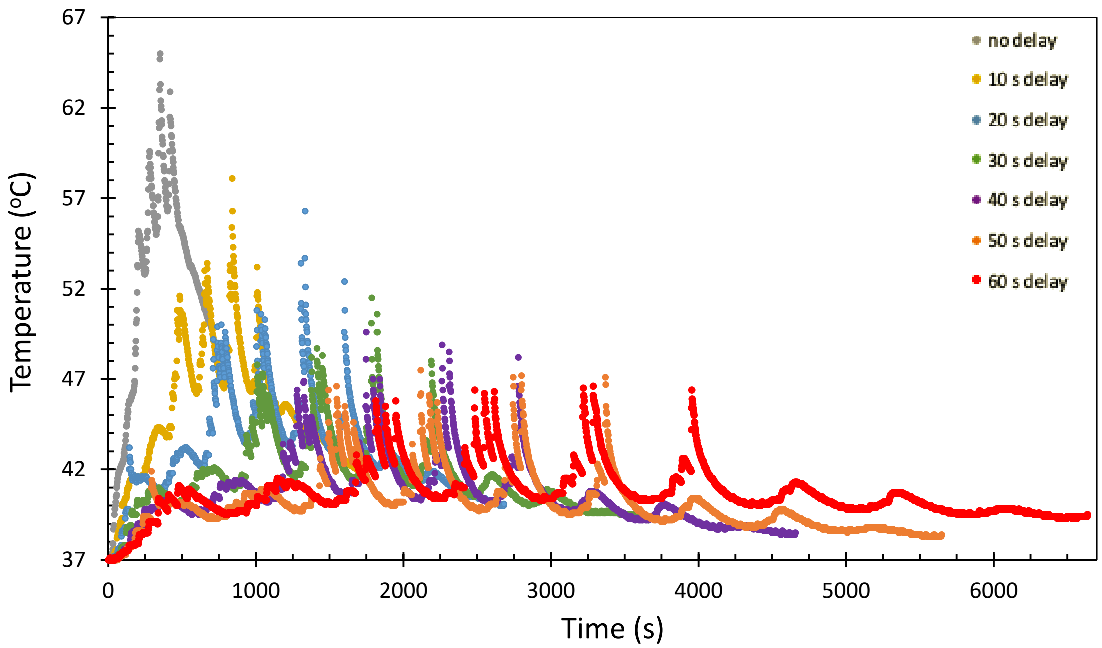

Figure 82: Temperature versus time at near-field (1 cm depth) for sonication in a 10 x 10 grid using acoustical power of 22 W, sonication time of 5 s, and varying delays (Triangular algorithm).

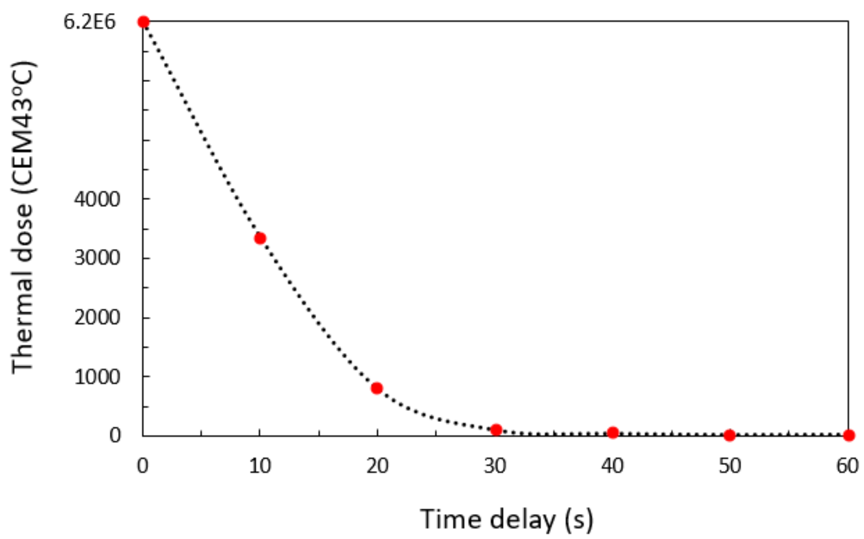

Figure 83: Thermal dose versus delay at near-field (1 cm depth) for sonication in a 10 x 10 grid using acoustical power of 22 W for sonication time of 5 s.

Table 12 summarizes both the peak and average temperature changes, as well as induced thermal dose, for each delay at the near-field (Triangular algorithm).

Table 12: Peak and average temperature change and total dose for each delay at near-field, for sonication in a 10 x 10 grid using acoustical power of 22 W for sonication time of 5 s.

Delay (s)	Peak ΔT (°C)	Average ΔT (°C)	Total dose (CEM43°C)
0	28	14.67	624658.11
10	21.1	8.21	3355.08
20	19.3	6	794.78
30	14.5	4.52	103.84
40	12.6	3.6	45.34
50	10.5	3.12	24.07
60	9.6	3.67	29.17

Figure 84 shows a graph of the recorded temperature versus time in the far-field for the various delays of 0 - 60 s while Figure 85 shows the corresponding thermal dose versus delay.

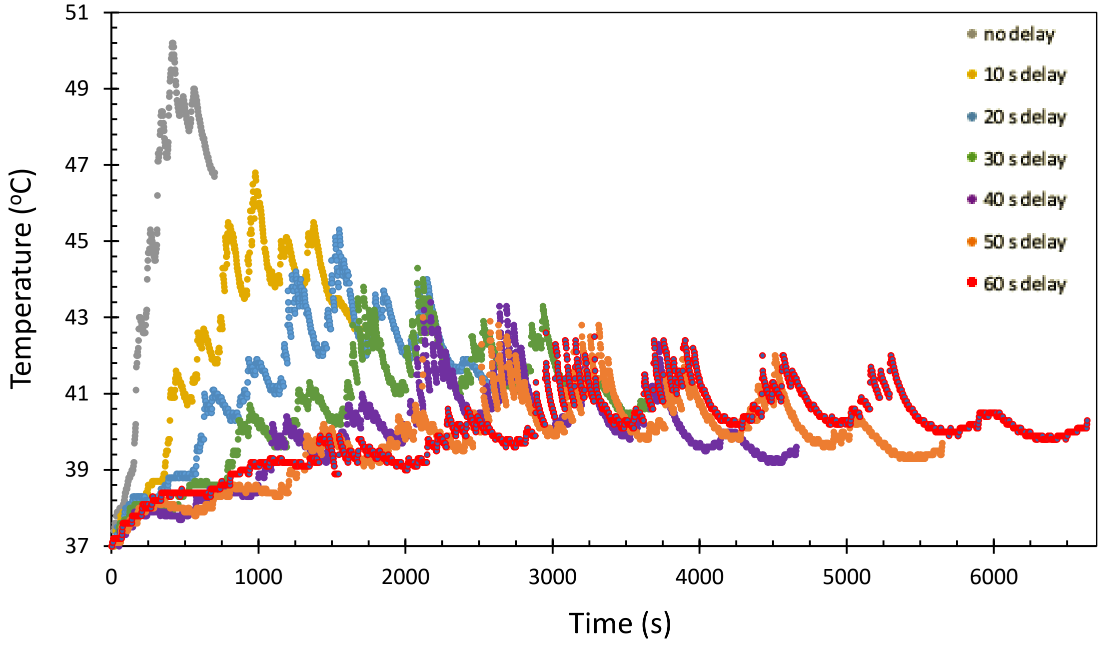

Figure 84: Temperature versus time at far-field (7 cm depth) for sonication in a 10 x 10 grid using acoustical power of 22 W, sonication time of 5 s, and varying delays (Triangular algorithm).

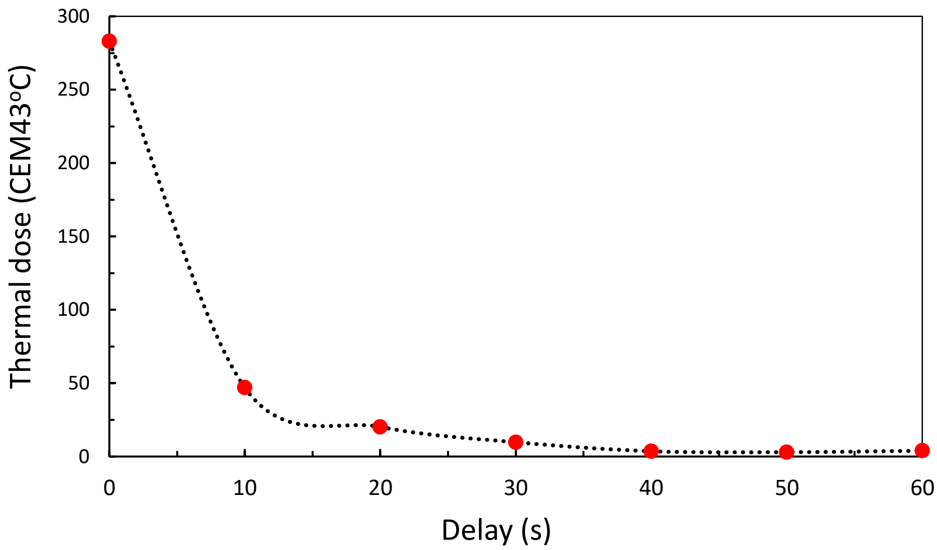

Figure 85: Thermal dose versus delay at far-field (7 cm depth) for sonication in a 10 x 10 grid using acoustical power of 22 W for sonication time of 5 s.

Table 13 summarizes both the peak and average temperature changes, as well as the total thermal dose, for each delay at the far-field (Triangular algorithm).

Table 13: Peak and average temperature change and total dose for each delay at far-field, for sonication in a 10 x 10 grid using acoustical power of 22 W for sonication time of 5 s.

Delay (s)	Peak ΔT (ºC)	Average ΔT (ºC)	Total dose ($CEM43^0C$)
0	13.2	7.88	282.97
10	9.8	5.29	46.98
20	8.3	4.29	20.25
30	7.3	3.59	9.75
40	6.4	2.84	3.63
50	6	2.75	2.98
60	5.6	2.98	3.96

Temperature changes and thermal dose

The peak temperature change for each delay and algorithm in the near-field and far-field is listed in Table 14 and Table 15, respectively.

Table 14: Peak temperature change in the near-field for sonication in a 10 x 10 grid using acoustical power of 22 W for sonication time of 5 s, using different motion algorithms and varying delays.

Algorithm	Sequential	Euler's	Spiral	Square	Random	Triangular
Delay (s)	**Peak ΔT (ºC)**					
0	64.8	32.4	34.4	32.4	31.1	28
10	32.9	25.1	25.4	29.9	29.8	21.1
20	26	15.6	20.6	19.7	23.8	19.3
30	16.5	10.2	16.6	16.3	20.9	14.5
40	14.5	9.2	15.8	14.7	12.7	12.6
50	13.2	6.3	11.8	14.5	11.6	10.5
60	13.2	7.4	9.1	14.2	9.6	9.6

Table 15: Peak temperature change in the far-field for sonication in a 10 x 10 grid using acoustical power of 22 W for sonication time of 5 s, using different motion algorithms and varying delays.

Algorithm	Sequential	Euler's	Spiral	Square	Random	Triangular
Delay (s)	**Peak ΔT (ºC)**					
0	25.5	15.8	9.5	8.6	12.2	13.2
10	20.4	12.9	7.1	8.3	6.2	9.8
20	17.3	15.7	7.1	6.6	5.1	8.3
30	10.9	9.5	6	5.7	4.5	7.3
40	11.9	8.8	4.5	3.7	5.3	6.4
50	14.8	9.1	4.7	4	4.5	6
60	6.4	5.5	5.1	4.2	3.6	5.6

Accordingly, the average temperature change for each different algorithm and delay in the near-field and far-field is listed in Table 16 and Table 17, respectively. Note that when the temperature is smaller than 4 ºC a green font is used.

Table 16: Average temperature change in the near-field for sonication in a 10 x 10 grid using acoustical power of 22 W for sonication time of 5 s, using different motion algorithms and varying delays.

Algorithm	Sequential	Euler's	Spiral	Square	Random	Triangular
Delay (s)	**Average ΔT (ºC)**					
0	38.5	23.18	18.6	19.43	17.2	14.67
10	17.49	16.89	9.95	10.82	10.7	8.21
20	13.77	10.58	6.9	8.23	8.25	6
30	7.2	6.95	5.7	5.46	5.69	4.52
40	5.58	6.1	4.01	3.57	2.58	3.6
50	5	3.86	3.64	3.51	3.71	3.12
60	1.94	4.22	3.51	3.22	3.11	3.67

Table 17: Average temperature change in the far-field for sonication in a 10 x 10 grid using acoustical power of 22 W for sonication time of 5 s, using different motion algorithms and varying delays.

Algorithm	Sequential	Euler's	Spiral	Square	Random	Triangular
Delay (s)	Average ΔT (ºC)					
0	12.6	9.08	5.89	5.10	7.07	7.88
10	7.97	7.16	3.88	4.40	3.25	5.29
20	5.77	3.21	3.62	3.68	3.08	4.29
30	5.89	1.79	2.93	2.64	1.68	3.59
40	5.86	1.76	1.68	1.34	2.09	2.84
50	2.79	1.02	1.91	1.13	1.61	2.75
60	1.99	1.7	2.06	1.74	1.40	2.98

Table 18 and Table 19 summarize the thermal dose accumulated in the near-field and far-field, respectively, for each tested algorithm and time delay. A thermal dose of 30 CEM was assumed to be safe without damaging the areas in the near and far-field of the transducer.

Table 18: Thermal dose in the near-field for sonication in a 10 x 10 grid using acoustical power of 22 W for sonication time of 5 s, using different motion algorithms and varying delays.

Algorithm	Sequential	Euler's	Spiral	Square	Random	Triangular
Delay (s)	Total dose (CEM43^{0}C)					
0	1.70757E+17	115629236.4	28933635.2	22420020.6	5367023.5	624658.11
10	56964725.96	944287.2	133808.7	622325.1	598546.4	3355.08
20	977060.1	3049	1845.2	4282.8	12614.9	794.78
30	1607.4	186.7	306	372.8	3589.5	103.84
40	365.7	127.98	98.4	96.24	13.77	45.34
50	236.3	11.2	37.9	104.62	22.19	24.07
60	17.6	24.1	22.4	40.17	12.56	29.17

Table 19: Thermal dose in the far-field for sonication in a 10 x 10 grid using acoustical power of 22 W for sonication time of 5 s, using different motion algorithms and varying delays.

Algorithm	Sequential	Euler's	Spiral	Square	Random	Triangular
Delay (s)	**Total dose (CEM43⁰C)**					
0	77977.3	719.05	32.69	17.82	131.9	282.97
10	2630.4	253	5.37	14	1.35	46.98
20	293.4	56.8	4.64	5.42	2.17	20.25
30	124.4	1.54	1.69	1.1	0.24	9.75
40	121.4	1.14	0.28	0.164	0.65	3.63
50	41.3	0.53	0.49	0.142	0.32	2.98
60	1.4	0.54	1.08	0.472	0.25	3.96

Figure 86 and Figure 87 show the thermal dose accumulated in the near-field with respect to the delay for all six algorithms.

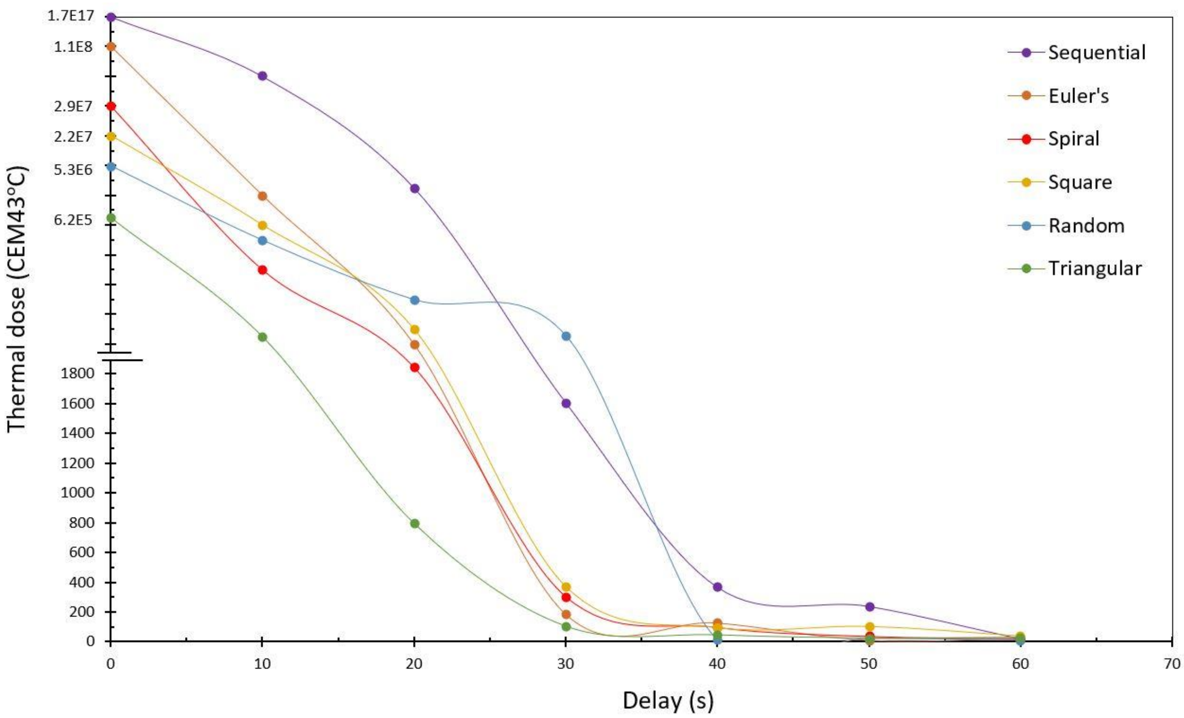

Figure 86: Thermal dose versus delay at near-field for all six algorithms.

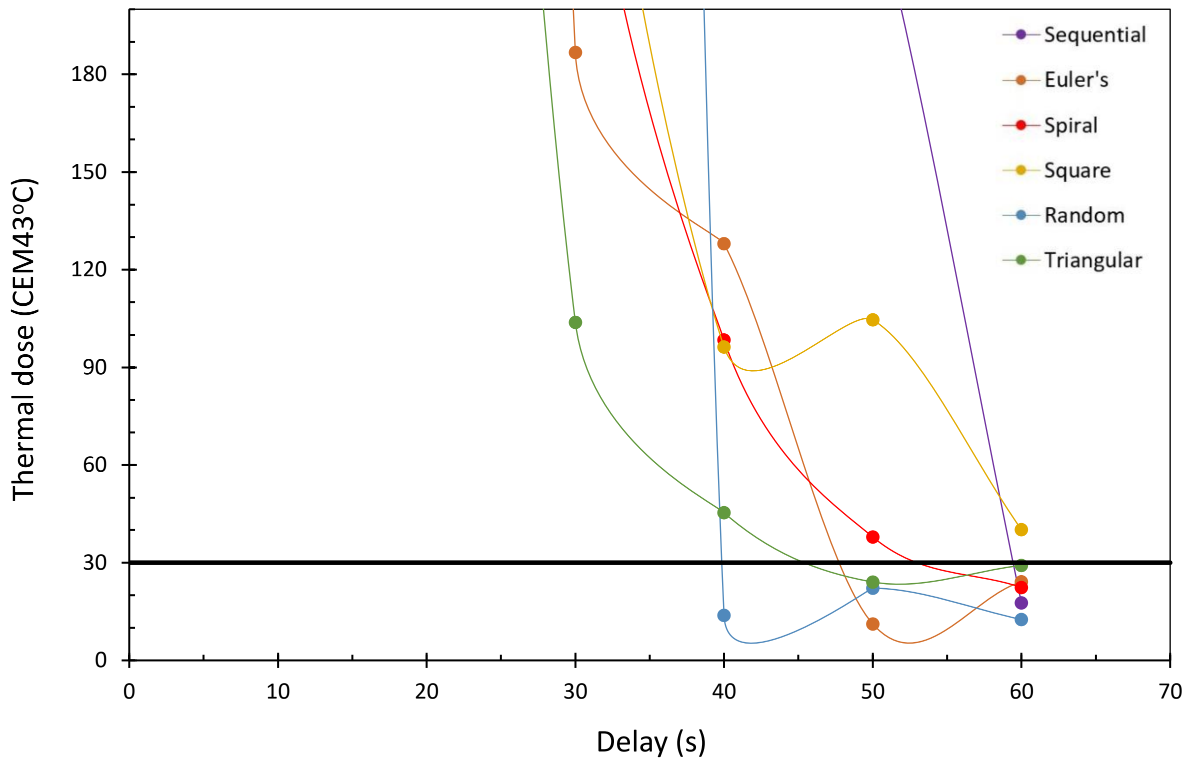

Figure 87: Thermal dose versus delay at near-field for all six algorithms. The black line indicates the thermal dose threshold of 30 CEM.

Figure 88 and Figure 89 show the thermal dose accumulated in the far-field with respect to the delay for all six algorithms.

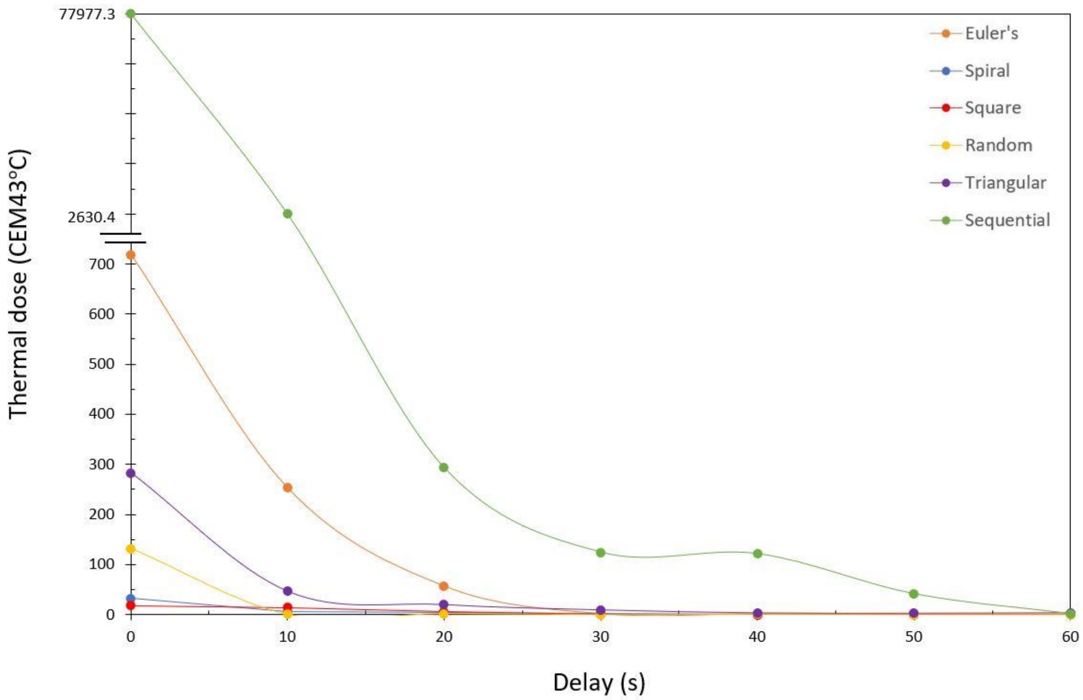

Figure 88: Thermal dose versus delay at far-field for all six algorithms.

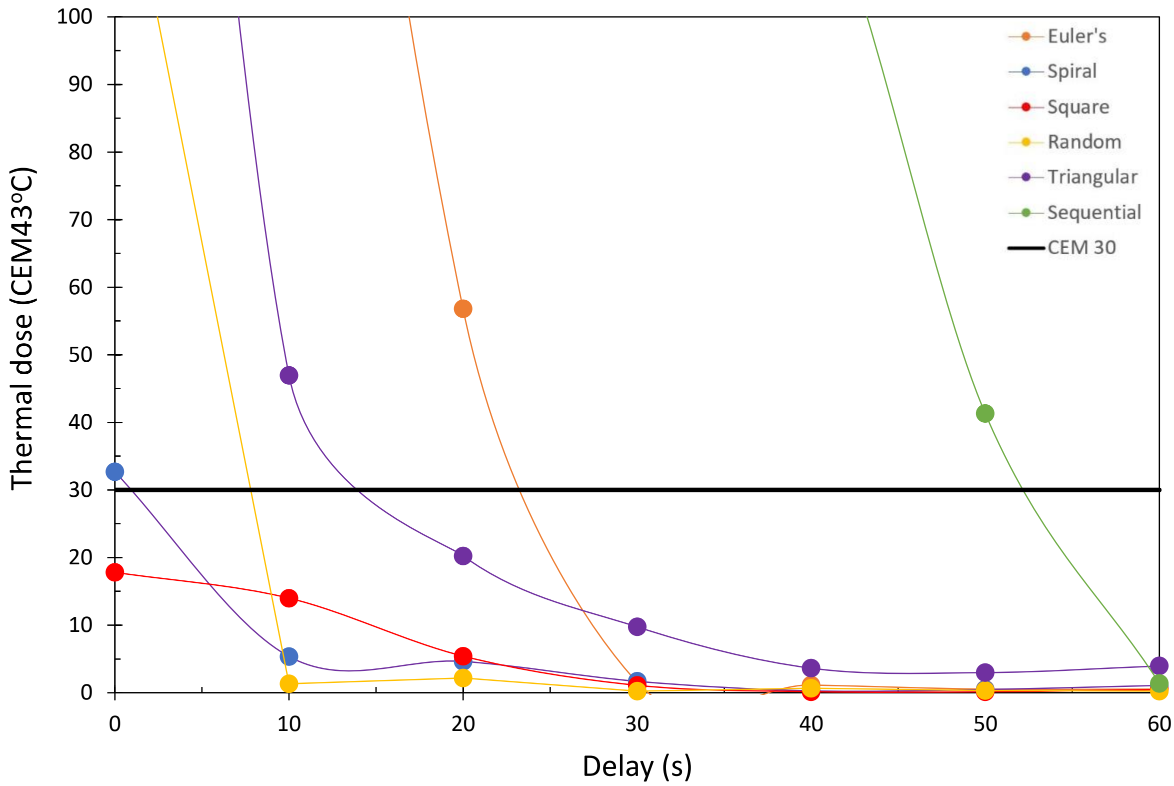

Figure 89: Thermal dose versus delay at far-field for all six algorithms. The black line indicates the thermal dose threshold of 30 CEM.

Discussion

The purpose of this study was to experimentally evaluate the induced near-field and far-field heating of a single-element (curved) focused transducer of low frequency (1.1 MHz). The measurement of dose accumulation at these two regions is important for HIFU applications, and particularly for safe and efficient ablation of the entire tissue volume in the clinical practice.

The reason for selecting the proposed transducer frequency was the vast use of low-frequency transducers for several HIFU treatments such as the treatment of uterine fibroids [19,27] and breast cancer [28]. However, ultrasonic beams of low frequency are typically wide. Therefore, the use of low frequency transducers is considered the worst scenario for evaluating overheating at the near and far-field regions. Unfortunately, researchers have solely concentrated on the estimation of the accumulated temperature in the near and far field regions through simulation models. Although simulations are able to project the heating and thermal dose, they might lead to inaccurate estimations or overestimations due to possible errors. On the other hand, experimental estimations, such as those performed in this study, are much closer to the clinical reality of accurate measurement of thermal dose.

The elimination of the near and far-field heating was achieved by varying two main factors: the delay between the grid points (to which a sonication of total ultrasonic energy of 110 J was applied) and the motion algorithm (movement pattern) followed. The ultrasonic energy was adequate in reaching a high accumulated thermal dose at the focal point (5 cm depth). Herein, both factors were investigated through the use of a delay range of 0 - 60 s and six different algorithms. The evaluation of these factors was implemented on a homogeneous agar/wood powder phantom with ultrasonic parameters close to that of soft tissue. It should be clarified that our investigation was limited to only homogeneous samples and any sample condition involving multiple layers of different ultrasonic parameters or obstacles (in case of bone or ribs) has not been evaluated.

It was observed, as expected, that as the delay increased the accumulated thermal dose in both the near-field and far-field decreased drastically for all algorithms. The temperature changes in the near-field were higher than those in the far-field where the ultrasound beam propagated a longer distance (6 cm more) in the phantom and was weakened considerably due to the attenuation factor. However, the differences in temperature at the far-field among the six algorithms for varying delays were still obvious. The criterion for safe dose was selected as 30 CEM at 43 ^{o}C. According to the thermal dose estimation for each algorithm in the near-field, sequential algorithm produced severe thermal dose when using a 20 s or shorter delay. The thermal doses using the sequential algorithm for 0-20 s delays were the highest in the near-field amongst all algorithms used in this study. The sequential algorithm still induced a thermal dose close to 240 CEM at 43 ^{o}C (which is a threshold of tissue damage) by using a 50 s delay, and therefore, it requires at least 60 s delay to eliminate pre-focal heating. Therefore, for this motion algorithm, it is recommended to use at least 60 s delay between sonications to ablate the entire tumor without damaging areas at the near-field.

Initially, we expected that the spiral and square algorithms would require much less delay than the sequential algorithm to eliminate pre-focal heating due to their large spatial steps. However, the experiments have refuted this expectation since it was observed that both algorithms induced more than 240 CEM at 43 ^{o}C for a delay of 30 s or shorter. The pre-focal heating was eliminated at 60 s delay for the spiral algorithm while more than 60 s delay was needed for the square algorithm. The Euler's and triangular algorithms reduced the pre-focal heating by requiring at least a 50 s delay. However, both algorithms, which use larger spatial steps than sequential, produced a thermal dose of 240 CEM at 43 ^{o}C when a 30 s or shorter cooling was applied during the evaluation procedure. Finally, the thermal dose using the random algorithm significantly decreased with increase in the time delay from 30 s (thermal dose of tissue-damaging) to 40 s. The random algorithm that follows random transducer navigation was the sole algorithm that required a delay of 40 s to minimize near-field heating. Nevertheless, this algorithm has unpredictable motion paths that might overstress motors.

Our experimental technique determined that the sequential algorithm induced severe heating not only in the pre-focal region but beyond the focus (far-field) as well. The far-field heating using the sequential algorithm was below 30 CEM at 43 ^{o}C only with a 60 s delay. It is thus concluded that the clinical use of the sequential algorithm as a treatment pattern can thermally harm tissue at the far-field when time delays shorter than 60 s are applied. All the other algorithms needed a time delay shorter than 30 s to eliminate the far-field heating, with the square algorithm eliminating thermal heating at no delay, spiral and random with a 10 s delay, triangular with a 20 s delay, and finally Euler's algorithm with a 30 s delay.

Previously published works have recommended possible treatment paths without considering the increase in treatment time [6], [29], [16]. A fixed 60 s delay for sequential treatment strategy was used to investigate different planar paths [6] and heuristic paths with the greatest possible distance between sequential small rapid scanning volumes [29]. Moreover, Payne et al. [16] allowed 60 s cooling time for the sequential algorithm, but the spacing between the grid points was set at 1 cm, which was considered relatively large and led to underrated results. The experimental results of our study confirmed that the sequential algorithm requires at least 60 s delay to eliminate both the near and far-field heating when ablating a 20 x 20 mm^2 area. Notably, in a study by Payne et al [30], the treatment time was calculated for three suggested path scans using a 1 MHz phased array transducer. The cooling times were selected to retain the cumulative near-field heating beneath 5 CEM at 43 ^{o}C for the whole treatment. However, the results of this study were only extracted through simulations compared to our study, which is an experimental estimation of the required delay for the near and far-field heating elimination.

Other studies reported delays for HIFU treatment of large regions. McDannold et al. [7] recommended at least 50-60 s of cooling time between sonications, whereas Fennessy and Tempany [31] used 80-90 s. In all these studies, the sequential algorithm was exclusively used for covering the entire treatment area. An appropriate delay was allowed between the grid points but without investigating possible reduction of the delay or use of another treatment path so as to achieve a faster total treatment ablation. Overall, the time delays suggested in the above studies are similar to what is proposed in the current study.

The results presented in this study corroborate the requirement of sequential plan treatment using a 60 s delay. Large treatment time reductions can be realized by judicious motion algorithm selection for the homogeneous tissue-mimicking material that was used in these experiments. The present findings might help to solve issues that appear with prolonged HIFU treatment therapies. The accumulation of high thermal dose in the near and far-field regions causes pain to some patients, which may result in treatment interruptions and longer treatment times. The sequential, square, and spiral algorithms require a long cooling time while Euler's and triangular algorithms need a shorter delay by 10 s. The random algorithm eliminates pre-focal heating with a 40 s delay between all sonications needed to cover a large tumor area. In summary, the results provide useful recommendations for yielding significant treatment time savings through the selection of the optimized algorithm and delay for HIFU applications in homogeneous tissues.

Another factor that contributes to the total treatment time is the movement of the robotic device. The time taken for robot movement was calculated for all six algorithms to examine its effect on total treatment time. Table 20 shows the total treatment time that is needed for each algorithm for complete elimination of the near and far-field heating. Assuming a 60 s delay and a 5 s sonication time for a 10 x 10 grid (100 movements), the treatment time is 110 minutes for the sequential algorithm, 94.9 minutes for the Euler's algorithm, 113.2 minutes for the spiral algorithm, at least 116.1 minutes for the square algorithm, 80.9 - 81.9 minutes for the random algorithm, and 94.4 minutes for the triangular algorithm. For complete elimination of the near-field heating, a 40 s delay is needed for the random algorithm, which results in the minimum total treatment time of 80.9 minutes.

Table 20: Total time needed for treatment using each algorithm for complete reduction of the near-field and far-field heating.

Algorithm	Robot time (s)	Delay for elimination of near and far-field heating (s)	Sonication time (s)	Scanning time (s)	Total time (s) = Robot time + Scanning time + Sonication time	Total time (min)
Sequential	102	60	500	6000	6602	110
Euler's	195	50	500	5000	5695	94.9
Spiral	297	60	500	6000	6797	113.2
Square	466	> 60	500	> 6000	> 6966	> 116.1
Random	359-411	40	500	4000	4859-4911	80.9-81.9
Triangular	162	50	500	5000	5662	94.4

References

[1] C. Yiallouras, N. Mylonas, and C. Damianou, “MRI-compatible positioning device for guiding a focused ultrasound system for transrectal treatment of prostate cancer,” *Int. J. Comput. Assist. Radiol. Surg.*, vol. 9, no. 4, pp. 745–753, 2014, doi: 10.1007/s11548-013-0964-x.

[2] K. Hynynen *et al.*, “MR imaging-guided focused ultrasound surgery of fibroadenomas in the breast: a feasibility study,” *Radiology*, vol. 219, no. 176–185, 2001.

[3] R. Salomir *et al.*, “Local hyperthermia with MR-guided focused ultrasound: Spiral trajectory of the focal point optimized for temperature uniformity in the target region,” *J. Magn. Reson. Imaging*, vol. 12, no. 4, pp. 571–583, 2000, doi: 10.1002/1522-2586(200010)12:4<571::AID-JMRI9>3.0.CO;2-2.

[4] C. Damianou and K. Hynynen, “Focal spacing and near-field heating during pulsed high temperature ultrasound therapy,” *Ultrasound Med. Biol.*, vol. 19, no. 9, pp. 777–787, 1993, doi: 10.1016/0301-5629(93)90094-5.

[5] C. Mougenot, M. O. Köhler, J. Enholm, B. Quesson, and C. Moonen, “Quantification of near-field heating during volumetric MR-HIFU ablation,” *Med. Phys.*, vol. 38, no. 1, pp. 272–282, 2011, doi: 10.1118/1.3518083.

[6] X. Fan and K. Hynynen, “Ultrasound surgery using multiple sonications - Treatment time considerations,” *Ultrasound Med. Biol.*, vol. 22, no. 4, pp. 471–482, 1996, doi: 10.1016/0301-5629(96)00026-9.

[7] N. McDannold, F. Jolesz, and K. Hynynen, “Determination of the Optimal Delay between Sonications during Focused Ultrasound Surgery in Rabbits by Using MR Imaging to Monitor Thermal Buildup in Vivo,” *Radiology*, vol. 211, no. 2, pp. 419–426, 1999.

[8] P. Ramaekers, M. de Greef, J. van Breugel, C. Moonen, and M. Ries, “Increasing the HIFU ablation rate through an MRI-guided sonication strategy using shock waves: feasibility in the in vivo porcine liver,” *Phys. Med. Biol.*, vol. 61, no. 3, p. 1057, 2016.

[9] P. Baron *et al.*, “In vivo T2-based MR thermometry in adipose tissue layers for high-intensity focused ultrasound near-field monitoring,” *Magn. Reson. Med.*, vol. 72, no. 4, pp. 1057–1064, 2014, doi: 10.1002/mrm.25025.

[10] C. Mougenot *et al.*, “MR Monitoring of the Near-Field HIFU Heating,” in *AIP*

Conference Proceedings, 2009, p. 1113(159).

[11] X. Ji, D. Li, G. Shen, J. Bai, and Y. Chen, “A method of introducing cooling time between multiple sonications in focused ultrasound surgery,” *Int. J. Heat Mass Transf.*, vol. 56, no. 1–2, pp. 403–410, 2013, doi: 10.1016/j.ijheatmasstransfer.2012.09.036.

[12] E. Ozhinsky, V. A. Salgaonkar, C. J. Diederich, and V. Rieke, “MR thermometry-guided ultrasound hyperthermia of user-defined regions using the ExAblate prostate ablation array,” *J. Ther. Ultrasound*, vol. 6, no. 1, pp. 1–10, 2018, doi: 10.1186/s40349-018-0115-5.

[13] J. Wijlemans, M. de Greef, G. Schubert, M. A. van den Bosch, C. Moonen, and M. Ries, “Near-field management during MR-HIFU ablation in highly perfused organs,” in *Proc. Int. Soc. Mag. Reson. Med.*, 2014, p. 22.

[14] L. C. Phillips, C. Puett, P. S. Sheeran, P. A. Dayton, G. Wilson Miller, and T. O. Matsunaga, “Phase-shift perfluorocarbon agents enhance high intensity focused ultrasound thermal delivery with reduced near-field heating,” *J. Acoust. Soc. Am.*, vol. 134, no. 2, pp. 1473–1482, 2013, doi: 10.1121/1.4812866.

[15] M. O. Köhler *et al.*, “Volumetric HIFU ablation under 3D guidance of rapid MRI thermometry,” *Med. Phys.*, vol. 36, no. 8, pp. 3521–3535, 2009, doi: 10.1118/1.3152112.

[16] A. Payne, U. Vyas, N. Todd, J. De Bever, D. A. Christensen, and D. L. Parker, “The effect of electronically steering a phased array ultrasound transducer on near-field tissue heating,” *Med. Phys.*, vol. 38, no. 9, pp. 4971–4981, 2011, doi: 10.1118/1.3618729.

[17] J. K. Enholm, M. O. Köhler, B. Quesson, C. Mougenot, C. T. W. Moonen, and S. D. Sokka, “Improved volumetric MR-HIFU ablation by robust binary feedback control,” *IEEE Trans. Biomed. Eng.*, vol. 57, no. 1, pp. 103–113, 2010, doi: 10.1109/TBME.2009.2034636.

[18] M. Tillander *et al.*, “High intensity focused ultrasound induced in vivo large volume hyperthermia under 3D MRI temperature control,” *Med. Phys.*, vol. 43, no. 3, pp. 1539–1549, 2016, doi: 10.1118/1.4942378.

[19] N. Ellens and K. Hynynen, “Simulation study of the effects of near- and far-field heating during focused ultrasound uterine fibroid ablation using an electronically focused phased array: A theoretical analysis of patient safety,” *Med. Phys.*, vol. 41, no. 7, 2014, doi: 10.1118/1.4883777.

[20] N. Ellens, B. Lucht, S. Gunaseelan, J. Hudson, and K. Hynynen, “A novel, flat, electronically-steered phased array transducer for tissue ablation: preliminary results,”

Phys. Med. Biol., vol. 60, p. 2105, 2015.

[21] M. Yiannakou, M. Trimikliniotis, C. Yiallouras, and C. Damianou, "Evaluation of focused ultrasound algorithms: Issues for reducing pre-focal heating and treatment time," *Ultrasonics*, vol. 65, pp. 145–153, 2016, doi: 10.1016/j.ultras.2015.10.007.

[22] T. Drakos, M. Giannakou, G. Menikou, G. Constantinides, C. Damianou,Characterization of a soft tissue-mimicking agar/wood powder material for MRgFUS applications, Ultrasonics(2021), doi: https://doi.org/10.1016/j.ultras.2021.

[23] S. A. Sapareto and W. C. Dewey, "Thermal dose determination in cancer therapy," *Int. J. Radiat. Oncol. Biol. Phys.*, vol. 10, no. 6, pp. 787–800, 1984, doi: 10.1016/0360-3016(84)90379-1.

[24] Menikou, G., Damianou, C. Acoustic and thermal characterization of agar based phantoms used for evaluating focused ultrasound exposures. *J Ther Ultrasound* **5,** 14 (2017). https://doi.org/10.1186/s40349-017-0093-z.

[25] Menikou G, Yiannakou M, Yiallouras C, Ioannides C, Damianou C. MRI-compatible breast/rib phantom for evaluating ultrasonic thermal exposures. *Int J Med Robot Comput Assist Surg*. 2018;14(1):1-12. doi:10.1002/rcs.1849.

[26] M. W. Dewhirst, L. B. Viglianti, M. Lora-Michiels, P. J. Hoopes, and M. Hanson, "Thermal Dose Requirement for Tissue Effect," *Proc SPIE Int Soc Opt Eng*, vol. 37, no. 3, pp. 338–348, 2003, doi: 10.1117/12.476637.THERMAL.

[27] Z. M. Lenard, N. J. McDannold, F. M. Fennessy, E. A. Stewart, F. A. Jolesz, K. Hynynen, C. M. Tempany, "Uterine Leiomyomas: MR Imaging-guided focused ultrasound surgery-imaging predictors of success", *Radiology*. 149(1) (2008) 187-94, doi: 10.1148/radiol.2491071600

[28] F. M. Knuttel, S. E. M. Huijsse, T. L. Feenstra, C. T. W. Moonen, M. A. A. J. van den Bosch, E. Buskens, M. J. W. Greuter, G. H. de Bock, "Early health technology assessment of magnetic resonance-guided high intensity focused ultrasound ablation for the treatment of early-stage breast cancer", *J Ther Ultrasound*. 5 (2017) 23, doi: 10.1186/s40349-017-0101-3

[29] H-L Liu, W-L Lin, Y-Y Chen, "A fast and conformal heating scheme for producing large thermal lesions using a 2D ultrasound phased array", *Int J Hyperthermia*. 23(1) (2007) 69-82, doi: 10.1080/02656730601087518

[30] A. Payne, U. Vyas, A. Blankespoor, D. Christensen, R. Roemer, "Minimisation of HIFU pulse heating and interpulse cooling times", *Int J Hyperthermia* 26(2) (2010) 198-208, doi: 10.3109/02656730903436459

[31] F. M. Fennessy, C. M. Tempany, "MRI-guided focused ultrasound surgery of uterine leiomyomas", Acad Radiol. 12(9) (2005) 1158-66, doi: 10.1016/j.acra.2005.05.018